CHAPTER 5

RESULTS AND DISCUSSION

In this chapter, the performance of direct ethanol fuel cell is discussed in three parts using laboratory synthesized Pt-based electrocatalysts i.e., (i) bi-metallic electrocatalysts supported on acetylene black carbon (C_{AB} or C_{PAB}): **Part-I**, (ii) bi-metallic and tri-metallic electrocatalysts supported on multi-wall carbon nanotubes (f-MWCNT): **Part-II** and (iii) optimization of DEFC process parameters using the best tri-metallic electrocatalyst supported on f-MWCNT: **Part-III**. The first part of **Part-I** is subdivided into **Part-1a and Part-1b**. The first part of **Part-Ia** deals with the performance evaluation of synthesized electrocatalysts without post treatment. While, **Part-Ib** deals with the performance evaluation of the synthesized post treated electrocatalysts. The physical characterization of support material and electrocatalysts, and electrochemical characterizations of synthesized electrocatalysts are discussed at the beginning of **Part-I (Part-1a and Part-Ib) and Part-II**. The effect of various parameters e.g., different types of anode electrocatalysts, ethanol concentrations, and cell operating temperature are also discussed in detail at the end of **Part-I and Part-II. Part-III** deals with the optimization and validation of process parameters using response surface methodology (RSM) for effective power generation from a proton exchange membrane based direct ethanol fuel cell (DEFC).

5.1 Performance evaluation of bi-metallic electrocatalysts supported on C_{AB}: Part-I

As already mentioned, that the post treatment of synthesized electrocatalyst improves the electrocatalytic activity for the ethanol electrooxidation. Thus, in the first phase of electrocatalyst synthesis, no post treatment was implemented and all such synthesized electrocatalysts were grouped and discussed in the section 5.1.1 **(Part-Ia)** below. While, in the second phase of electrocatalyst synthesis, the electrocatalysts were post treated and all such synthesized electrocatalysts were grouped, and discussed in the section 5.1.2 **(Part-1b)** (Page no. 150). The studies on post treatment of electrocatalysts and without post treatment of electrocatalysts were performed to see the degree of enhancement of electrocatalyst performance and comparison purpose.

5.1.1 Bi-metallic electrocatalysts without post treatment: Part-Ia

5.1.1.1 Physical characterization of the acetylene black carbon support

The functionalized/treated dry mass of acetylene black (C_{AB}) was obtained at the end of the process as described in section 3.3.1 (Page no. 81). The important properties of pristine acetylene black carbon (C_{PAB}) and functionalized acetylene black carbon (C_{AB}) support material are discussed below in detail.

5.1.1.1.1 pH analysis

As discussed earlier that the nature of carbon support material plays a key role in the synthesis of supported electrocatalyst for the fuel cell. de la Fuente et al., (2009) reported that the treatment of the carbonaceous materials with concentrated HNO_3 is an effective acid reagent for creating surface functional groups for nanoparticle anchoring sites, hydrophilicity, and dissolving the remaining impurities. The pH of the aqueous slurry of nitric acid functionalized carbon black (C_{AB}) support decreases considerably (pH = 3.2)

compared to that of pristine acetylene black carbon (C_{PAB}) support (pH = 8.12). The drastic decrease in pH of functionalized carbon black (C_{AB}) support indicates that sufficient acidic functional groups (carboxylic groups) have been introduced after acidic treatment.

5.1.1.1.2 X-ray diffraction (XRD) analysis

The X-ray diffraction (XRD) patterns of pristine acetylene black (C_{PAB}) and functionalized acetylene black carbon (C_{AB}) support are presented in Fig (5.1a-b). The XRD patterns of C_{PAB} and C_{AB} support show two common peaks of both the samples. It was also observed from Fig (5.1a-b) that there are two peaks at the 2θ value of 25.54º (002) and 42.65º (100), which indicate the characteristic diffraction pattern of the graphitic structure of the acetylene black support material (JCPDS card no. 34-1832). The first intense peak around 2θ of 25.56º refers to the high degree of graphitization (002) facet of support material (Huang et al., 2015). The XRD results of acetylene black support material as presented in Table (5.1) which shows that the interplanar spacing of C_{AB} is 0.3513 nm due to random plane orientations compare to the graphite interplanar spacing of 0.335 nm. The existence of sp^2 carbon-bonded graphite crystals of carbon support C_{PAB} and C_{AB} confirm that acetylene black has a turbostratic structure (Tang et al., 2014). After the acid treatment with concentrated nitric acid, the (002) peak of acetylene black carbon support became sharper and intense. The functionalized acetylene black (C_{AB}) shows a smaller d_{002} spacing value of 0.3473 nm and a larger crystallite size of 3.37 nm in comparison to pristine acetylene black carbon (C_{PAB}).

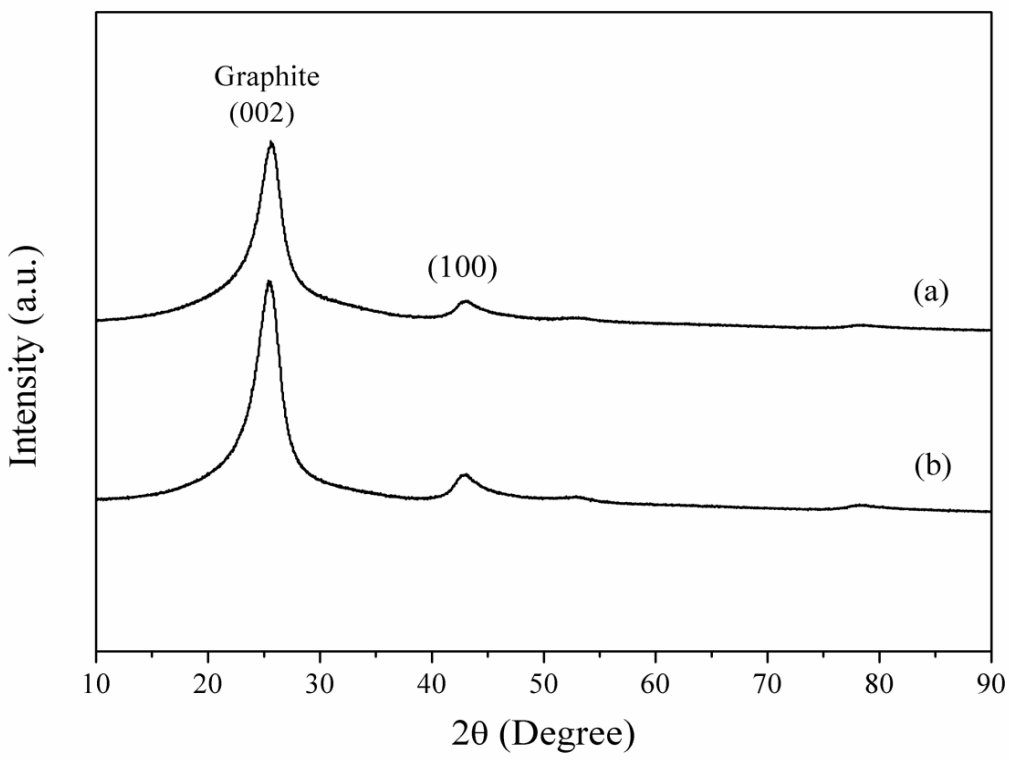

Figure 5.1 XRD patterns of (a) pristine acetylene black carbon (C_{PAB}) and (b) functionalized acetylene black carbon (C_{AB}) support.

Table 5.1 Physical properties of acetylene black support material derived from XRD patterns.

Carbon support	**C (002) peak position 2θ (º)**	**d_{002} spacing (nm)**	**FWHM peak**	**Crystallite size from XRD (nm)**
Pristine acetylene black carbon (C_{PAB})	25.34	0.3513	3.09	2.82
Functionalized acetylene black carbon (C_{AB})	25.62	0.3473	2.53	3.37

5.1.1.1.3 Fourier transform infrared spectroscopy (FTIR) analysis

The Fourier transform infrared spectroscopy (FTIR) is a very useful analysis technique that detects various characteristic functional groups present in the carbon support samples i.e., C_{PAB} and C_{AB}, respectively. Fig (5.2) shows the FTIR spectra of C_{PAB} and C_{AB} using FTIR in the wavelength range of 500–4000 cm^{-1}.

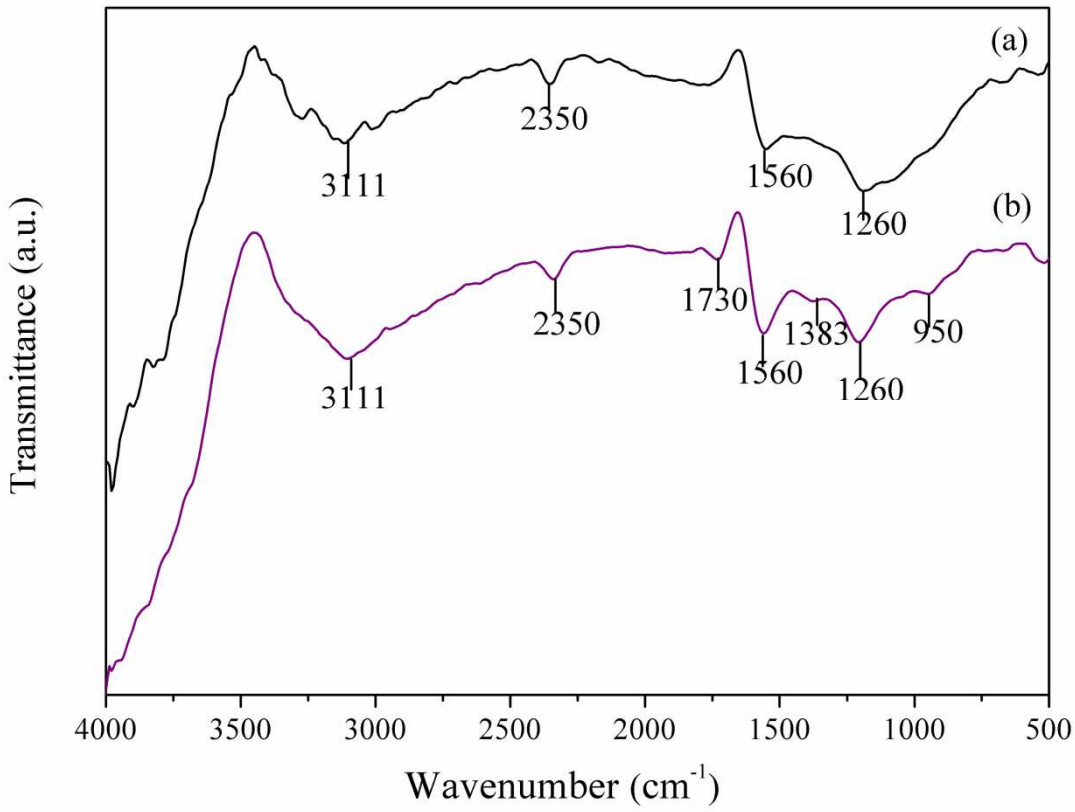

Figure 5.2 FTIR spectra of (a) pristine acetylene black carbon (C_{PAB}) and (b) functionalized acetylene black carbon (C_{AB}) support.

Both the samples of carbon support show four common peaks located at about 3111 cm^{-1}, 2350 cm^{-1}, 1560 cm^{-1} and 1206 cm^{-1} are attributed to the O–H, CO_2, C=C and CO–H functional groups, respectively (Zu et al., 2013, Miao et al., 2013 and Jin et al., 2018). Additional three peaks in functionalized acetylene black carbon (C_{AB}) surface at 1730 cm^{-1}, 1383 cm^{-1} and 950 cm^{-1}, which are ascribed to the oscillation of carboxylic groups (C=OOH), O–H bending deformation in carboxylic acid groups, and C–H out of plane deformation, respectively (Tang et al., 2014). It is evident from Fig (5.2b) and Table (5.2) that the sufficient acidic functional groups have been introduced after the acid treatment on the surface of acetylene black carbon support. These created oxygen-containing groups on the surface of functionalized carbon support (C_{AB}) resulting in hydrophilicity and anchoring sites to form complexes with different metal ions of platinum and ruthenium.

Table 5.2 Comparison and shifting of bands data of pristine (C_{PAB}) and functionalized acetylene black carbon (C_{AB}) support in FTIR analysis.

Stretching or bending functional groups	**Wavenumber (cm^{-1})**	
	Pristine acetylene black carbon (C_{PAB})	**Functionalized acetylene black carbon (C_{AB})**
C-H, out of plane deformation	…	950
C–OH stretching vibrations	1206	1206
O–H bending deformation in carboxylic acid	…	1383
C=C stretching vibrations of C_{AB} backbones	1560	1560
C=O stretching in carboxylic groups	…	1730
CO_2 signal	2350	2350
O-H group	3111	3111

5.1.1.1.4 Field-emission scanning electron microscopy (FESEM) analysis

Fig (5.3a) and Fig (5.3b) show FESEM images of pristine acetylene black (C_{PAB}) and functionalized acetylene black carbon (C_{AB}). It is seen in the FESEM images that the carbon support is of spherical morphology consisting of carbon nanospheres with a size in the range of 40 to 60 nm. Pristine acetylene black carbon (C_{PAB}) is consisted of agglomerated spherically shaped carbon nanospheres with cross-linked structure and formed aggregates in the form of clusters or a steric specific chain structure. The morphological change in the functionalized acetylene black carbon (C_{AB}) is not significant in comparison to pristine acetylene black carbon (C_{PAB}), except for a minute change in particle size (Fig 5.3b). These results suggest that the treatment of carbon support with HNO_3 does not affect their physical morphology severely. However, it modifies their surface chemical properties such as hydrophilicity and surface functional groups which are discussed in the following section.

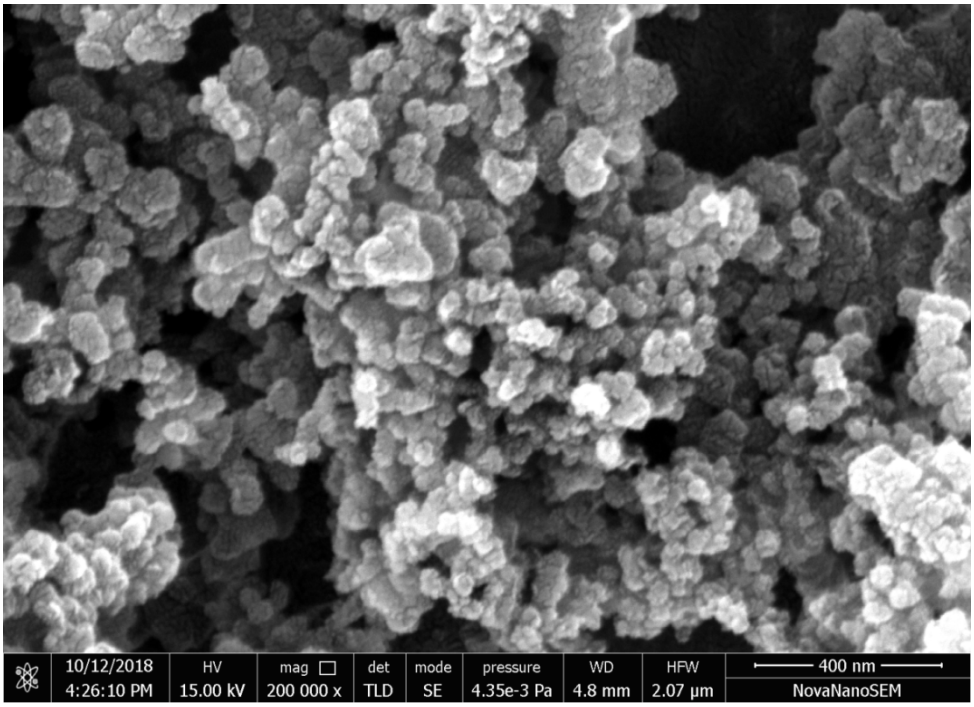

Figure 5.3a FESEM image of pristine acetylene black carbon (C_{PAB}).

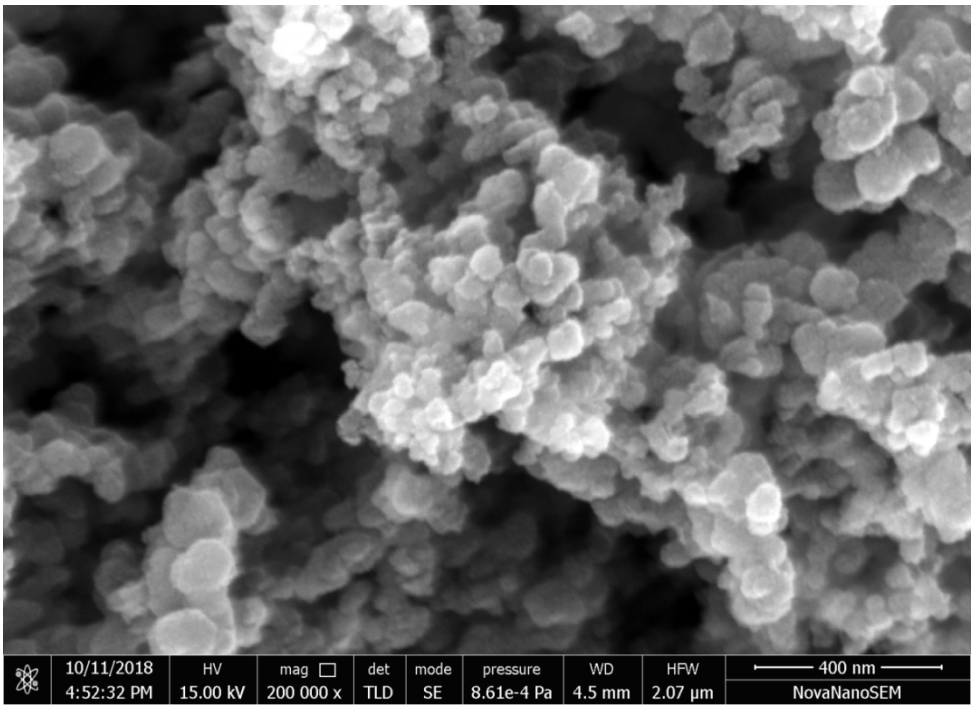

Figure 5.3b FESEM image of functionalized acetylene black carbon (C_{AB}).

5.1.1.2 Physical Characterization of electrocatalysts

5.1.1.2.1 X-ray diffraction (XRD) analysis

The XRD analysis provides the bulk structural information of the electrocatalyst and its support material. Fig (5.4a-f) presents the XRD patterns, mainly crystallographic structures of the synthesized and commercial electrocatalysts, respectively. The first broad diffraction peaks at about 2θ of 25.5° were observed for Pt-Ru/C_{PAB}-PLM, Pt-Ru/C_{PAB}-FAM, Pt-Ru/C_{AB}-PLM, Pt-Ru/C_{AB}-FAM, and Pt/C_{AB}-PLM electrocatalysts due to the assigned (002) graphite crystalline plane of acetylene black carbon (C_{AB}) support material with hexagonal structure. However, the diffraction peak of carbon support material is not found in the case of commercial Pt-Ru/C electrocatalyst because the peak intensity of support material which is generally Vulcan XC-72R gives less intense due to its lower crystallinity grade, compared to the intensity of Pt-Ru metal peak (Goel and Basu, 2014). The XRD patterns of all the electrocatalysts (Fig 5.4a-e) display Pt-Ru alloy diffraction peaks at around 40º, 47º and 68º are attributed to Pt (111), Pt (200) and Pt (220), respectively. This indicates the typical character of the face-centered cubic (fcc) crystalline structure of platinum (Pt). The shift of the Pt peaks to the higher angles is found in the synthesized electrocatalyst due to the presence of Pt-Ru alloy. The XRD pattern of commercial Pt-Ru/C (Fig 5.4e) electrocatalyst shows broader peaks as compared to synthesized Pt-Ru/C_{AB}-PLM and Pt-Ru/C_{AB}-FAM. A similar trend is also observed for commercial Pt-Ru/C in comparison to Pt-Ru/C_{PAB}-PLM and Pt-Ru/C_{PAB}-FAM. Broader peaks of commercial Pt-Ru/C electrocatalyst may be due to its lower crystallinity and smaller particles having lattice strain. However, no diffraction peak for Ru hexagonal structure is detected in the XRD pattern of electrocatalysts, indicating its presence in the amorphous state either in the form of metallic ruthenium or ruthenium oxides (Yang et al., 2003 and Datta et al., 2009).

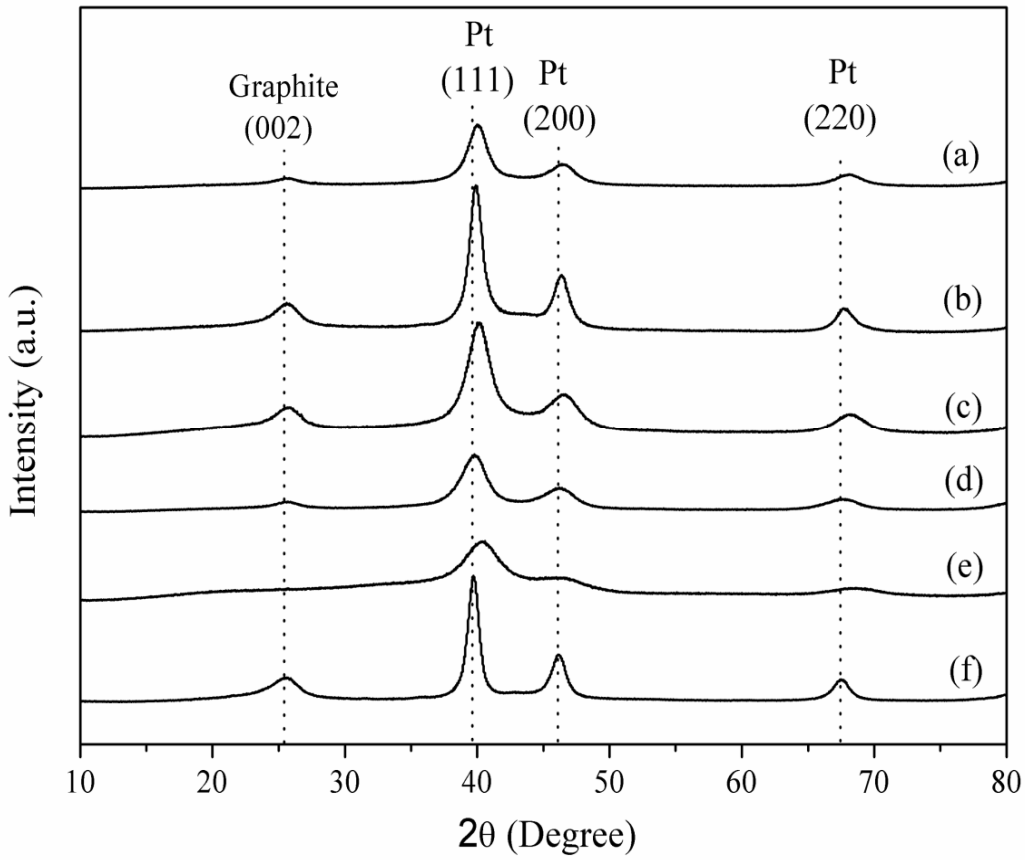

Figure 5.4 XRD patterns of (a) Pt-Ru/C_{PAB}-PLM, (b) Pt-Ru/C_{PAB}-FAM, (c) Pt-Ru/C_{AB}-PLM, (d) Pt-Ru/C_{AB}-FAM, (e) commercial Pt-Ru/C and (f) Pt/C_{AB}-PLM electrocatalysts.

The lattice parameters (Table 5.3) of all the electrocatalysts are smaller than that of Pt/C (JCPDS # 040802, a_{fcc} = 0.3915 nm) due to the formation of a Pt-Ru solid solution (Li et al., 2007). The reduction in the lattice parameter of Pt crystal structure reveals the incorporation of secondary smaller atomic-sized Ru metal (R_{Pt} = 1.39 Å and R_{Ru} = 1.34 Å) into the Pt crystal to form Pt-Ru solid alloy solution. This could result in the contraction of Pt lattice parameter in Pt-Ru bimetallic supported electrocatalysts.

The average crystallite sizes (d_c) of Pt-Ru bimetallic supported electrocatalysts were calculated based on the broadening of the Pt (220) peak using the Debye-Scherrer's equation Equation (3.4) as discussed in section 3.3.3.3. The diffraction peaks of Pt (220)

from the XRD patterns were considered to calculate the average crystallite size and lattice parameter of Pt (Wang et al., 2011 and Tayal et al., 2012). The composition of the supported Pt-Ru alloy electrocatalysts was calculated by the shift of Pt-Ru diffraction peaks i.e., the variation of the lattice parameter $a_{Pt-Ru/C}$ from the XRD patterns, which is based on Vegard's law (Chu and Gilman, 1996). The lattice parameter ($a_{Pt-Ru/C}$) of Pt-Ru alloy electrocatalyst was used to calculate Ru atomic fraction $(x_{Ru})(< 0.7)$ using the relationship of Vegard's law (Pires et al., 2013).

$$a_{\mathrm{Pt-Ru/C}} = a_{\mathrm{Pt/C}} - Kx_{\mathrm{Ru}} \tag{5.1}$$

where $a_{Pt/C}$ and $a_{Pt-Ru/C}$ are the lattice parameter of Pt/C and the Pt–Ru/C alloyed electrocatalyst, respectively. The value of $a_{Pt/C}$ is 0.3915 nm and the value of constant K is 0.0124 nm were taken from published literature (Antolini et al., 2001 and Li et al., 2007).

Further, the amounts of alloyed ruthenium (Ru_{alloy}) in the Pt-Ru/C alloy electrocatalysts were calculated using the equation below (Antolini et al., 2001):

$$Ru_{\mathrm{alloy}} = \frac{x_{\mathrm{Ru}}}{\left[(1-x_{\mathrm{Ru}})\left(\frac{\mathrm{Ru}}{\mathrm{Pt}}\right)_{\mathrm{nom.}}\right]} \tag{5.2}$$

Where $\left(\frac{\mathrm{Ru}}{\mathrm{Pt}}\right)_{\mathrm{nom.}}$ represents the nominal atomic ratio of Ru to Pt and x_{Ru} is the atomic content of alloyed Ru fraction in the Pt-Ru/C alloy electrocatalysts. The relative data calculated from XRD diffraction patterns by the Debye-Scherrer's equation (Equation 3.4) and Vegard's law (Equations 5.1 and 5.2) are presented in Table (5.3).

Table 5.3 Data calculated from XRD patterns of electrocatalysts by the Debye Scherrer's equation and Vegard's law.

Electrocatalysts	**Average crystallite size (d_c) by XRD (nm)**	**Lattice parameter $a_{(Pt\text{-}Ru/C)}$ (nm)**	**Pt (2 2 0) position (Deg.)**	**Ru fraction (x_{Ru})**	**Alloyed Ru (wt. %)**
Pt-Ru/C_{PAB}-PLM	3.8	0.3885	68.20	0.242	31.93
Pt-Ru/C_{PAB}-FAM	5.8	0.3889	68.10	0.210	26.58
Pt-Ru/C_{AB}-PLM	3.6	0.3883	68.24	0.270	37.0
Pt-Ru/C_{AB}-FAM	3.4	0.3884	68.22	0.254	34.04
Commercial Pt-Ru/C	2.8	0.3877	68.35	0.310	44.73
Pt/C_{AB}-PLM	6.0	0.3915	67.60	---	---

It is seen from Table 5.3 that the average crystallite size of all the synthesized bi-metallic electrocatalysts lies in the range of 3.4 nm to 5.8 nm. The average crystallite size obtained for the synthesized electrocatalysts supported on pristine acetylene black C_{PAB} i.e., Pt-Ru/C_{PAB}-PLM and Pt-Ru/C_{PAB}-FAM is higher than that of the functionalized acetylene black C_{AB} supported electrocatalysts Pt-Ru/C_{AB}-PLM and Pt-Ru/C_{AB}-FAM, respectively. The calculated average crystallite sizes (d_c) of the synthesized Pt-Ru/C_{PAB}-PLM and Pt-Ru/C_{PAB}-FAM electrocatalysts were 3.8 nm and 5.8 nm, respectively. It may be due to a lack of oxygenated species on the surface of pristine acetylene black C_{PAB}. The alloying degree of Ru for the synthesized Pt-Ru/C_{PAB}-PLM and Pt-Ru/C_{PAB}-FAM electrocatalysts is 31.93 wt. % and 26.58 wt. %, which are lower than the Pt-Ru/C_{AB}-PLM (37 wt.%) and Pt-Ru/C_{AB}-FAM (34 wt. %), respectively. Whereas, lower average crystallite size is obtained for the synthesized electrocatalyst Pt-Ru/C_{AB}-FAM with the Ru alloying of about 34.04 wt. %. Although, the particle size is a little larger for Pt-Ru/C_{AB}-PLM (3.6 nm) than electrocatalyst Pt-Ru/C_{AB}-FAM (3.4 nm) and commercial Pt-Ru/C electrocatalyst (2.8), the polyol method (Pt-Ru/C_{AB}-PLM) results in higher Ru alloying of

37.0 wt. % with Pt noble metal. The alloying of Ru with Pt atom plays a very crucial role in the electrooxidation of ethanol fuel. Thus, synthesized Pt-Ru/C_{AB}-PLM electrocatalyst is expected to perform excellently and produce comparable results with the commercial electrocatalyst Pt-Ru/C. It should be noted that the single metal electrocatalyst Pt/C_{AB}-PLM resulting in the largest crystallite size of 6 nm. The TEM of synthesized electrocatalysts was also performed to verify the analysis of the results of XRD of synthesized electrocatalysts which are discussed in the following section.

5.1.1.2.2 Field-emission scanning electron microscopy (FESEM) analysis

The surface morphology of the electrocatalysts was thoroughly examined via FESEM and their images are presented in Fig (5.5a) to Fig (5.5e). It is seen from Fig (5.5a) to Fig (5.5e) that the electrocatalysts particles are of nano-range with uniform size. The uniformity is more prominent in the FESEM images for the synthesized electrocatalysts Pt-Ru/C_{AB}-PLM (Fig 5.5c) and commercial electrocatalyst Pt-Ru/C (Fig 5.5e). The FESEM analysis also confirms that the particle sizes are in good agreement with the average crystallite size calculated from XRD analysis and average particle size from TEM analysis. The FESEM images also confirm that the synthesized electrocatalysts are porous which could facilitate mass transport from the bulk phase to the active electrocatalysts sites.

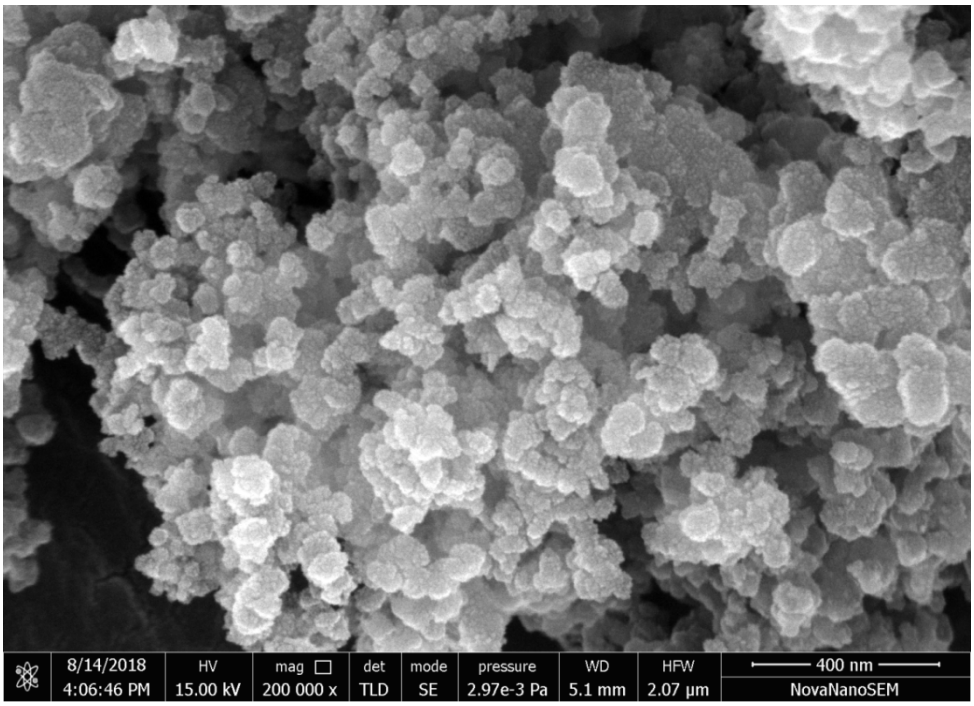

Figure 5.5a FESEM image of Pt-Ru/C_{PAB}-PLM electrocatalyst.

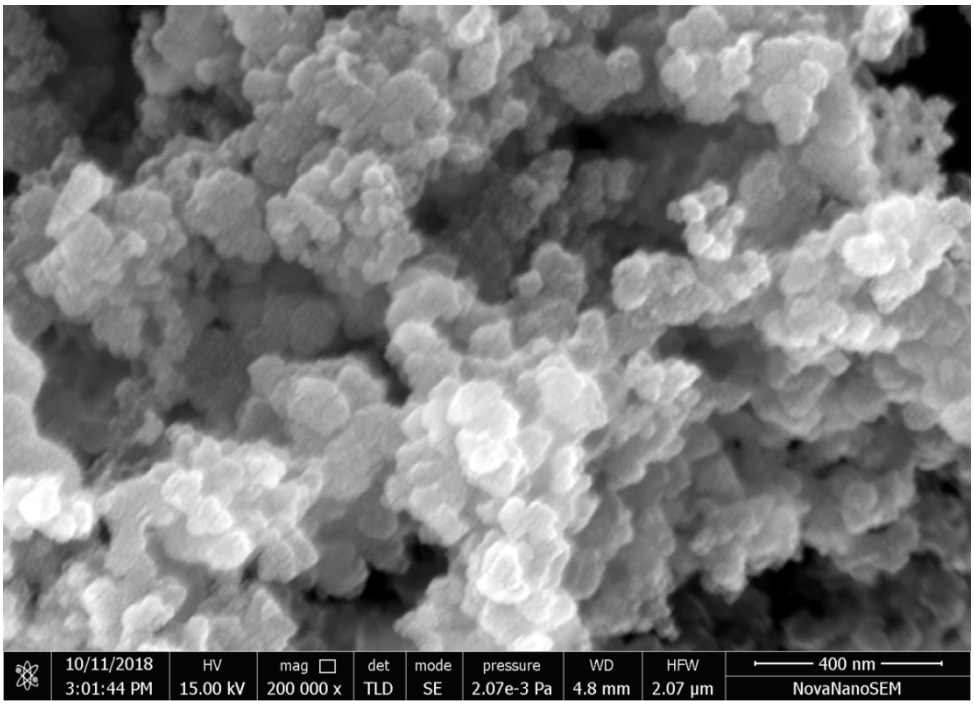

Figure 5.5b FESEM image of Pt-Ru/C_{PAB}-FAM electrocatalyst.

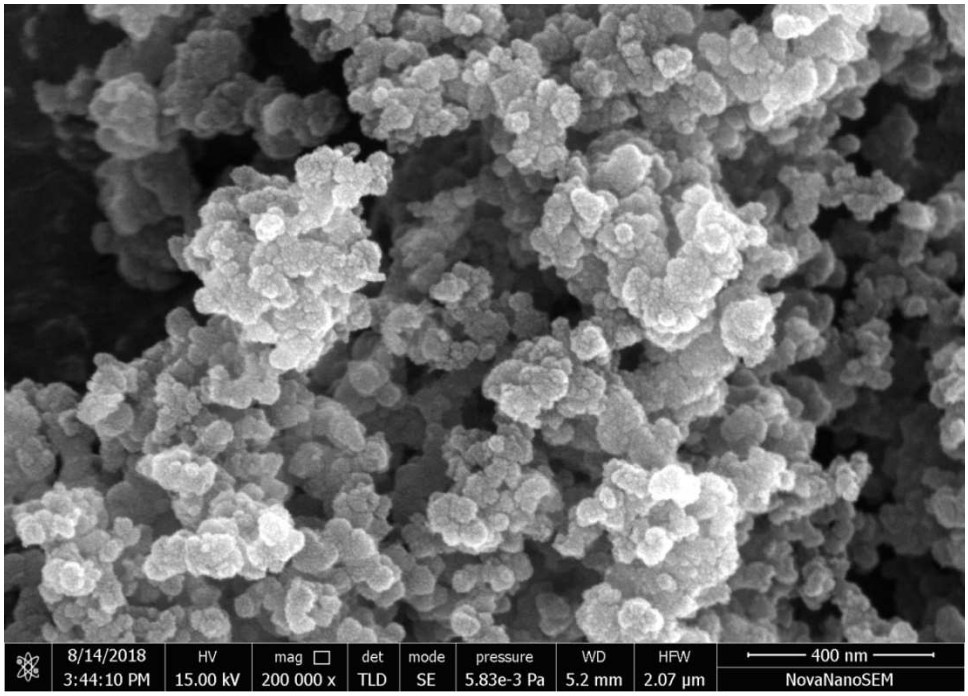

Figure 5.5c FESEM image of Pt-Ru/C_{AB}-PLM electrocatalyst.

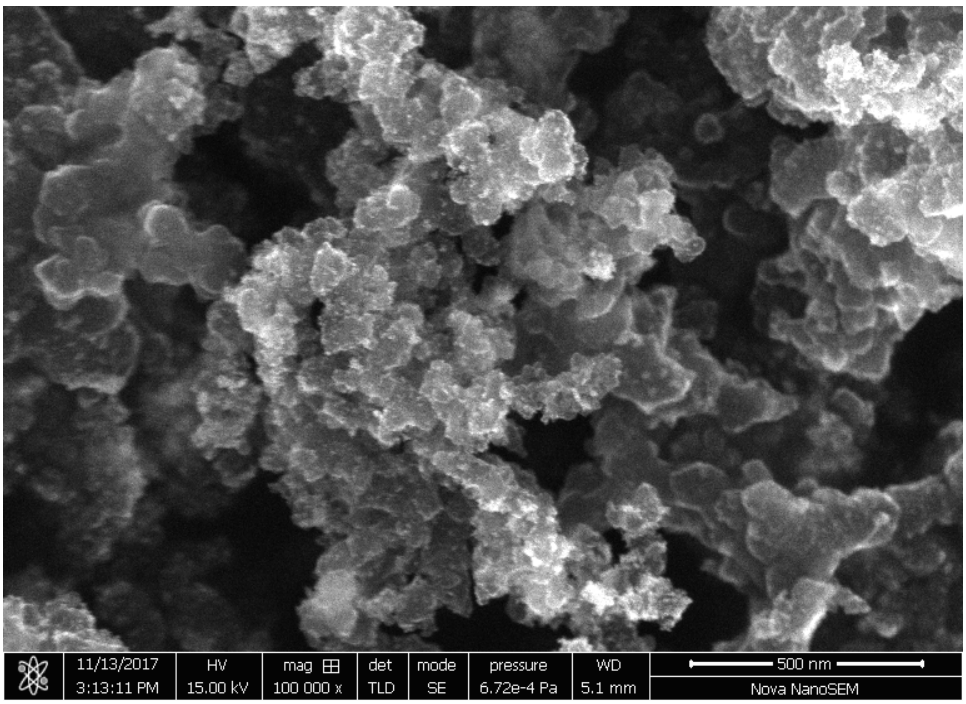

Figure 5.5d FESEM image of Pt-Ru/C_{AB}-FAM electrocatalyst.

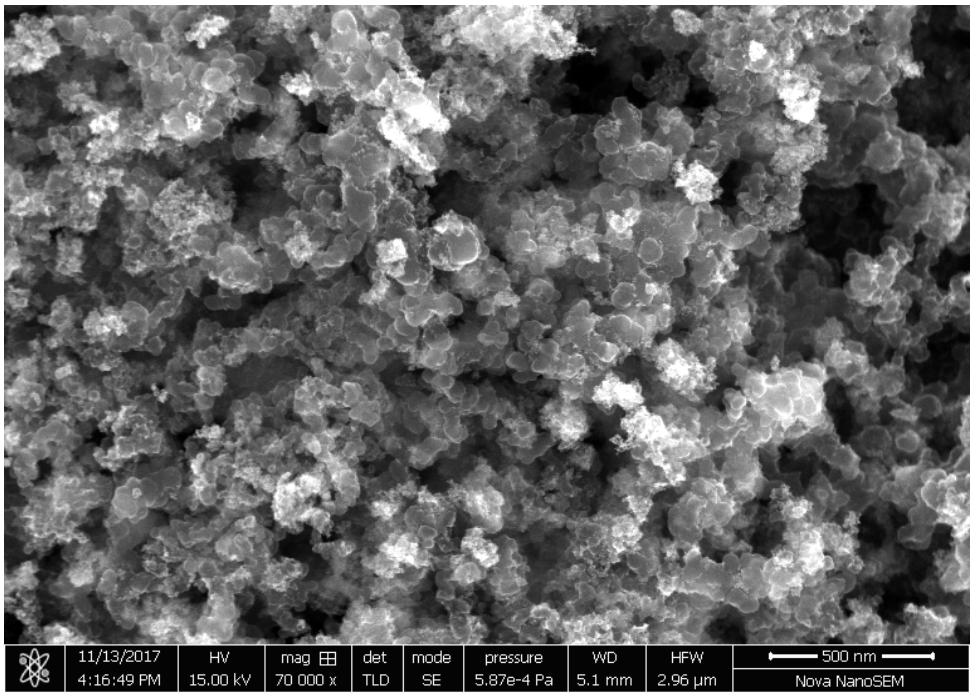

Figure 5.5e FESEM image of commercial Pt-Ru/C electrocatalyst.

5.1.1.2.3 Transmission electron microscopy (TEM) analysis

Fig (5.6a) to Fig (5.6e) show the typical TEM images of electrocatalyst and their metal particle size distribution. The average particle sizes and histograms of the size distribution of metal nanoparticles were estimated by counting the diameter of 150 metal nanoparticles in an arbitrarily chosen area of the corresponding TEM images. The thorough analysis of TEM images depicts that the electrocatalysts consist of almost spherical shape nano-sized particles, well-dispersed with negligible agglomerations on the carbon support material. It is also observed in the TEM images that the metal particle sizes of each sample are less than 11 nm and slightly agglomerated irrespective of the electrocatalysts types. Metal particles in the Pt-Ru/C_{PAB}-PLM and Pt-Ru/C_{PAB}-FAM electrocatalysts are in the nano range and a fraction of the metal particles clumped together to form slightly large aggregations (Fig 5.6a and Fig 5.6b).

The heavy black dots of Pt-Ru metal alloy electrocatalyst nanoparticles indicate well dispersion over carbon supports lighter particles of 40-60 nm size. The particle size for Pt-Ru/C_{AB}-PLM synthesized catalyst ranges from 1.5 to 6.5 nm, with an average particle size of 3.8 ± 0.9 nm. The average particle size for Pt-Ru/C_{AB}-FAM synthesized electrocatalyst is 3.51 ± 0.89 nm and the size distribution lies in the range of 1.5-8 nm. Similarly, for commercial Pt-Ru/C electrocatalyst, the average particle size is 3.0 ± 0.58 nm and size distribution ranges from 1.5 to 5.5 nm. However, the average particle size for commercial Pt-Ru/C electrocatalyst is lower than synthesized electrocatalysts but particles are seemed to be slightly agglomerated (Fig 5.6e).

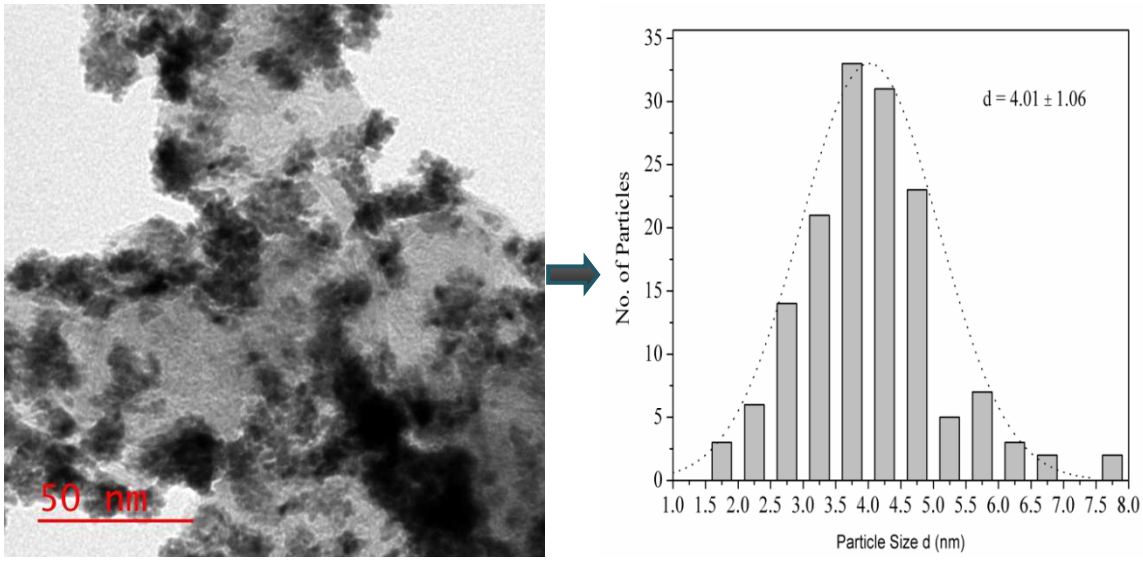

Figure 5.6a TEM image and histogram of metal particle size distribution of Pt-Ru/C_{PAB}-PLM electrocatalyst.

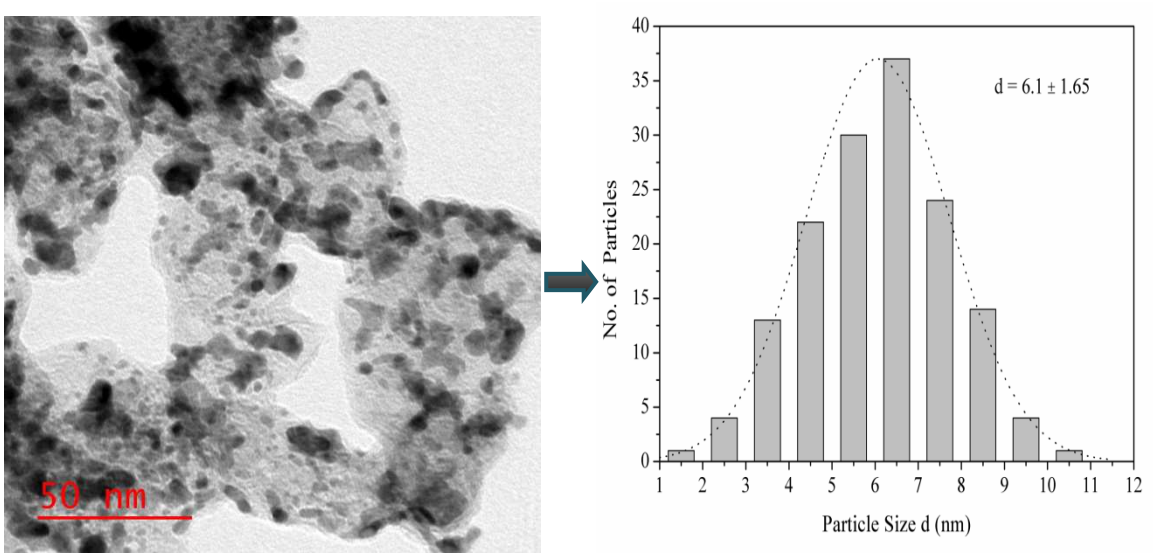

Figure 5.6b TEM image and histogram of metal particle size distribution of Pt-Ru/C_{PAB}-FAM electrocatalyst.

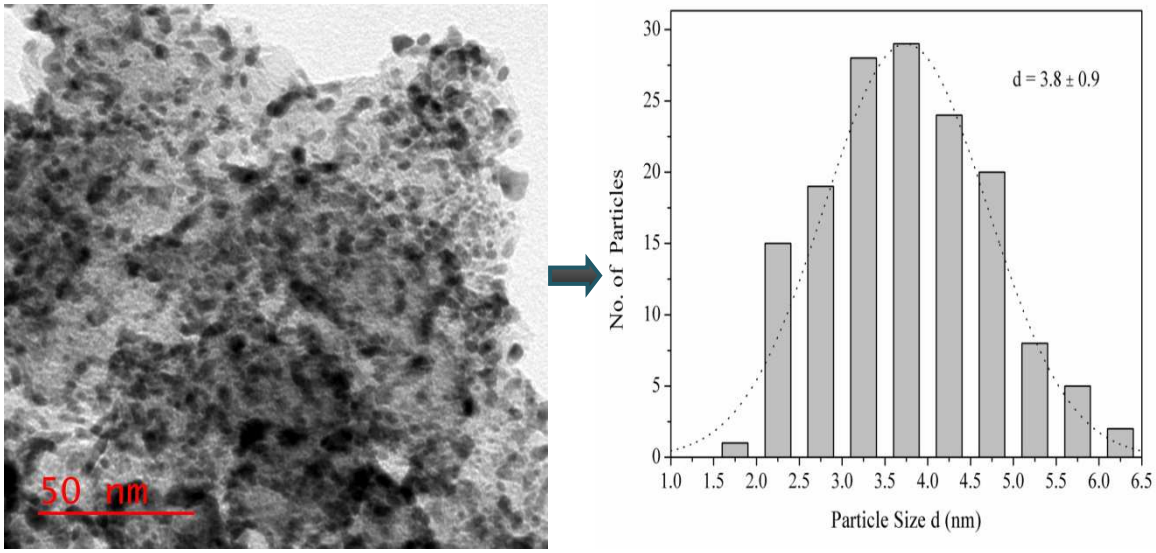

Figure 5.6c TEM image and histogram of metal particle size distribution of Pt-Ru/C_{AB}-PLM electrocatalyst.

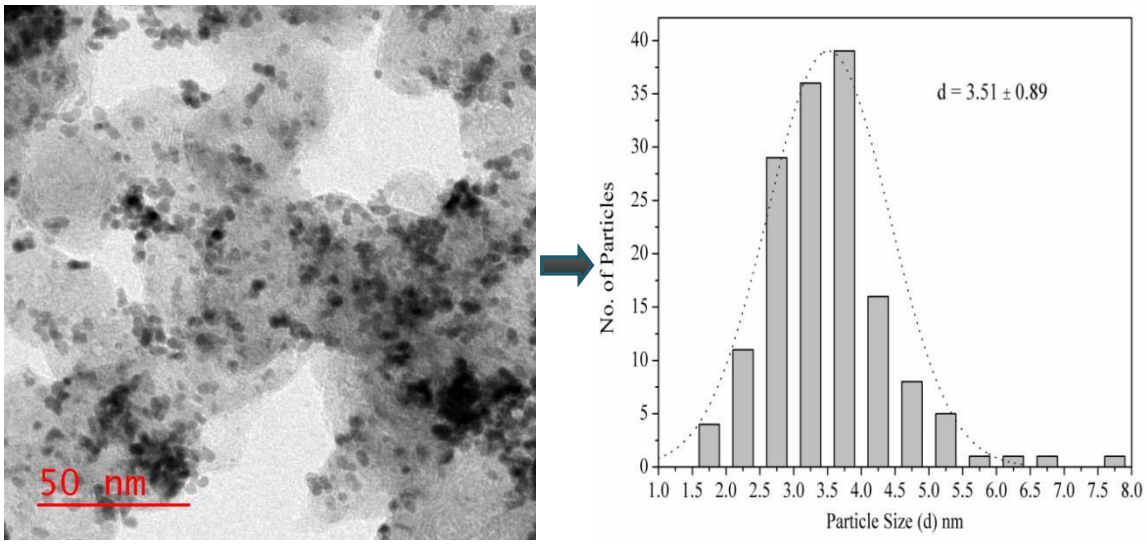

Figure 5.6d TEM image and histogram of metal particle size distribution of Pt-Ru/C_{AB}-FAM electrocatalyst.

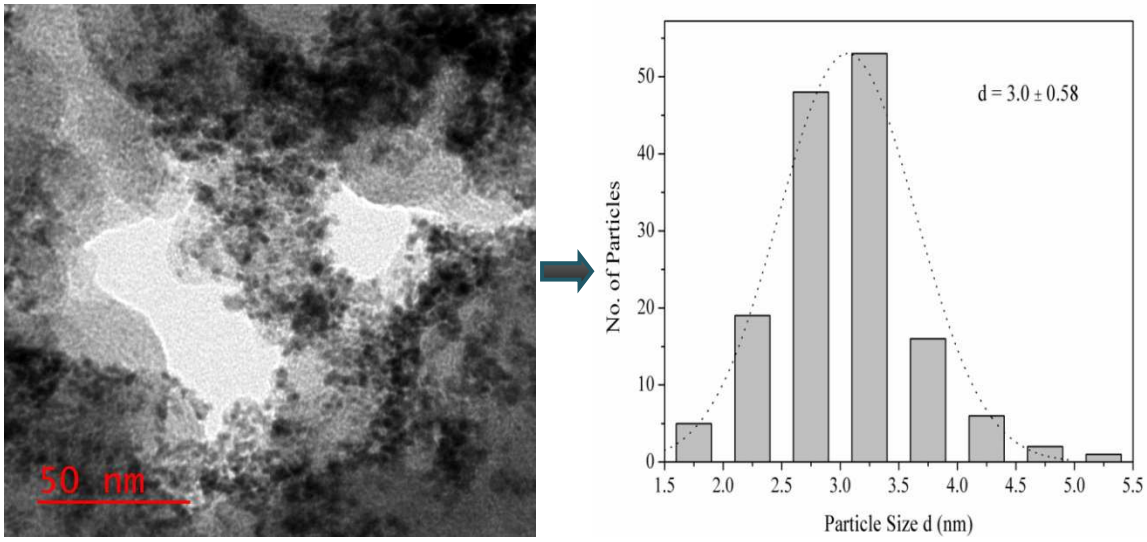

Figure 5.6e TEM image and histogram of metal particle size distribution of commercial Pt-Ru/C electrocatalyst.

The average particle size estimated by TEM images and the average crystallite size by XRD analysis is almost similar to an error of ± 10 % (Table 5.4). The metal surface area (SA) of the electrocatalyst was calculated from Equation (5.3) (Antolini and Cardellini 2001, Antolini et al., 2001 and Zhiani et al., 2013):

$$SA = \frac{60000}{\rho_{\mathrm{Pt-Ru}} d_{\mathrm{p}}} \tag{5.3}$$

$$\rho_{Pt-Ru} = X_{Pt} \times \rho_{Pt} + X_{Ru} \times \rho_{Ru} \tag{5.4}$$

where *SA* is the surface area (m^2/g), d_{p} is the average particle size (nm), $\rho_{\mathrm{Pt-Ru}}$ is the density of Pt-Ru alloy nanoparticles, ρ_{Pt} is the density of Pt metal (21.4 g cm^{-3}), ρ_{Ru} is the density of Ru metal (12.3 g cm^{-3}), and X_{Pt} and X_{Ru} are the wt. % of Pt and Ru in the electrocatalyst, respectively.

The metal surface areas (*SA*) obtained for synthesized Pt-Ru/C_{PAB}-PLM, Pt-Ru/C_{PAB}-FAM, Pt-Ru/C_{AB}-PLM and Pt-Ru/C_{AB}-FAM electrocatalysts are 20.46 m^2/g, 13.46 m^2/g, 22.26 m^2/g and 24.31 m^2/g respectively. The metal surface area of all synthesized electrocatalysts is slightly lower than the commercial Pt-Ru/C (25.62 m^2/g) electrocatalyst (Table 5.4).

Table 5.4 The average particle size and specific area of electrocatalysts from TEM analysis and comparison with XRD results.

Electrocatalysts	**Average particle size (d_p) by TEM (nm)**	**Average crystallite size (d_c) by XRD (nm)**	**Surface area (m^2/g)**
Pt-Ru/C_{PAB}-PLM	4.01 ± 1.06	3.8	20.46
Pt-Ru/C_{PAB}-FAM	6.1 ± 1.65	5.8	13.46
Pt-Ru/C_{AB}-PLM	3.8 ± 0.9	3.6	22.26
Pt-Ru/C_{AB}-FAM	3.51 ± 0.89	3.4	24.31
Commercial Pt-Ru/C	3.0 ± 0.58	2.8	25.62

However, the surface area of synthesized Pt-Ru electrocatalyst supported on C_{AB} is higher than that of the synthesized Pt-Ru supported on C_{PAB}. This proves that functionalized support material C_{AB} resulted in smaller particle sizes of the C_{AB} supported bi-metallic Pt-Ru electrocatalysts and thus, the high surface area of synthesized electrocatalysts Pt-Ru/C_{AB}-PLM and Pt-Ru/C_{AB}-FAM were observed.

5.1.1.2.4 X-ray photoelectron spectroscopy (XPS) analysis

The chemical oxidation/valence states and surface compositions of Pt and Ru metals in the Pt-Ru/C_{PAB}-PLM, Pt-Ru/C_{PAB}-FAM, Pt-Ru/C_{AB}-PLM, Pt-Ru/C_{AB}-FAM and commercial Pt-Ru/C nano electrocatalysts were analyzed by XPS analysis. The XPS is a surface-sensitive method and most of the cluster atoms are surface atoms. Here it is assumed that the bulk information of the associated elements Pt, Ru, C and O in the supported electrocatalysts i.e., Pt-Ru/C_{AB} can only be obtained from the XPS analysis of the electrocatalysts. Fig (5.7a) to Fig (5.7e) selectively show the Pt (4f) core regional spectra of synthesized Pt-Ru/C_{PAB}-PLM, Pt-Ru/C_{PAB}-FAM, Pt-Ru/C_{AB}-PLM, Pt-Ru/C_{AB}-FAM, and commercial Pt-Ru/C electrocatalysts. As reported in the literature that the Pt $4f_{7/2}$ and $4f_{5/2}$ peaks are deconvoluted into three sets of the spin-orbit doublets (Lee et al., 2011 and Pires et al., 2013). The first set of Pt $4f_{7/2}$ and Pt $4f_{5/2}$ doublets at 71.42–71.7 eV and 74.9–75.1 eV is assigned to pure metallic Pt^0 (zero valance) state. The second doublets set at 72.64–72.8 eV and 75.8–76.1 eV can be ascribed to oxidized Pt^{2+} such as PtO or $Pt(OH)_2$ species, whereas the third doublets set at 73.9–74.7 eV and 77.2–77.9 eV is related with the Pt^{4+} oxide such as PtO_2 species (Lee et al., 2011 and Park et al., 2010). The different methods followed for the synthesis of electrocatalysts could result in different compositions of the oxidation states in the electrocatalyst metals present.

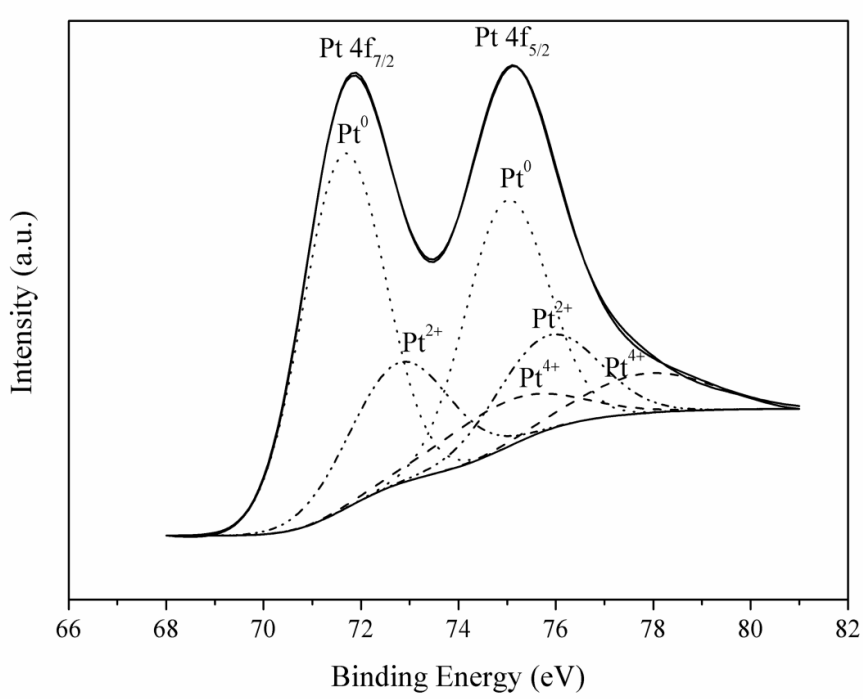

Figure 5.7a XPS spectra in Pt 4f region of Pt-Ru/C_{PAB}-PLM electrocatalyst. The solid line represents the XPS fitted spectra and the broken line represents the peaks due to different Pt oxidation state corresponds to Pt^0, Pt^{2+} and Pt^{4+}.

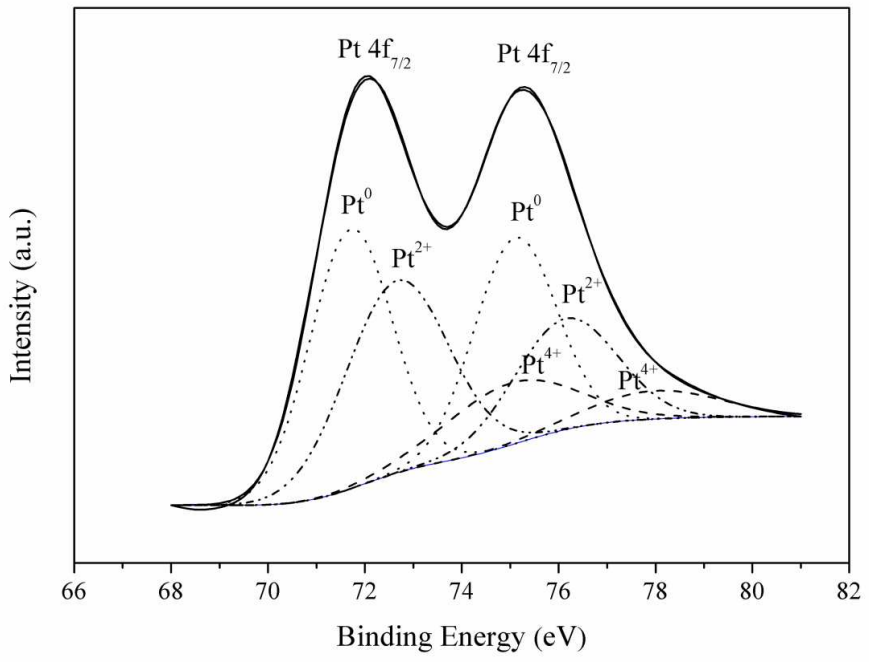

Figure 5.7b XPS spectra in Pt 4f region of Pt-Ru/C_{PAB}-FAM electrocatalyst. The solid line represents the XPS fitted spectra and the broken line represents the peaks due to different Pt oxidation state corresponds to Pt^0, Pt^{2+} and Pt^{4+}.

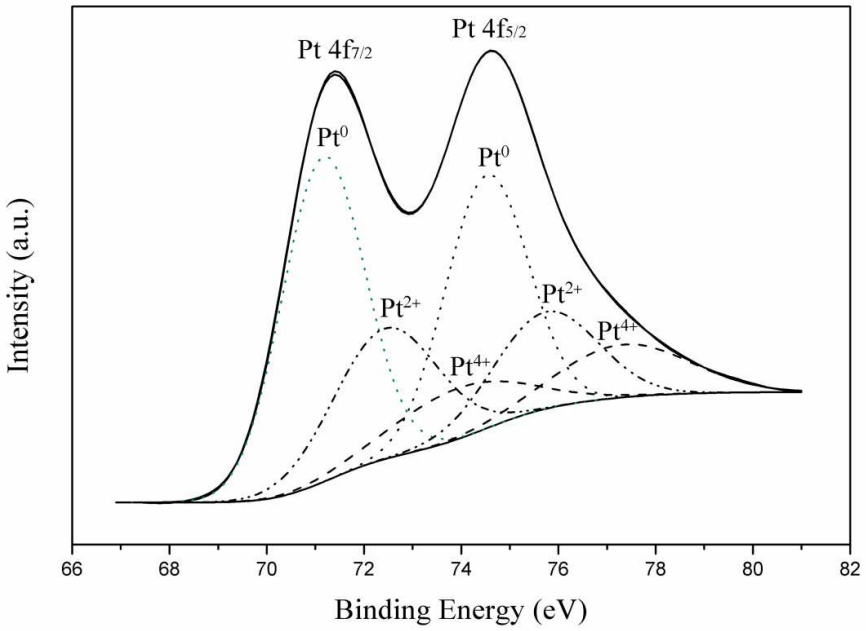

Figure 5.7c XPS spectra in Pt 4f region of Pt-Ru/C_{AB}-PLM electrocatalyst. The solid line represents the XPS fitted spectra and the broken line represents the peaks due to different Pt oxidation state corresponds to Pt^0, Pt^{2+} and Pt^{4+}.

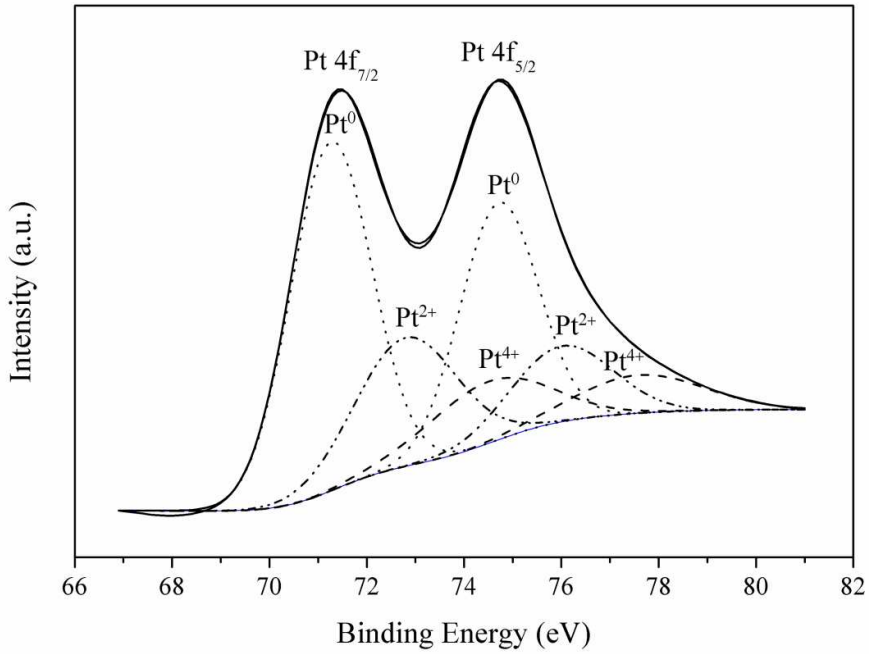

Figure 5.7d XPS spectra in Pt 4f region of Pt-Ru/C_{AB}-FAM electrocatalyst. The solid line represents the XPS fitted spectra and the broken line represents the peaks due to different Pt oxidation state corresponds to Pt^0, Pt^{2+} and Pt^{4+}.

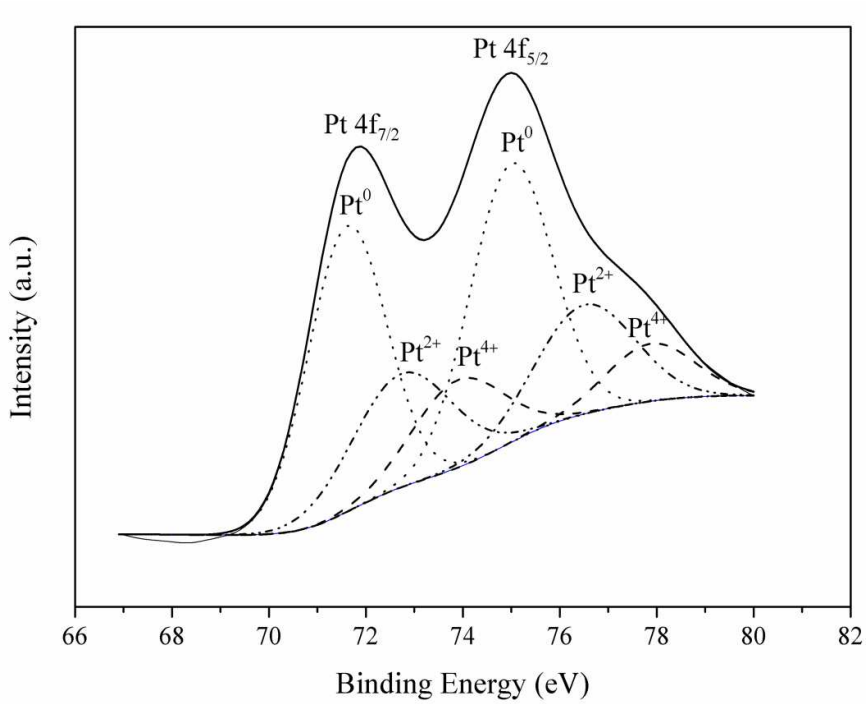

Figure 5.7e XPS spectra in Pt 4f region of commercial Pt-Ru/C electrocatalyst. The solid line represents the XPS fitted spectra and the broken line represents the peaks due to different Pt oxidation state corresponds to Pt^0, Pt^{2+} and Pt^{4+}.

The binding energies (BEs) of the Pt $4f_{7/2}$ component at their corresponding relative intensities are obtained from the respective mapped area of quantitative deconvoluted of peaks and the corresponding full-width at the half-maximum (FWHM) values are presented in Table (5.5). A slight shift of the Pt^0 (zero valance) peaks towards higher values of binding energies in comparison to that of bulk Pt (BE of Pt $4f_{7/2}$ = 70.5 eV) is due to the effect of small particles and the Pt-support interactions (Lee et al., 2011 and Pires et al., 2013). Generally, Pt^0 is found that only the predominant species in all the electrocatalysts (53.74–60.52 %). The electrocatalyst supported on pristine acetylene black (C_{PAB}) and synthesized by the FAM method showed the lowest amount of metallic Pt (Pt^0) while using the same method/FAM supported on functionalized acetylene black (C_{AB}) exhibited the highest content of Pt^0. However, there is an important contribution of oxidized Pt species such as Pt^{2+}/PtO or $Pt(OH)_2$ and Pt^{4+}/PtO_2. The pure metallic form is

Pt^0 which is slightly higher in the case of Pt-Ru/C_{AB}-FAM compare to Pt–Ru/C_{AB}-PLM and commercial Pt–Ru/C electrocatalysts (Table 5.5). The most preferential state of Pt species i.e., Pt^{2+}/PtO or $Pt(OH)_2$ was found to be maximum in the case of Pt-Ru/C_{AB}-PLM (28.66 %) (Pires et al., 2013). Irrespective of the synthesis methods used for electrocatalysts synthesis, the C_{AB} supported electrocatalysts resulting in a better oxidation state of Pt species.

Table 5.5 Different oxidation states of Pt species and their relative intensities obtained from binding energies (BE) of the Pt $4f_{7/2}$ component of XPS spectra for Pt-Ru/C_{PAB}-PLM, Pt-Ru/C_{PAB}-FAM, Pt-Ru/C_{AB}-PLM, Pt-Ru/C_{AB}-FAM and commercial Pt-Ru/C electrocatalysts.

Electrocatalysts	**Pt $4f_{7/2}$ component of XPS spectra**			
	Pt species	**BE of $4f_{7/2}$ (eV)**	**FWHM (eV)**	**Relative intensity (%)**
Pt-Ru/C_{PAB}-PLM	Pt^0/ metallic Pt	71.64	2.0	57.84
	Pt^{2+}/PtO or $Pt(OH)_2$	72.78	2.5	27.31
	Pt^{4+}/PtO_2	74.7	3.2	14.85
Pt-Ru/C_{PAB}-FAM	Pt^0/ metallic Pt	71.7	2.0	53.74
	Pt^{2+}/PtO or $Pt(OH)_2$	72.69	2.5	26.26
	Pt^{4+}/PtO_2	74.55	3.1	20.0
Pt-Ru/C_{AB}-PLM	Pt^0/ metallic Pt	71.42	2	57.0
	Pt^{2+}/PtO or $Pt(OH)_2$	72.64	2.5	28.66
	Pt^{4+}/PtO_2	73.95	3.2	14.34
Pt-Ru/C_{AB}-FAM	Pt^0/metallic Pt	71.47	2	60.52
	Pt^{2+}/PtO or $Pt(OH)_2$	72.8	2.5	22.12
	Pt^{4+}/PtO_2	74	3.2	17.36
Commercial Pt–Ru/C	Pt^0/metallic Pt	71.51	2	59.13
	Pt^{2+}/PtO or $Pt(OH)_2$	72.74	2.5	27.77
	Pt^{4+}/PtO_2	73.9	3.2	13.10

The XPS spectra of Ru (3d)–C(1s) region for electrocatalyst samples are presented in Fig (5.8a-e). The peak at 284.55 eV is attributed to graphitic carbon (C(1s)) support material in all the electrocatalysts substantiates the literature data (Rolison et al., 1999 and Aricò et al., 2003).

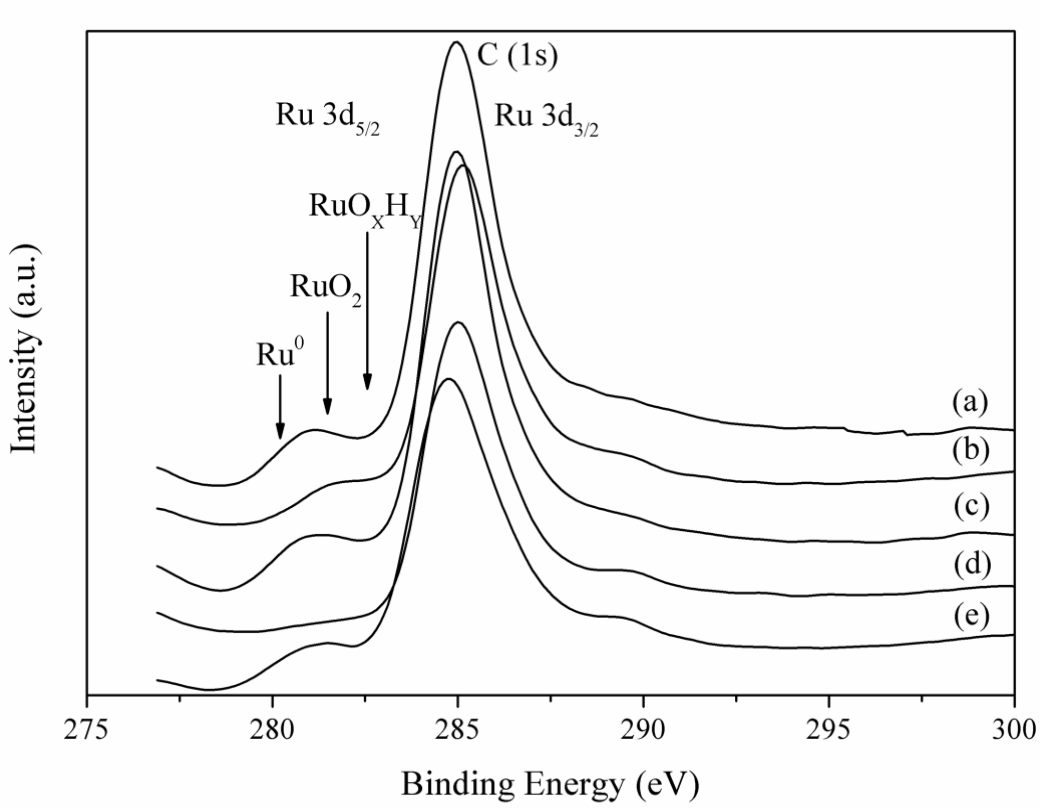

Figure 5.8 C(1s) + Ru(3d) region in (a) Pt-Ru/C_{PAB}-PLM, (b) Pt-Ru/C_{PAB}-FAM, (c) Pt-Ru/C_{AB}-PLM, (d) Pt-Ru/C_{AB}-FAM and (e) commercial Pt-Ru/C electrocatalysts.

Quantitative estimation of the oxidation states of Ru (3d) spectra is a slight bit difficult, as the C(1s) peak entirely covers the Ru($3d_{3/2}$) signal and partially overlaps with the Ru($3d_{5/2}$). However, two peaks at 280.3 eV and 281.5 eV can be easily observed for the synthesized electrocatalysts Pt-Ru/C_{AB}-PLM and commercial Pt-Ru/C for the Ru ($3d_{5/2}$) signal as shown in Fig (5.8). The peaks at 280.3 eV with a shoulder and 281.5 eV can be qualitatively attributed to Ru^0 and anhydrous RuO_2, respectively (Aricò et al., 2003 and

Raman et al., 2006). However, a flat plateau is observed for Pt-Ru/C_{AB}-FAM in the same region. The shifting of these peaks appears at about 0.3 eV to the higher binding energies concerning the corresponding standard values reported in the literature, which may be due to a large C(1s) peak tail (Aricò et al., 2003). The Ru($3d_{5/2}$) signal from hydrous amorphous RuO_xH_y is predictable at a binding energy ~1 eV higher than anhydrous RuO_2. Hence, the overlapping of the Ru($3d_{3/2}$) signal with the intense graphitic C(1s) peak, the presence of the hydrous ruthenium phase cannot be excluded. Thus, it may be concluded from the above discussion that the Pt-Ru/C_{AB}-PLM electrocatalyst is better than the Pt-Ru/C_{PAB}-PLM, Pt-Ru/C_{PAB}-FAM**,** Pt-Ru/C_{AB}-FAM and commercial electrocatalyst Pt-Ru/C about the oxidation state of Pt and Ru both.

5.1.1.2.5 Energy dispersive X-ray (EDX) analysis

The chemical composition of individual metal particles along with its support material carbon of all the electrocatalysts was analyzed by EDX (Fig 5.9a to Fig 5.9e). The EDX patterns, obviously confirm the presence of desired elements Pt, Ru and C in the electrocatalyst, respectively. The strongest C peak is assigned to the support material in all the electrocatalysts. The electrocatalyst prepared has the desired elements with some variation in composition as reported in Table (5.6). The EDX results show that the elemental composition of synthesized electrocatalysts varies from point to point as the electrocatalytic surface is heterogeneous. The EDX spectrum also shows the presence of oxygen and chlorine in electrocatalysts. The presence of chlorine may be probably coming from the remains of metal precursors during the reduction process. The existence of oxygen indicates the formation of ruthenium oxides/platinum oxides which are visible in XPS analysis (Table 5.6). The presence of these common impurities has been reported by Qian et al., (2008) and Tayal et al., (2011).

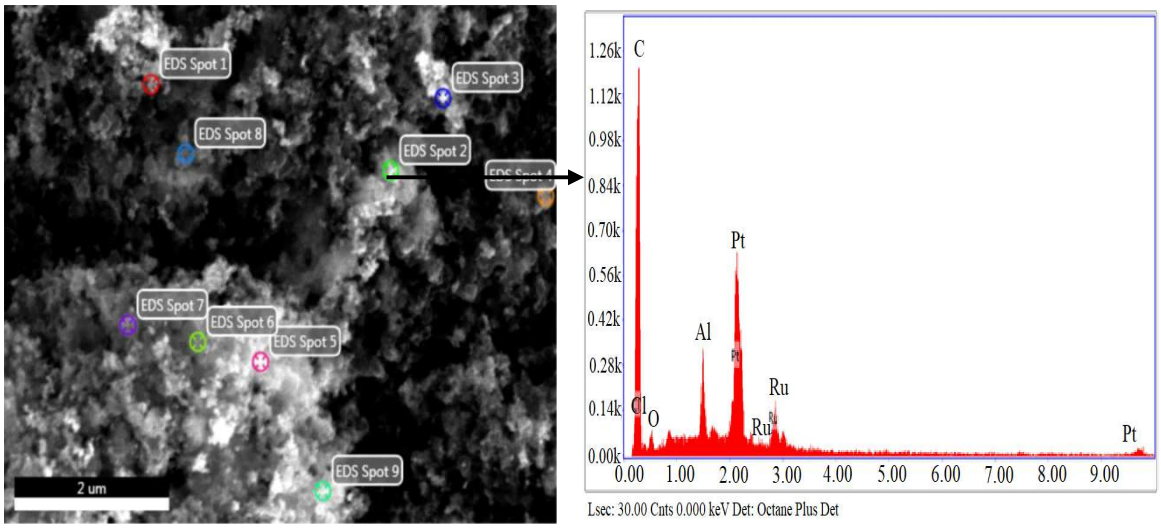

Figure 5.9a EDX pattern of Pt-Ru/C_{PAB}-PLM electrocatalyst.

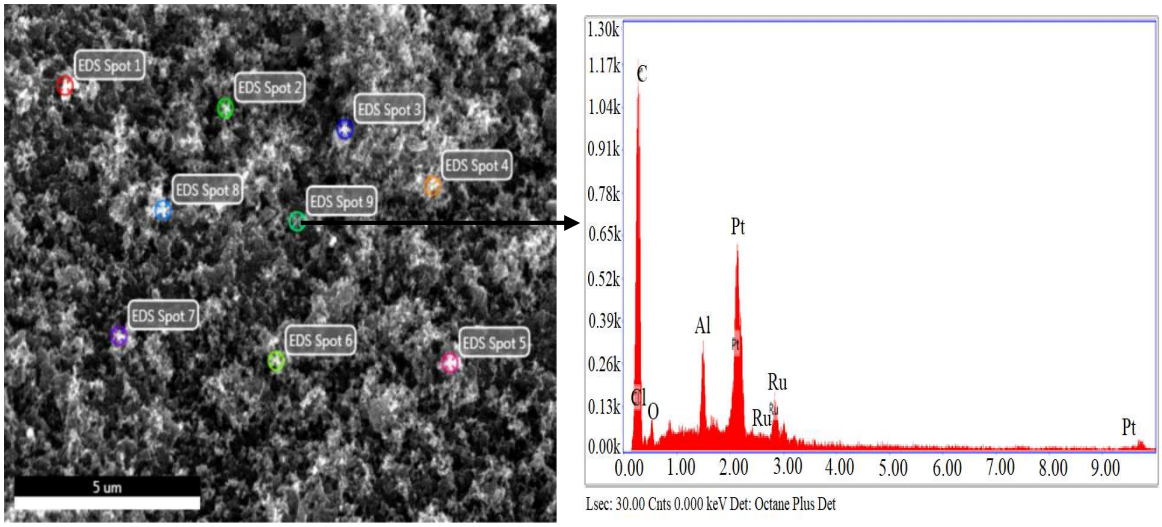

Figure 5.9b EDX pattern of Pt-Ru/C_{PAB}-FAM electrocatalyst.

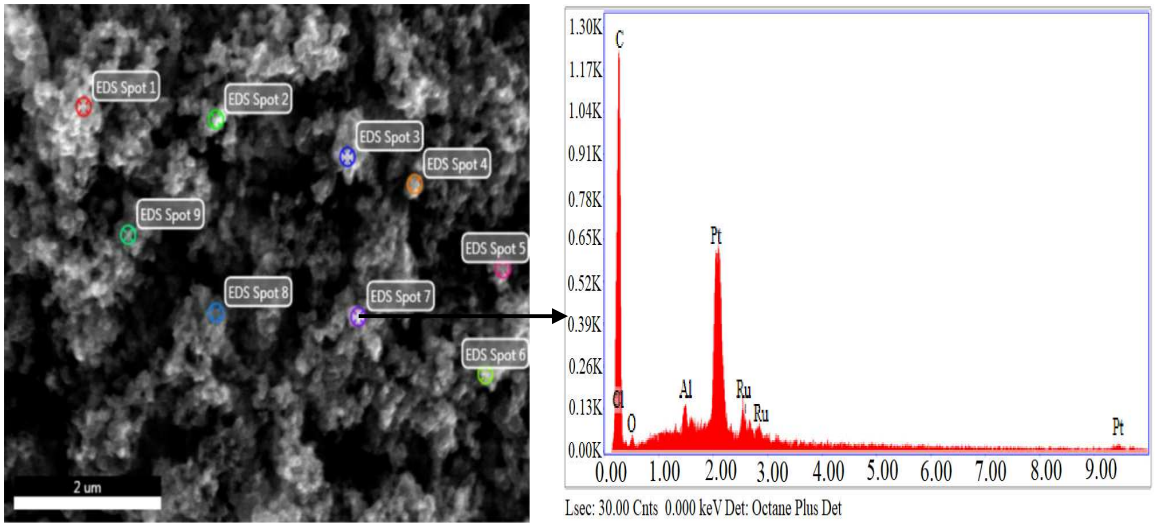

Figure 5.9c EDX pattern of Pt-Ru/C_{AB}-PLM electrocatalyst.

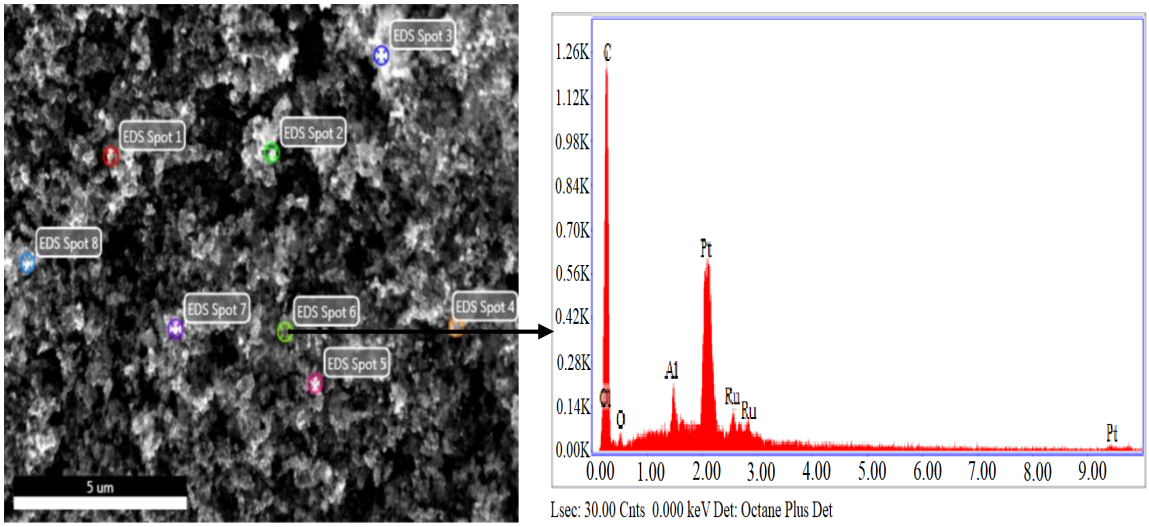

Figure 5.9d EDX pattern of Pt-Ru/C_{AB}-FAM electrocatalyst.

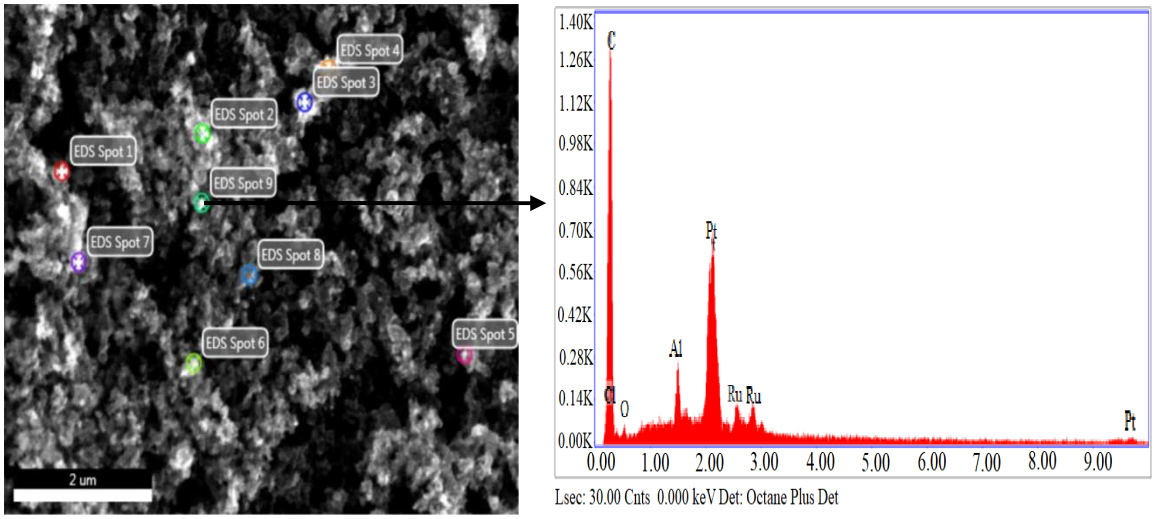

Figure 5.9e EDX pattern of commercial Pt-Ru/C electrocatalyst.

Table 5.6 EDX results of the synthesized Pt-Ru/C_{PAB}-PLM, Pt-Ru/C_{PAB}-FAM, Pt-Ru/C_{AB}-PLM, Pt-Ru/C_{AB}-FAM and commercial Pt-Ru/C electrocatalysts.

Electrocatalysts	**Elements**	**Composition obtained by EDX (wt. %)**	**Nominal composition (wt. %)**
Pt–Ru/C_{PAB}-PLM	Pt	25.10	26.35
	Ru	12.30	13.65
	C	62.60	60
Pt–Ru/C_{PAB}-FAM	Pt	24.70	26.35
	Ru	12.21	13.65
	C	63.09	60
Pt–Ru/C_{AB}-PLM	Pt	25.71	26.35
	Ru	12.93	13.65
	C	61.36	60
Pt–Ru/C_{AB}-FAM	Pt	25.62	26.35
	Ru	12.59	13.65
	C	61.79	60
Commercial Pt–Ru/C	Pt	28.58	30
	Ru	13.74	15
	C	57.68	55

5.1.1.3 Electrochemical characterization of anode electrocatalysts

5.1.1.3.1 Cyclic voltammetry (CV) analysis

Fig (5.10) shows the cyclic voltammograms (CV) of synthesized Pt-Ru/C_{AB}-PLM, Pt-Ru/C_{AB}-FAM, and commercial Pt-Ru/C electrocatalysts for ethanol oxidation using 1 M of C_2H_5OH mixed in 0.5 M of $HClO_4$.

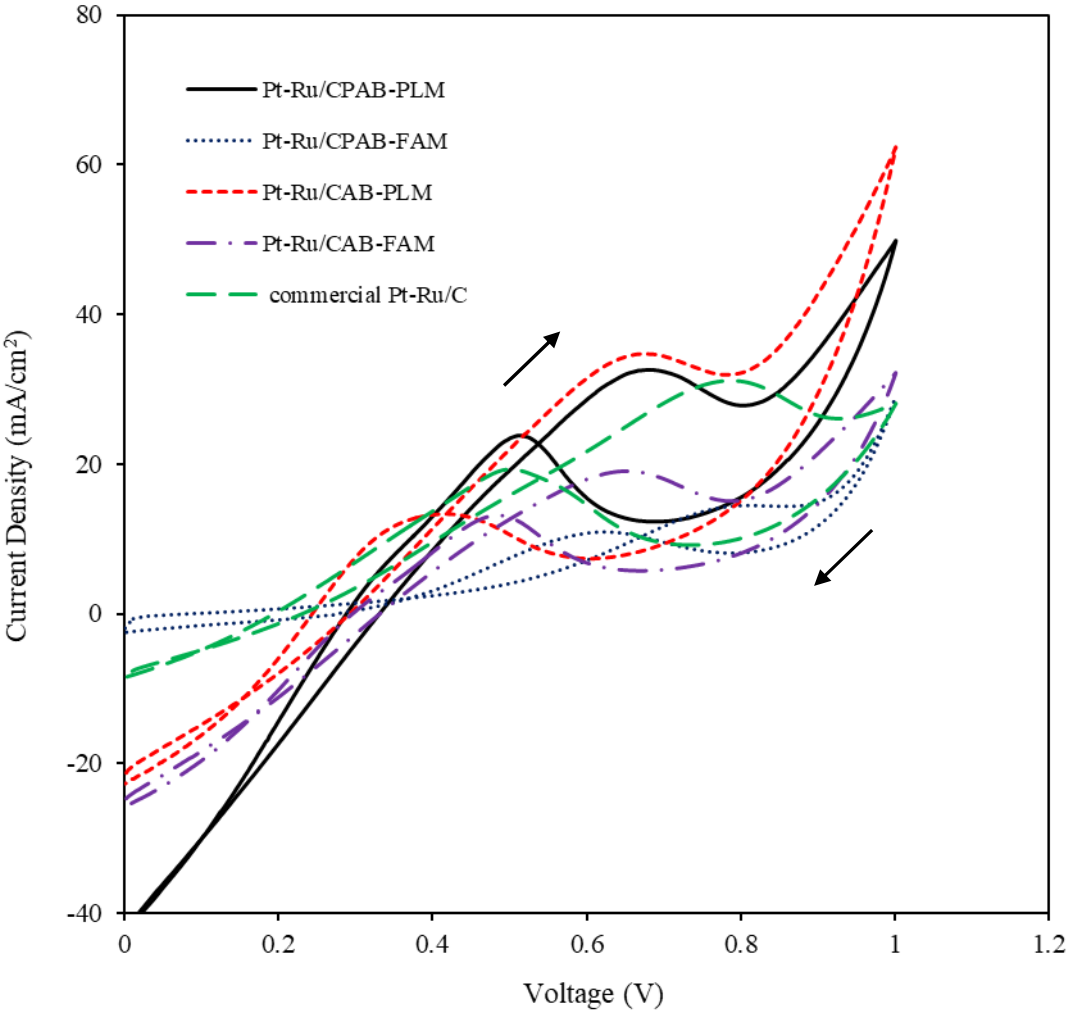

Figure 5.10 CV characteristics of the synthesized Pt-Ru/C_{PAB}-PLM, Pt-Ru/C_{PAB}-FAM, Pt-Ru/C_{AB}-PLM, Pt-Ru/C_{AB}-FAM and commercial Pt-Ru/C electrocatalysts in 0.5 M $HClO_4$ and 1 M ethanol solution at a scan rate of 20 mV/s; Temperature 35° C.

The electrooxidation peaks for ethanol fuel were found in the forward and backward scan as well during the CV study. In the forward scan, the electrooxidation of ethanol produced a prominent anodic peak due to the electrooxidation of freshly chemisorbed species. Fig (5.10) shows that the carbonaceous adsorbed species which are formed during the forward scan are further dissociated via electrooxidation during the backward scan. The noticeable electrooxidation peaks for ethanol fuel on the electrocatalysts Pt-Ru/C_{PAB}-PLM, Pt-Ru/C_{PAB}-FAM, Pt-Ru/C_{AB}-PLM, Pt-Ru/C_{AB}-FAM, and commercial Pt-Ru/C are presented in Table (5.7) including the positive peak potentials and corresponding peak current densities.

It is seen from the CV studies that the ethanol electrooxidation peak current density of 32.59 mA/cm^2 at a potential of 0.686 V was generated during the forward scan for synthesized Pt-Ru/C_{PAB}-PLM electrocatalyst, while Pt-Ru/C_{AB}-PLM produced a little higher peak current density of 34.71 mA/cm^2 at a peak potential of 0.671 V. Similarly, the peak current density of 14.46 mA/cm^2 at a peak potential of 0.805 V was observed for the synthesized Pt-Ru/C_{PAB}-FAM electrocatalyst, while the electrooxidation peak current density of 19.05 mA/cm^2 was observed for Pt-Ru/C_{AB}-FAM at a peak potential of 0.651 V. The CV studies show that the synthesized Pt-Ru supported on functionalized C_{AB} carbon support resulting in better electrocatalytic performance due to their excellent activity in comparison to pristine C_{PAB} carbon-supported electrocatalyst. The onset potential of ethanol electrooxidation on all synthesized electrocatalysts Pt-Ru/C_{AB}-PLM and Pt-Ru/C_{AB}-FAM showed a shift in the potential of 0.115 V and 0.135 V towards less positive in comparison to commercial Pt-Ru/C electrocatalyst. It is observed from Fig (5.10) and Table (5.7) that the ethanol electrooxidation peak potential during a forward scan of synthesized Pt-Ru/C_{AB}-PLM and Pt-Ru/C_{AB}-FAM are in the lowest potential

0.671 V and 0.651 V in comparison to commercial electrocatalyst Pt-Ru/C (0.786 V). It indicates that the loss in potential or overvoltage is low for the synthesized Pt-Ru/C_{AB}-PLM and Pt-Ru/C_{AB}-FAM electrocatalyst. Besides, peak current density is highest (34.71 mA/cm^2) for Pt-Ru/C_{AB}-PLM and thus, possesses the highest catalytic activity towards ethanol oxidation among all anode the electrocatalysts tested. It may be due to better alloying of Ru with Pt atom which plays a very crucial role in the electrooxidation of ethanol fuel and this has already been discussed in XRD analysis. During the backward scan the Pt-Ru/C_{AB}-PLM electrocatalyst resulting in electrooxidation of adsorbed species at a very low potential of 0.419 V.

In the CV study, the ethanol electrooxidation activities of anode electrocatalysts are increased in the following order: Pt-Ru/C_{PAB}-FAM < Pt-Ru/C_{AB}-FAM < commercial Pt-Ru/C < Pt-Ru/C_{PAB}-PLM < Pt-Ru/C_{AB}-PLM based on peak current densities (Table 5.7). The Pt-Ru/C_{AB}-PLM electrocatalyst was synthesized using the polyol reduction method and is supported on functionalized carbon C_{AB}, which is the most active.

Table 5.7 CV results of the synthesized Pt-Ru/C_{PAB}-PLM, Pt-Ru/C_{PAB}-FAM, Pt-Ru/C_{AB}-PLM, Pt-Ru/C_{AB}-FAM, and commercial Pt-Ru/C electrocatalysts at 20 mV/s sweep rate for ethanol electrooxidation.

Electrocatalysts	**Forward scan**		**Backward scan**	
	peak potential (V vs. Ag/AgCl)	**peak current density (mA/cm^2)**	**peak potential (V vs. Ag/AgCl)**	**peak current density (mA/cm^2)**
Pt-Ru/C_{PAB}-PLM	0.686	32.59	0.512	23.82
Pt-Ru/C_{PAB}-FAM	0.805	14.46	0.626	10.95
Pt-Ru/C_{AB}-PLM	0.671	34.71	0.419	13.30
Pt-Ru/C_{AB}-FAM	0.651	19.05	0.483	13.15
Commercial Pt-Ru/C	0.786	31.15	0.500	19.31

5.1.1.3.2 Chronoamperometry (CA) analysis

The chronoamperometry tests of electrocatalysts provide clues on the rate of surface poisoning or stability loss under certain test conditions. The main aim here is to check if there is a rapid poisoning of the electrocatalyst upon ethanol electrooxidation. Chronoamperometry tests for the ethanol electrooxidation at different potentials were carried out at an ethanol concentration of 1 M ethanol mixed with 0.5 M $HClO_4$ and the results are presented in Fig (5.11a) and Fig (5.11b).

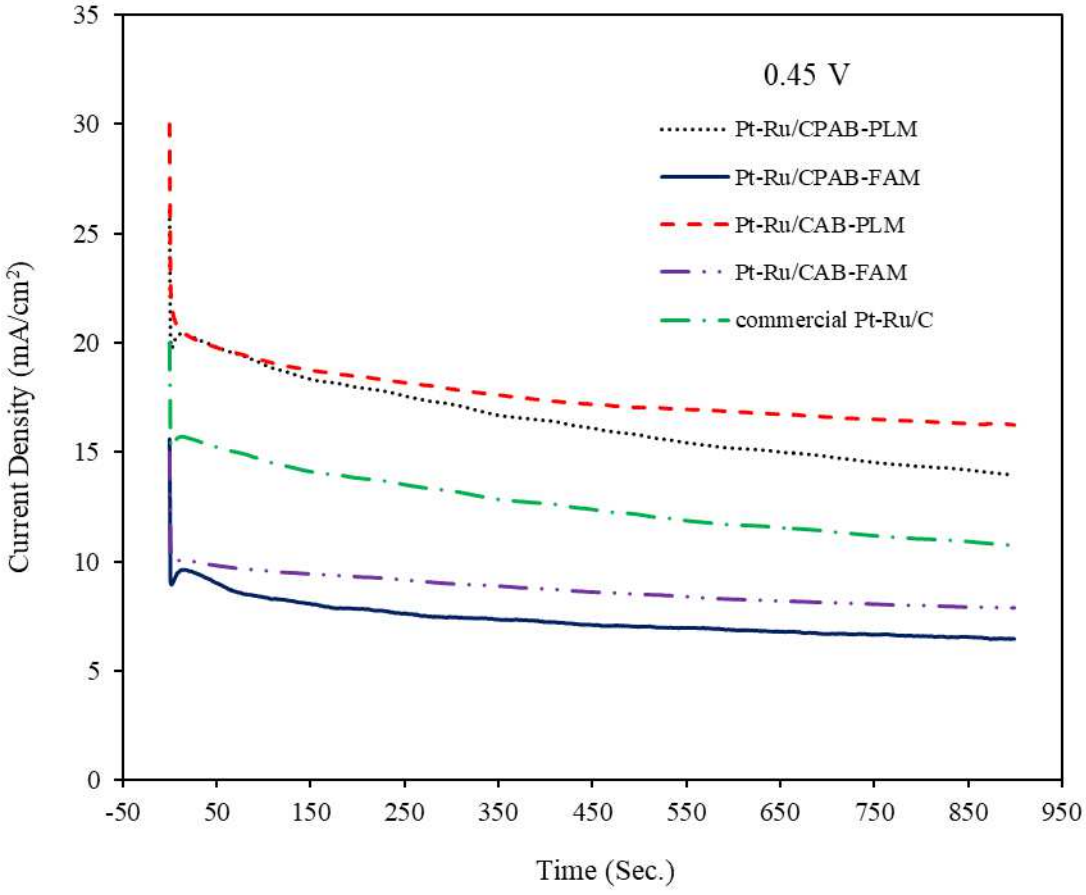

Figure 5.11a CA test of ethanol oxidation in 0.5 M perchloric acid ($HClO_4$) containing 1 M ethanol (C_2H_5OH) solution on synthesized Pt-Ru/C_{PAB}-PLM, Pt-Ru/C_{PAB}-FAM, Pt-Ru/C_{AB}-PLM, Pt-Ru/C_{AB}-FAM and commercial Pt-Ru/C electrocatalysts at 0.45 V vs. Ag/AgCl at room temperature 35 ^{o}C.

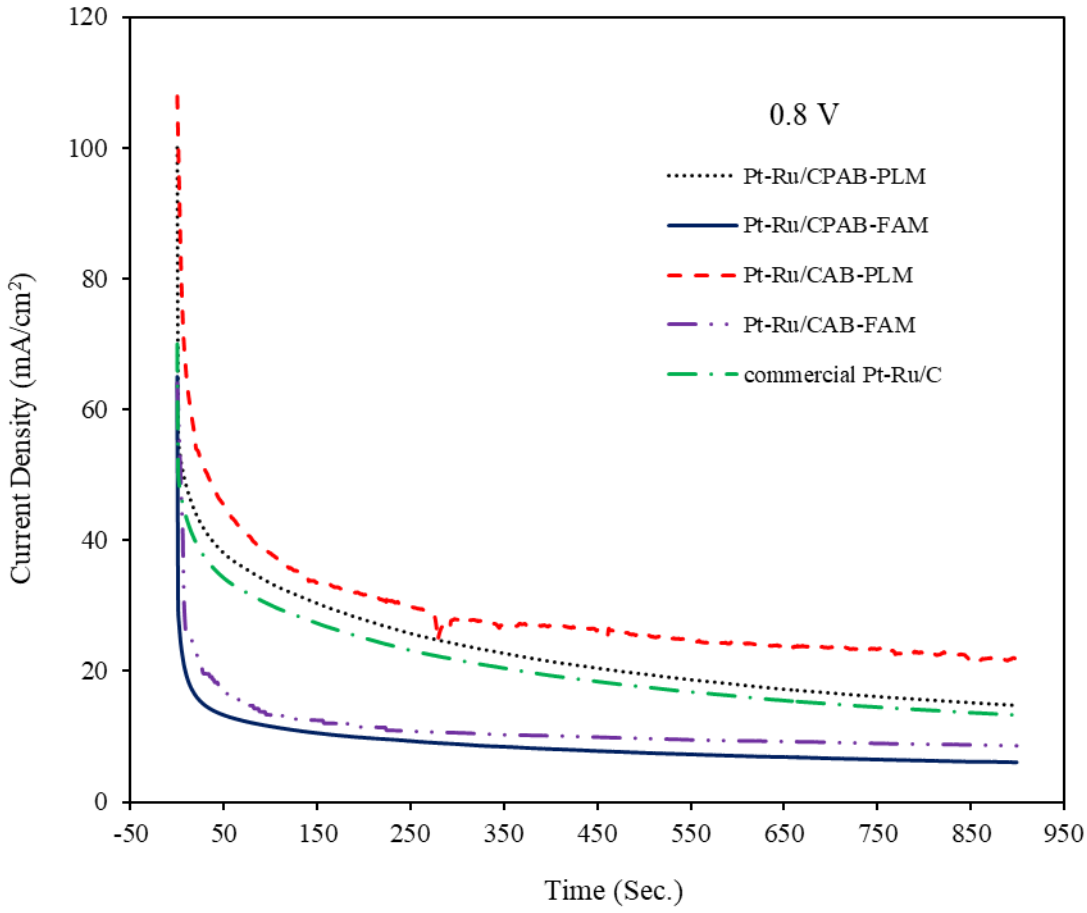

Figure 5.11b CA test of ethanol oxidation in 0.5 M perchloric acid ($HClO_4$) containing 1 M ethanol (C_2H_5OH) solution on synthesized Pt-Ru/C_{PAB}-PLM, Pt-Ru/C_{PAB}-FAM, Pt-Ru/C_{AB}-PLM, Pt-Ru/C_{AB}-FAM and commercial Pt-Ru/C electrocatalysts at 0.8 V vs. Ag/AgCl at room temperature 35 ^{o}C.

It can be observed that currents for ethanol electrooxidation on all the electrocatalysts dropped rapidly and then became relatively stable. The dramatic decrease can be ascribed to diffusion effects and the gradual decrease to the poisoning of electrocatalysts due to the formation of intermediates during ethanol electro-oxidation (Tayal et al., 2011 and Tayal et al., 2012). The reference potential (0.8 V and 0.45V) for the chronoamperometry test were obtained from CV results (Fig 5.10).

It is found that at a lower potential of 0.45 V (Fig 5.11a), the current for ethanol oxidation on Pt-Ru/C_{AB}-PLM electrocatalyst is significantly higher than on all the other

electrocatalysts. Similarly, at the higher potential of 0.8 V (Fig 5.11b), the electrooxidation current on Pt-Ru/C_{AB}-PLM synthesized electrocatalyst is always higher in comparison to synthesized Pt-Ru/C_{PAB}-PLM, Pt-Ru/C_{PAB}-FAM, Pt-Ru/C_{AB}-FAM, and commercial Pt-Ru/C electrocatalysts.

5.1.1.4 Electrochemical characterization of cathode electrocatalysts

It has already been discussed in literature review (Page no. 59) that the oxygen reduction reaction (ORR) proceeds by two possible reaction pathways in acidic medium (i) single step four electron ($4e^-$**)** pathway and (ii) two step 2+2 electron pathways.

Fig 5.12 presents the cyclic voltammograms (CVs) of cathode (Pt/C_{HiSPEC}) at a scan rate of 20 mV/s in 0.5 M $HClO_4$ solution saturated with oxygen or nitrogen gas. In Fig 5.12, the oxygen gas saturated electrolyte (0.5 M $HClO_4$) is represented by a solid line, while the nitrogen gas saturated electrolyte is shown by a dashed line. The cathode electrode was fabricated using commercial electrocatalyst Pt/C_{HiSPEC} with loading of 1 mg/cm^2. Fig 5.12 shows that the single oxygen reduction peak in the reverse scan at 0.47 V for 0.5 M $HClO_4$ solution saturated with oxygen gas. The single oxygen reduction peak for the Pt/C_{HiSPEC} cathode was observed at 0.47 V with a peak current density of -4.83 mA/cm^2 corresponding to the single step four electron (4e-) O_2 to H_2O pathway mechanism, as discussed in the literature review (Equation 2.14, Page no. 59). Whereas no reduction peak is observed during the reverse scan in the presence of nitrogen gas saturated electrolyte, since no dissolved oxygen is present in the electrolyte solution. These results are in good agreement with literature data reported by Guo et al., (2005) and Pramanik and Basu, (2011). In addition, the Pt/C_{HiSPEC} shows well-pronounced peaks associated

with hydrogen adsorption/desorption in potential regions of -0.3 V and 0.1 V, exhibiting a highly electrochemically active surface area of the electrocatalyst (Fig 5.12).

It should be noted that the CV of cathode Pt/C discussed in this section are used for the explanation of experimental results obtained by the DEFC studies using all other synthesized electrocatalysts in **Part-Ib** and **Part-II** also.

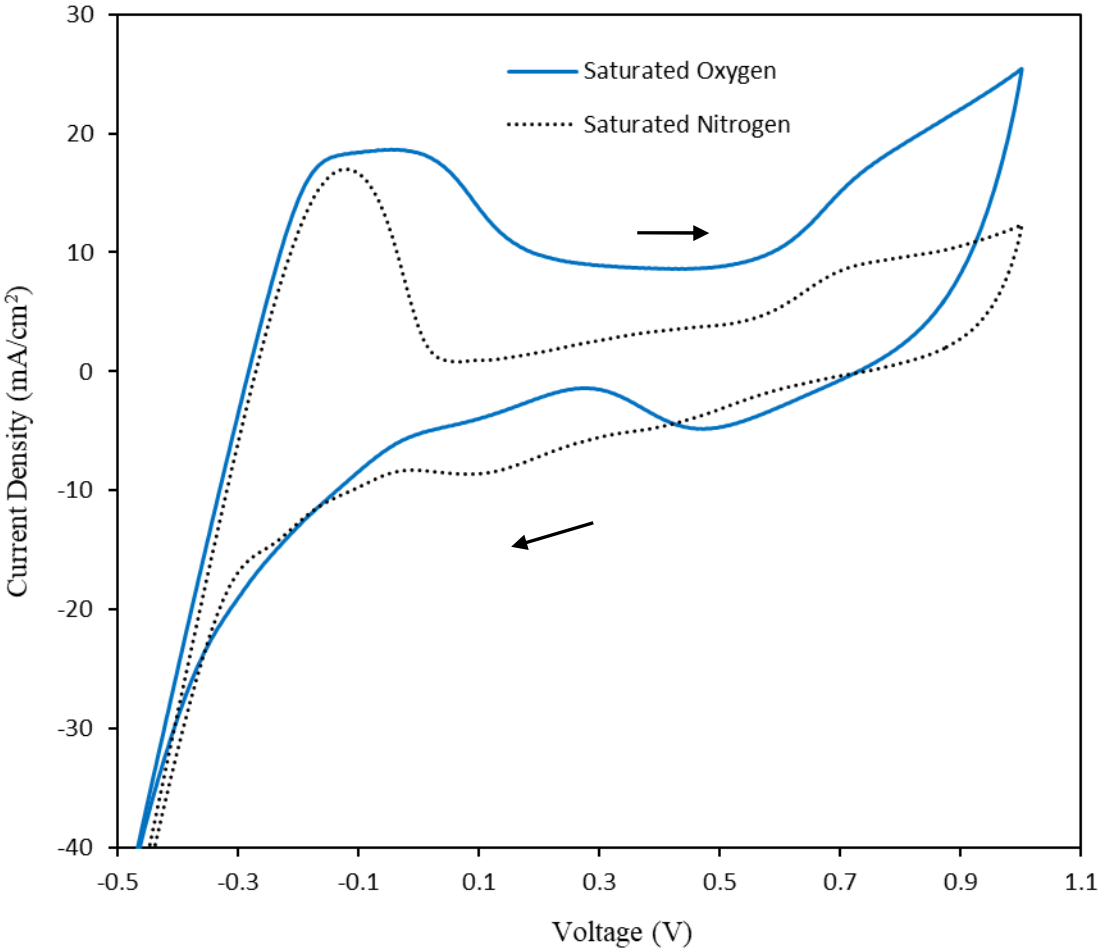

Figure 5.12 Cyclic voltammograms for Pt/C_{HiSPEC} cathode in 0.5 M $HClO_4$ electrolyte solution saturated with pure oxygen or nitrogen gas at a scan rate of 20 mV/s; room temperature of 30 ºC.

5.1.1.5 DEFC study

5.1.1.5.1 Effect of electrocatalyst type

The electrocatalytic activities of the synthesized and commercial electrocatalysts were tested in a DEFC single cell setup which is presented in Fig (5.13). Electrocatalyst loading at the anode was 1 mg/cm^2 of synthesized Pt-Ru/C_{PAB}-PLM, Pt-Ru/C_{PAB}-FAM, Pt-Ru/C_{AB}-PLM, Pt-Ru/C_{AB}-FAM and commercial Pt-Ru/C electrocatalysts, respectively. The cathode was made of commercial Pt/C_{HiSPEC} of fixed loading i.e., 1 mg/cm^2.

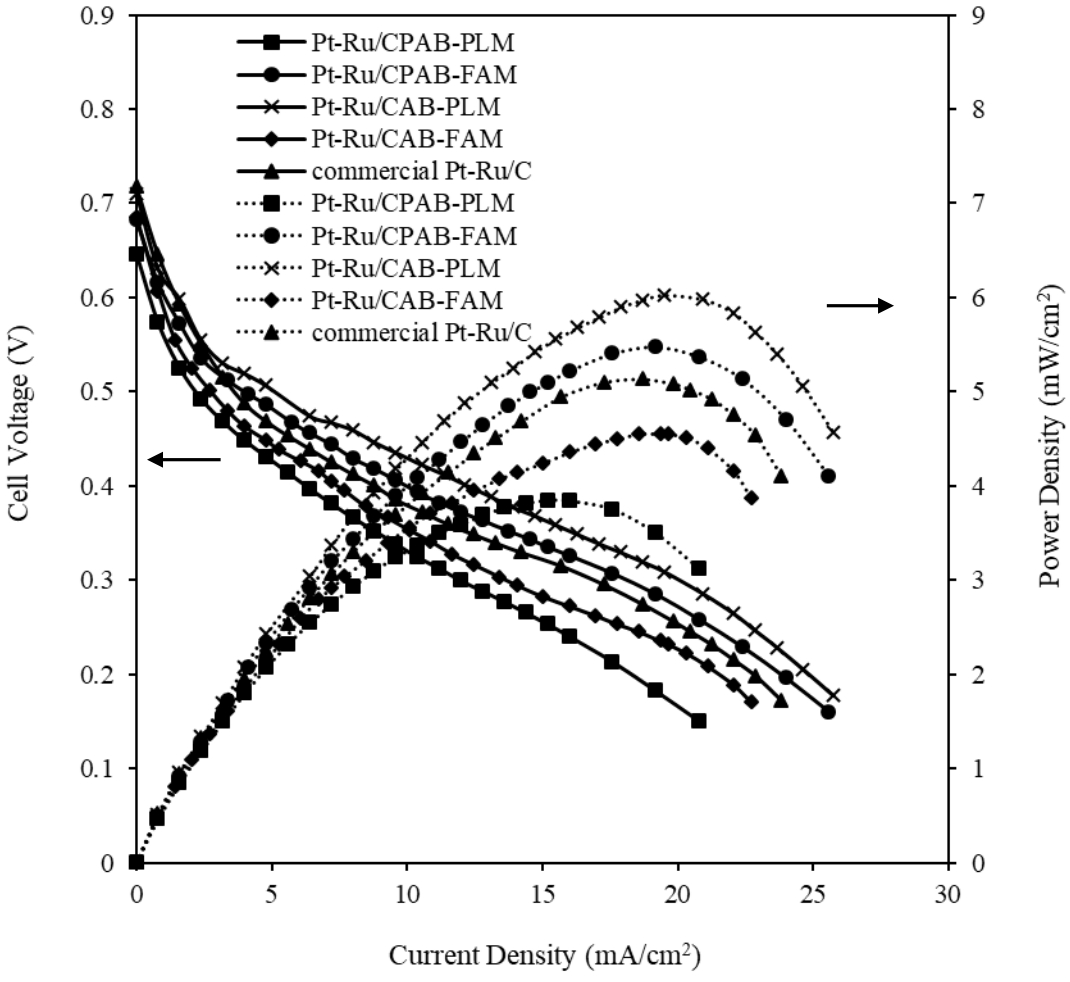

Figure 5.13 Single cell performance characteristics for different anode electrocatalysts for anode feed of 1 M ethanol. Cathode feed: humidified pure oxygen; $P_{cathode}$ = 1 bar (absolute); Solid line-polarization curves; Dotted line-power density curves.

The electrolyte used was a commercial Nafion® 117 membrane. The DEFC was operated at a temperature of 35 °C which was kept similar to that of CV experiments performed. As observed in CV experiments (Fig 5.10), Pt-Ru/C_{AB}-PLM resulted in a comparable performance with the commercial Pt-Ru/C electrocatalyst in the DEFC test also (Fig 5.13).

It is observed from the single cell study, the synthesized electrocatalysts supported functionalized carbon support (C_{AB}) resulting in enhanced cell performance in comparison to pristine carbon support (C_{PAB}) while adopting the same synthesis method. Moreover, electrocatalyst synthesized via the PLM method always showed better performance in terms of current and power density than any other electrocatalysts tested in the present DEFC. The maximum OCV of 0.71 V was obtained for Pt-Ru/C_{AB}-PLM, which is near about the same that of the commercial Pt-Ru/C (0.717 V) electrocatalyst. Synthesized electrocatalyst Pt-Ru/C_{AB}-FAM produced relatively lower OCV 0.685 V than Pt-Ru/C_{AB}-PLM and commercial Pt-Ru/C (0.717 V) electrocatalyst. The DEFC constructed with synthesized Pt-Ru/C_{AB}-PLM anode electrocatalyst yielded a maximum power density of 6.02 mW/cm^2, which is higher than with commercial Pt-Ru/C electrocatalyst (5.13 mW/cm^2) and with synthesized Pt-Ru/C_{AB}-FAM electrocatalyst (4.54 mW/cm^2). For both Pt-Ru/C_{PAB}-PLM and Pt-Ru/C_{PAB}-FAM electrocatalysts, the maximum power density of 5.47 mW/cm^2 and 3.85 mW/cm^2 were obtained at a current density of 19.20 mA/cm^2 and 15.20 mA/cm^2, respectively. After treatment of pristine acetylene black, there is an increase in OCV of Pt-Ru/C_{AB}-PLM and Pt-Ru/C_{AB}-FAM anode electrocatalysts, which indicates a difference in ethanol electrooxidation reaction mechanism due to the presence of oxygenated surface groups at the surface of functionalized carbon C_{AB} as explained in FTIR section (Goel and Basu, 2014).

A rapid fall in cell voltage was observed for all electrocatalysts, which may be due to the slow initial ethanol electrooxidation reaction at the electrode surface. Moreover, metal particles are well dispersed on polyol method synthesized electrocatalyst (Pt-Ru/C_{AB}-PLM) and thus showed better performance than the commercial Pt-Ru/C electrocatalyst. Enhanced performance of Pt-Ru/C_{AB}-PLM synthesized electrocatalyst could also be attributed to the positive effect of functionalized acetylene black (C_{AB}) as support having high electrical conductivity, large pore volume, and more uniform distribution of the ionomer in the anode electrocatalyst layer which could result in enhanced ethanol electrooxidation kinetics to give the highest current density of 19.52 mA/cm^2. The XPS results also predicted better performance for synthesized Pt-Ru/C-PLM electrocatalysts (Fig 5.7). Due to the highest electrocatalytic activity of the synthesized electrocatalyst Pt-Ru/C_{AB}-PLM, it was used as an anode electrocatalyst for optimization of other operating parameters like concentration and temperature, which are presented in the next section.

5.1.1.5.2 Effect of ethanol concentration

Fig (5.14) shows the effect of ethanol concentration on the polarization and power density curves using the synthesized Pt-Ru/C_{AB}-PLM as the anode and Pt/C_{HiSPEC} as cathode electrocatalyst, respectively. The fixed electrocatalyst loading of 1 mg/cm^2 was applied to both electrodes. The cathode oxidant used was humidified oxygen. It is seen from Fig (5.14) that the cell performance in terms of voltage and current increases with the increase in ethanol concentration from 0.5 M to 2 M, while further increase in concentration to 3 M, the cell performance decrease. Adequate fuel ethanol is unable to reach the electrocatalyst layer at a very low ethanol concentration of 0.5 M to sustain the increased current density and thus the cell output unexpectedly decreases due to

limitations in mass transport. Similar results have already been reported by Song et al., (2005) and Pramanik and Basu, (2007).

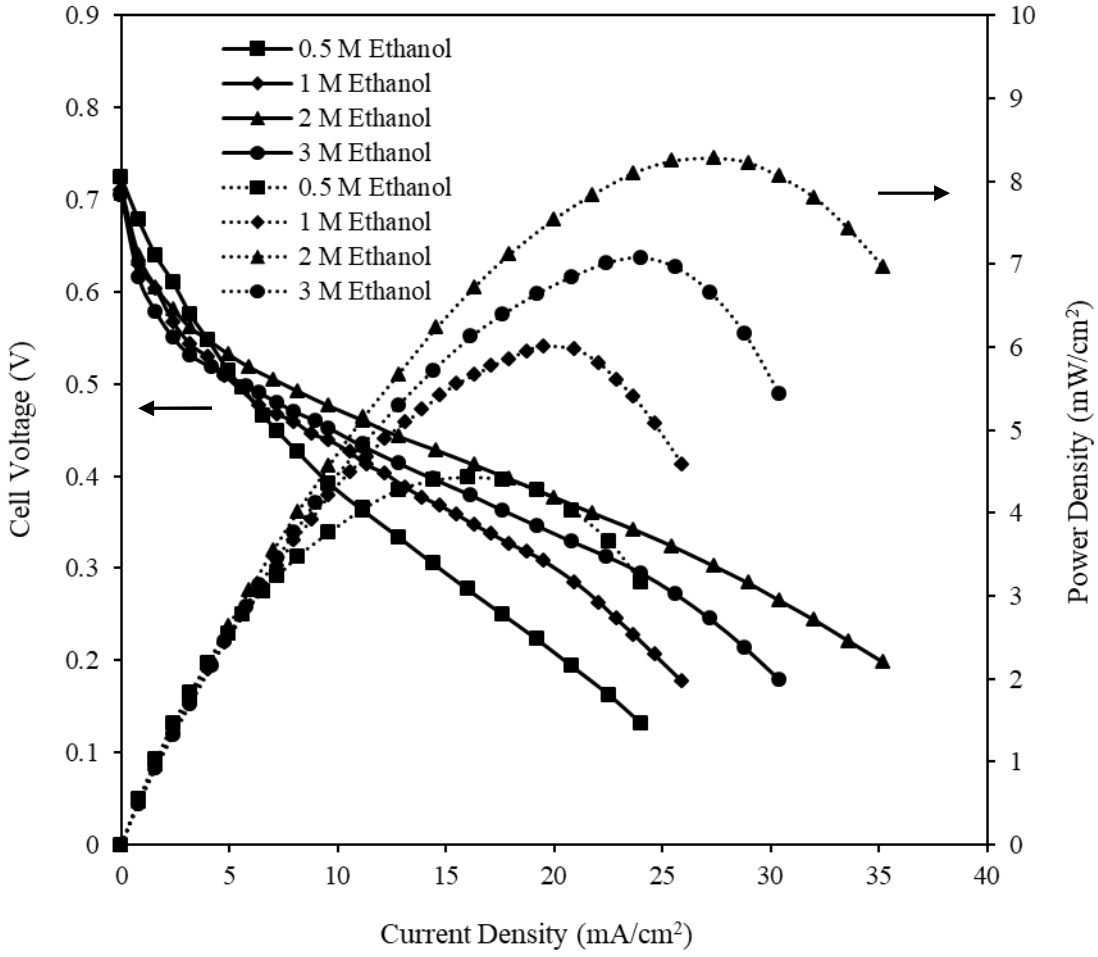

Figure 5.14 Single cell performance characteristics for anode electrocatalyst Pt-Ru/C_{AB}-PLM using varying ethanol concentration as anode feed at a cell temperature of 35 °C. Cathode feed: pure humidified oxygen; $P_{cathode}$ = 1 bar (absolute); Dotted line-power density curves; Solid line- polarization curves.

The maximum OCV of 0.712 V and maximum power density of 8.28 mW/cm^2 at a current density of 27.36 mA/cm^2 were obtained for the ethanol concentration of 2 M. Whereas, the ethanol concentration of 1 M and 3 M produced a maximum power density of 6.02 mW/cm^2 at a current density of 19.52 mA/cm^2 and maximum power density of 7.08 mW/cm^2 at a current density of 24 mA/cm^2, respectively. The ethanol concentration

of 0.5 M generated a very low power density of 4.4 mW /cm^2 at a current density of 17.60 mA/cm^2.

With an increase in ethanol concentration, the current density increases due to an improvement in the reaction rate at a higher ethanol concentration, which could facilitate an increase in the diffusion of ethanol concentration to the electrocatalyst layer (Larminie and Dicks, 2003, Heysiattalab et al., 2011 and Alzate et al., 2011). However, at a higher ethanol concentration of 3 M, the cell performance decreases due to blockage of active sites of electrocatalyst at a high concentration which hinders the availability of water molecules to the active sites. Moreover, excess unreacted ethanol may cross through the polymeric membrane on the cathode side. The cross-ethanol fuel results in a mixed potential and cathode electrocatalyst poisoning that reduce cell performance (Azam et al., 2019).

Although, not shown here a similar trend for ethanol concentration dependence is also observed for Pt-Ru/C_{AB}-FAM and commercial Pt-Ru/C as anode electrocatalysts. The detailed single cell studies are presented in Appendix C (Fig C.1 and Fig C.2, Page no. 279, 280).

5.1.1.5.3 Effect of cell temperature

The effects of temperature on cell performance are performed for the synthesized electrocatalyst Pt-Ru/C_{AB}-PLM only, as it produces the highest power density at room temperature of 35 ^oC. Fig (5.15) illustrates the effect of cell temperatures using the synthesized Pt-Ru/C_{AB}-PLM of 1 mg/cm^2 as the anode and Pt/C_{HiSPEC} as cathode electrocatalyst, respectively. It is observed in Fig (5.15) that the maximum power density and current density both increase with the increase in temperature of up to 80 ^oC. It

should be noted that the maximum cell temperature was maintained at 80 ^{o}C given the boiling point of ethanol of about 78.4 ^{o}C. The temperature dependence of cell performance indicates ethanol electrooxidation kinetics on synthesized Pt-Ru/C_{AB}-PLM electrocatalyst is thermally activated.

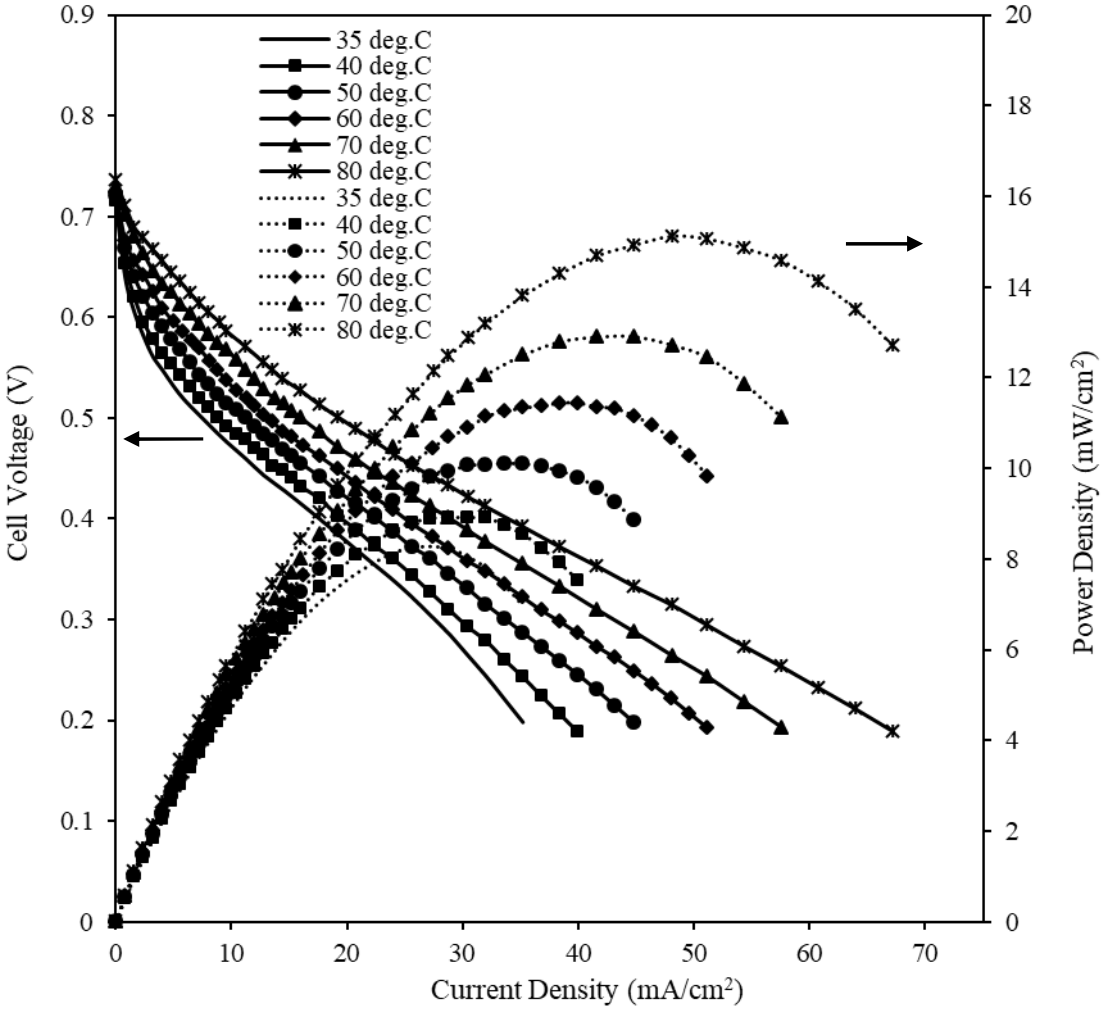

Figure 5.15 Single cell performance characteristics for varying cell temperatures using an anode feed of 2 M ethanol solution. Cathode feed: pure humidified oxygen; $P_{cathode}$ = 1 bar (absolute); Dotted line-power density curves; Solid line- polarization curves.

It is reported in the literature, high temperature not only reduces activation overpotential but ohmic and concentration overpotential also. At high temperature (T < 80 ^{o}C), the

proton conductivity of the Nafion® membrane is significantly improved, which results in decreased ohmic polarization (Alzate et al., 2011). Additionally, the high operating temperature of cell operation also favors the mass transfer rate of the reactant and thus, decreasing the concentration overpotential (Goel and Basu, 2012). The OCV of the single DEFC also increases due to the positive effect of temperature and this could be explained by the Nernst equation (Larminie and Dicks, 2003). The maximum power density of 8.28 mW/cm^2 at a current density of 27.36 mA/cm^2 was obtained when the cell was functioning at room temperature of 35 °C. However, DEFC performance was improved significantly at the highest operating temperature of 80 °C. The maximum OCV of 0.736 V and maximum power density of 15.12 mW/cm^2 at a current density of 48.16 mA/cm^2 were achieved at this temperature (80 ^oC). A noticeable increase in the power density i.e., about 83 % was achieved for the temperature increase from 35 ^oC to 80 ^oC. The effect of temperature on DEFC performance for the anode using commercial electrocatalyst Pt-Ru/C is presented in Appendix D (Fig D.1, Page no. 281).

5.1.2 Post treated bi-metallic electrocatalysts supported on C_{AB}: Part-1b

The physical characterization of support material C_{AB} has been reported in section 5.1.1.1 (Page no. 108). The important physicochemical properties, electrochemical properties, and performance of post-treated polyol synthesized Pt-based bi-metallic electrocatalysts supported on C_{AB} are discussed below in detail. It should be noted that the modified polyol synthesis method (PLM) was adopted here for electrocatalyst synthesis and its post treatment as this route PLM produced most active electrocatalyst Pt-Ru/C_{AB}-PLM which are discussed in the **Part-Ia** (Page no. 138).

5.1.2.1 Physical characterization of electrocatalysts

5.1.2.1.1 X-ray diffraction (XRD) analysis

The XRD measurements were obtained to investigate the crystal characteristics of electrocatalysts and results are presented in Fig (5.16). The first broad diffraction peak at around $2\theta = 25.3^{o}$ is associated with the carbon/graphite (002) crystalline plane of its hexagonal structure for all the samples. The Pt-Ru/C_{AB}-syn fresh electrocatalyst display a broad diffraction peak at 38.7^{o} which is due to the superposed effect of RuO_2 at 35.2^{o} (101) and Pt diffraction peak at 39.7^{o} (111), while the other diffraction peaks at Pt (200), Pt (220), Pt (311) and Pt (222) are too weak to be observed. The XRD pattern of Pt-Ru/C_{AB}-syn electrocatalyst reveals its poor crystalline structure. After the post-treatment in a reductive (H_2) atmosphere, the RuO_2 peaks disappear from the post-treated Pt-Ru/C_{AB}-H_2-RT and Ru/C_{AB}-H_2-160 electrocatalysts. However, post-treated in an oxidative (air) atmosphere increased the crystallinity of Pt-Ru/C_{AB}-Air-160 electrocatalyst. The three additional peaks at 28.1^{o}, 35.2^{o} and 54.4^{o} were observed for Pt-Ru/C_{AB}-Air-160 electrocatalyst can be indexed to the (110), (101) and (211) planes of

anhydrous crystalline rutile RuO_2 (JCPDS no. 43-1027). This suggests that the RuO_2 and Pt phase are separated further during post-treatment under an oxidative atmosphere.

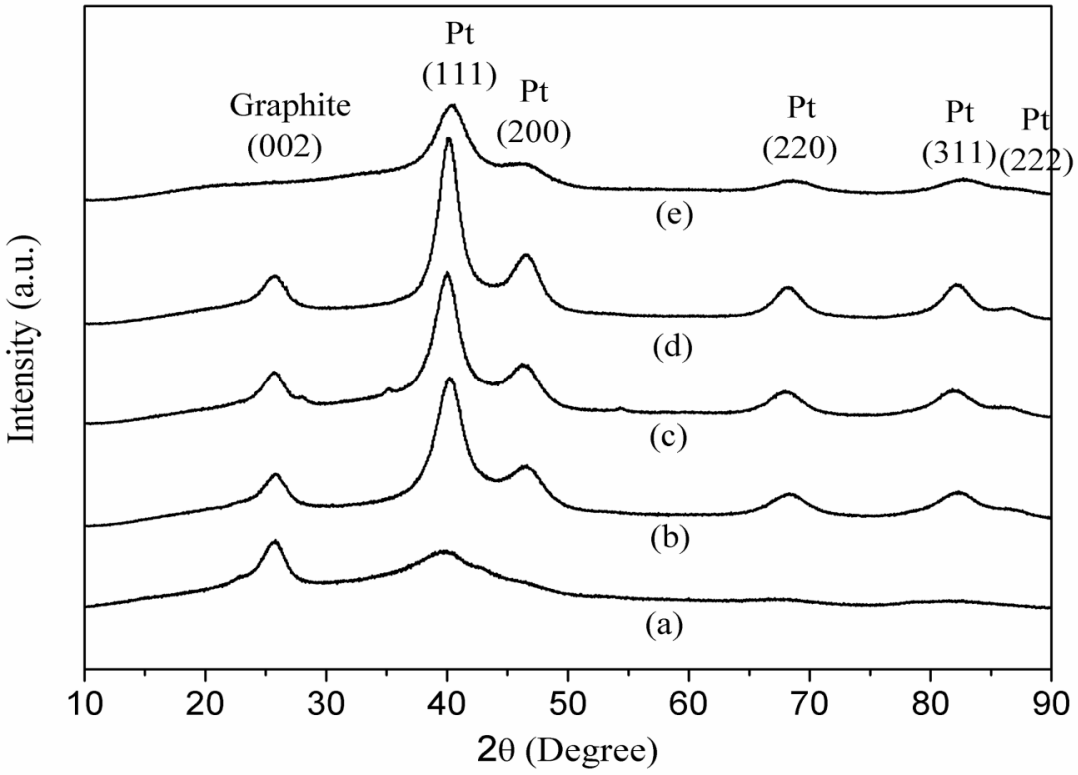

Figure 5.16 XRD patterns of (a) Pt-Ru/C_{AB}-syn, (b) Pt-Ru/C_{AB}-H_2-RT, (c) Pt-Ru/C_{AB}-Air-160, (d) Ru/C_{AB}-H_2-160 and (e) commercial Pt-Ru/C electrocatalysts.

The lack of characteristic diffraction peaks of metallic Ru or Ru oxides/hydroxides in the XRD patterns of the post-treated under reductive atmosphere and commercial electrocatalysts, suggests that Ru atoms form a metal alloy with Pt atoms or exist as oxides in the amorphous form (Chu et al., 2010 and Hu et al., 2016). On the other side, the XRD patterns of Pt-Ru/C_{AB}-H_2-RT, Pt-Ru/C_{AB}-Air-160, Pt-Ru/C_{AB}-H_2-160, and commercial Pt-Ru/C electrocatalysts represent the typical face-centered cubic (FCC) crystalline Pt diffraction peaks. The XRD patterns of all the Pt-Ru/C electrocatalysts

samples except Pt-Ru/C_{AB}-sny showed the Pt diffraction peaks shifting to a higher 2θ degree compare to pure Pt diffraction peaks, which reveals that the Ru atoms (smaller than Pt) are incorporated into Pt crystal lattice to form an FCC solid solution between Pt and Ru. The Pt (220) peak was selected to estimate the average crystallite size (d_c) of electrocatalysts samples based on the Debye Scherrer's equation (Equation 3.4). The Pt (220) peak was chosen due to its relative isolation from carbon contributions. The average crystallite size of the Pt-Ru/C_{AB}-syn electrocatalyst could not be calculated due to the weak intensity of Pt (220) diffraction peak.

The Ru atomic fraction (x_{Ru}) in the bimetallic Pt-Ru/C electrocatalysts were measured using Vegard's law Equation (5.1) (Antolini and Cardellini, 2001 and Pires et al., 2013), which is based on the shifting of Pt diffraction peaks and variation in lattice parameters from the XRD patterns. The values of x_{Ru} calculated via Equation (5.1) of all the bi-metallic electrocatalysts are reported in Table (5.8).

Table 5.8 Data obtained from XRD patterns of electrocatalysts analyses by the Debye Scherrer's equation (Equation 3.4) and Vegard's law (Equation 5.1).

Electrocatalysts	**Average crystallite size (d_c) (nm)**	**Lattice parameter (a) (nm)**	**Pt (2 2 0) peak position 2θ (°)**	**Ru fraction (x_{Ru})**	**Alloyed Ru (wt. %)**
Pt-Ru/C_{AB}-syn	---	0.3913	67.63	0.024	2.49
Pt-Ru/C_{AB}-H_2-RT	3.2	0.3880	68.30	0.290	40.84
Pt-Ru/C_{AB}-Air-160	3.5	0.3899	67.90	0.137	15.87
Pt-Ru/C_{AB}-H_2-160	3.8	0.3889	68.11	0.217	27.71
Commercial Pt-Ru/C	2.8	0.3877	68.35	0.315	45.98

The resulting average crystallite size, lattice parameters, and alloying degree related to Pt (220) peak of the electrocatalysts from the XRD patterns are presented in Table (5.8). The alloying degree of Ru (Ru_{alloy}) in the bi-metallic supported Pt-Ru electrocatalysts was calculated using the relationship Equation (5.2) as already discussed. The average crystallite sizes for Pt (220) of the Pt-Ru/C_{AB}-H_2-RT, Pt-Ru/C_{AB}-Air-160, Pt-Ru/C_{AB}-H_2-160, and commercial Pt-Ru/C electrocatalysts were calculated to be 3.2 nm, 3.5 nm, 3.8 nm, and 2.8 nm, respectively. It is also observed that the lattice parameters of the Pt-Ru/C_{AB} electrocatalysts are in the range of 0.3877−0.3899 nm, which is lower than that of pure Pt (0.3923 nm) or Pt/C (a = 0.3916 nm) (dos Santos et al., 2006 and Guo et al., 2007). The alloying degree of the Pt-Ru/C_{AB}-H_2-RT electrocatalyst was as high as 40.84 %. Whereas, freshly synthesized electrocatalyst Pt-Ru/C_{AB}-syn showed Ru alloying of 2.49 % only. This indicates that most of the RuO_2 in the as-synthesized Pt-Ru/C_{AB}-syn electrocatalyst is further reduced by the H_2 flow at room temperature and improves its alloy formation. When the post-treatment reduction temperature was increased to 160 °C in the presence of H_2 flow, caused drastic agglomeration of crystallite size and alloying degree of Ru/C_{AB}-H_2-160 was lower (27.71 %) than that of post-treated electrocatalyst at room temperature/Pt-Ru/C_{AB}-H_2-RT (40.84 %). The post-treated electrocatalyst in the presence of air at a temperature of 160 °C (Pt-Ru/C_{AB}-Air-160) showed the lowest alloying degree of about 15.87 % due to lack of reducing environment. It is clearly observed in Table (5.8) that the amount of Ru alloyed with Pt is smaller than nominal values, which suggest that a part of Ru is present as oxides in the amorphous form on the electrocatalyst surface and cannot be detected by XRD measurements (Datta et al., 2009 and Hu et al., 2016).

5.1.2.1.2 FESEM-EDX analysis

The FESEM images and corresponding EDX patterns of the synthesized and commercial bimetallic electrocatalysts are presented in Fig (5.17a) to Fig (5.17e). The elemental compositions and metal loading on the carbon support of the electrocatalysts are examined by the EDX spectrum. It is clearly seen in Fig (5.17a) to Fig (5.17e) that the electrocatalysts particles are of nano-range and their surface morphology is uniform. The FESEM images also confirm that the synthesized electrocatalysts are made of porous spherical particles which could facilitate mass transport from the bulk phase to the active electrocatalysts sites.

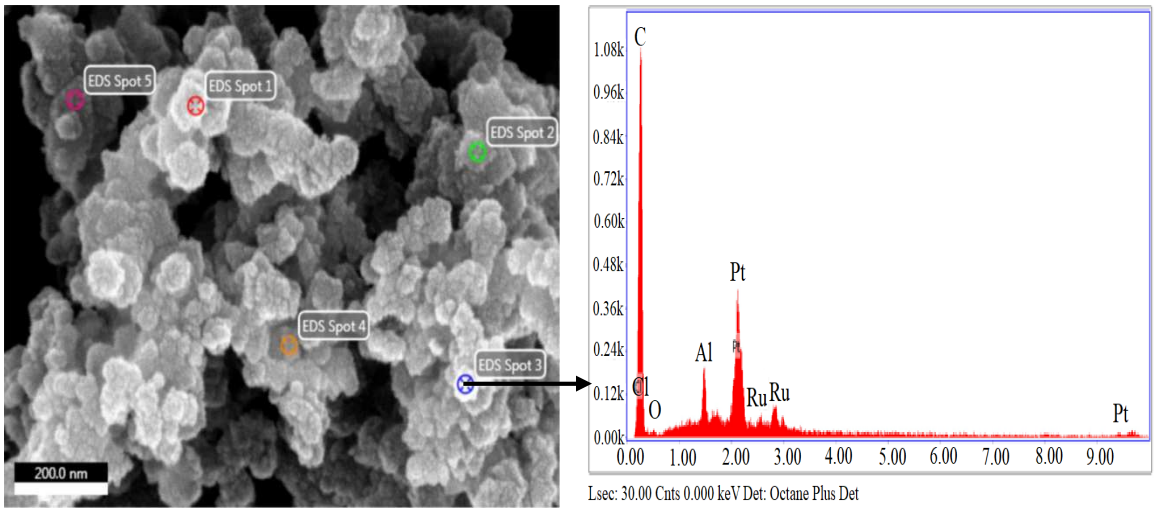

Figure 5.17a FESEM image and corresponding EDX pattern of Pt-Ru/C_{AB}-syn electrocatalyst.

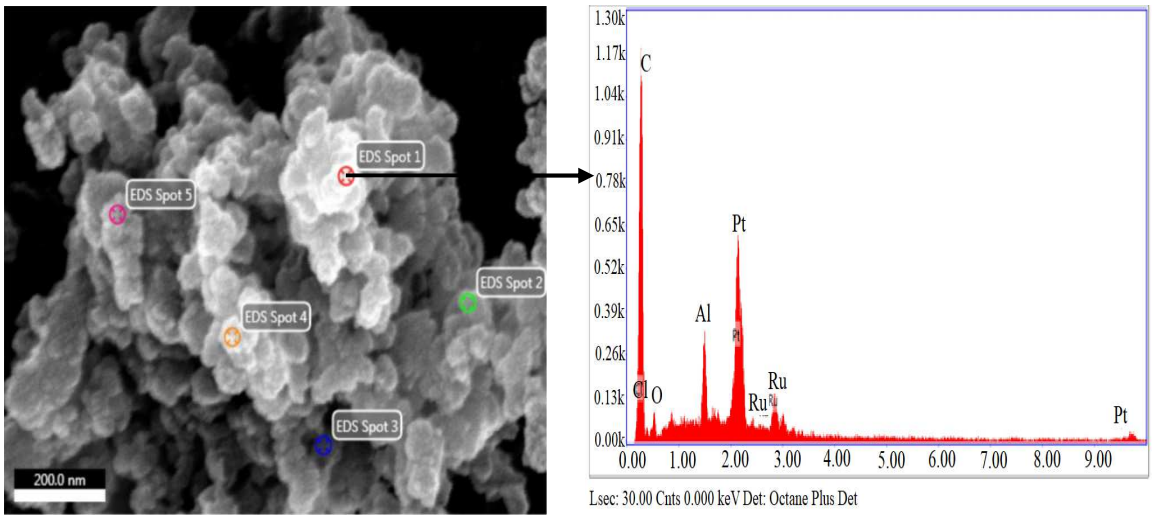

Figure 5.17b FESEM image and corresponding EDX pattern of Pt-Ru/C_{AB}-H_2-RT electrocatalyst.

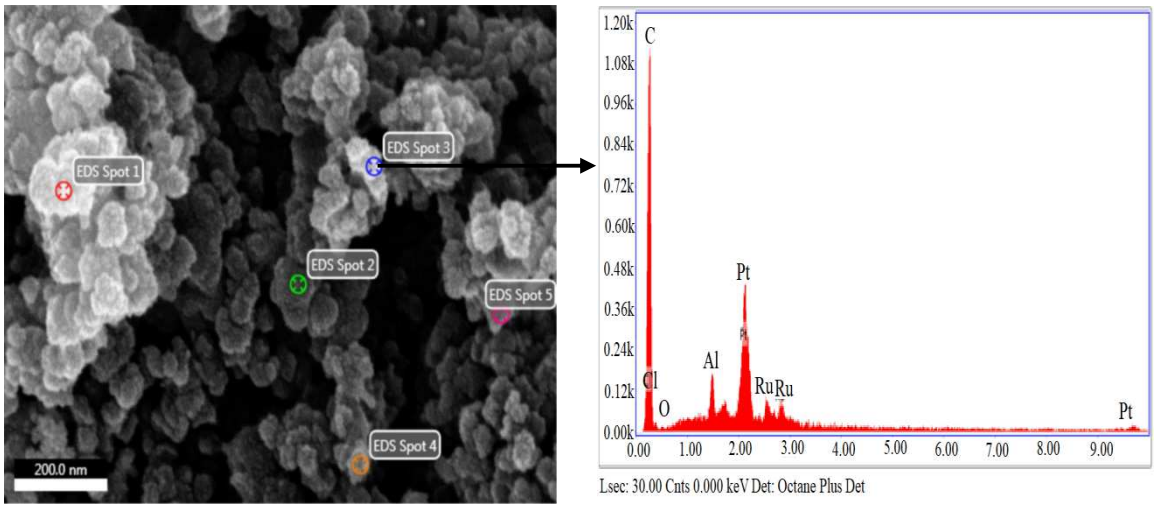

Figure 5.17c FESEM image and corresponding EDX pattern of Pt-Ru/C_{AB}-Air-160 electrocatalyst.

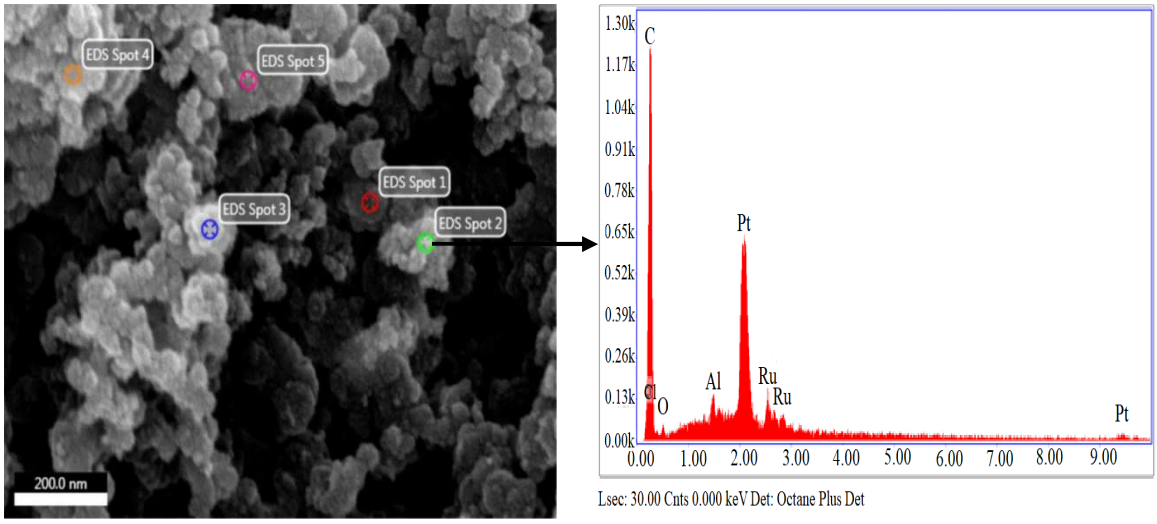

Figure 5.17d FESEM image and corresponding EDX pattern of Ru/C_{AB}-H_2-160 electrocatalyst.

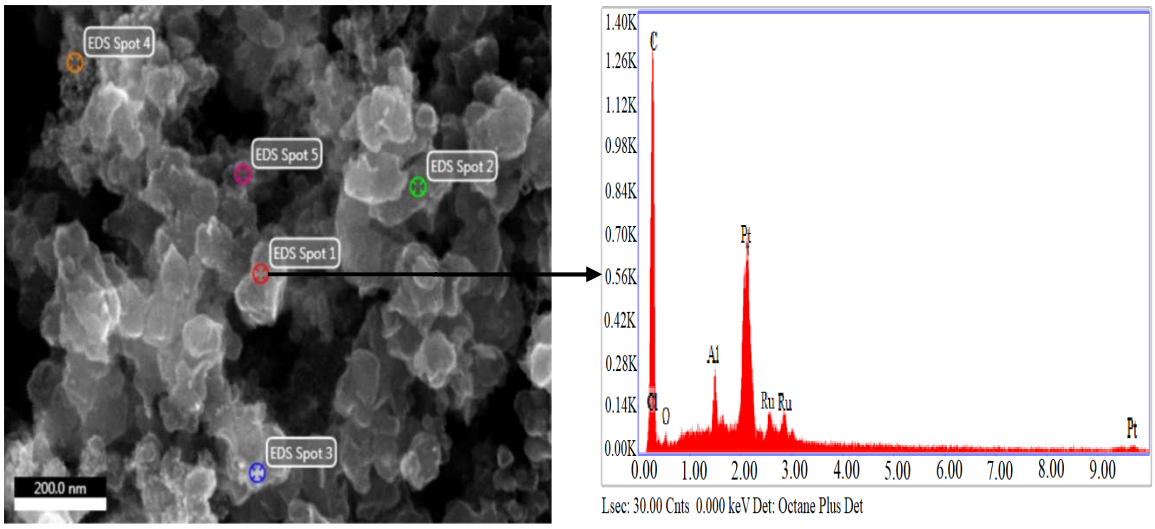

Figure 5.17e FESEM image and corresponding EDX pattern of commercial Pt-Ru/C electrocatalyst.

The EDX spectrum of all the electrocatalysts reveals the presence of desired elements such as Pt, Ru, and C respectively; which can be ascribed to the Pt-Ru electrocatalyst nanoparticles supported on the carbon support. The strongest C peaks in all EDX patterns were observed due to the presence of the acetylene black support material. Post-treatment does not promote significant alterations in the EDX nominal values. The average

elemental compositions of all the electrocatalysts evaluated by EDX analyses are summarized in Table (5.9). Total metal loading on the carbon support was around 40 wt. % and was similar in each case. The desired elements compositions were nearly in good agreement with the nominal compositions with some variations.

Table 5.9 EDX compositions of synthesized Pt–Ru/C_{AB}-syn, Pt–Ru/C_{AB}-H_2-RT, Pt–Ru/C_{AB}-Air-160, Pt–Ru/C_{AB}-H_2-160 and commercial Pt-Ru/C electrocatalysts.

Electrocatalysts	**Nominal composition (wt. %)**	**Composition obtained by EDX (wt. %)**	**Composition obtained by EDX (at. %)**
Pt-Ru/C_{AB}-syn	Pt: 26.35, Ru:13.65, C: 60	Pt: 25.71, Ru: 12.93, O: 1.16, C: 60.2	Pt: 50.75 ,Ru: 49.25
Pt-Ru/C_{AB}-H_2-RT	Pt: 26.35, Ru:13.65, C: 60	Pt: 24.62, Ru: 12.59, O: 3.59, C: 59.20	Pt: 50.33 ,Ru: 49.67
Pt-Ru/C_{AB}-Air-160	Pt: 26.35, Ru:13.65, C: 60	Pt: 25.40, Ru: 12.51, O: 2.80, C: 59.29	Pt: 51.27 ,Ru: 48.73
Pt-Ru/C_{AB}-H_2-160	Pt: 26.35, Ru:13.65, C: 60	Pt: 25.81, Ru: 12.10, O: 1.80, C: 59.39	Pt: 52.50 ,Ru: 47.50
commercial Pt-Ru/C	Pt: 30, Ru:15, C: 55	Pt: 28.40, Ru: 13.28, O: 1.77, C: 56.55	Pt: 52.56 ,Ru: 47.44

The presence of common impurities such as chlorine was also observed. However, traces of chlorine impurity are almost negligible and may be attributed due to the remains of metal precursors used in electrocatalyst synthesis. The presence of oxygen indicates the formation of ruthenium oxides or platinum oxides which have been reported by many other investigators for Pt-Ru/C electrocatalysts (Yang et al., 2003 and Datta et al., 2009). The presence of chlorine common impurity has also been reported by Tayal et al., (2011).

The peak of aluminum at 1.5 eV was also observed during EDX analysis, which originates from the sample holder (Tayal et al., 2011 and Qian et al., 2008).

5.1.2.1.3 Transmission electron microscopy (TEM) analysis

The dispersed state, particle size, and particle size distribution histogram of the electrocatalysts were analyzed by TEM images (Fig 5.18a to Fig 5.18e). It is seen in Fig (5.18a) to Fig (5.18e), most of the nanoparticles are homogeneously distributed on the carbon support surface in all the electrocatalysts. The histogram of the particle size distribution reflects the size distribution in the Pt-Ru/C_{AB} electrocatalysts quantitatively. The heavy dark spots represent Pt-Ru metal alloy nanoparticles, which are well dispersed over the lighter particles carbon support surface (40-60 nm size). The electrocatalysts synthesized by the modified polyol method show well-dispersed metal nanoparticles on the carbon support with varying degrees of dispersion. Fig (5.18a) shows that synthesized fresh Pt-Ru/C_{AB}-syn electrocatalyst nanoparticles are not contacted each other due to the adsorption of glycolate acid on metal nanoparticles and carbon support which preventing the interconnection of nanoparticles.

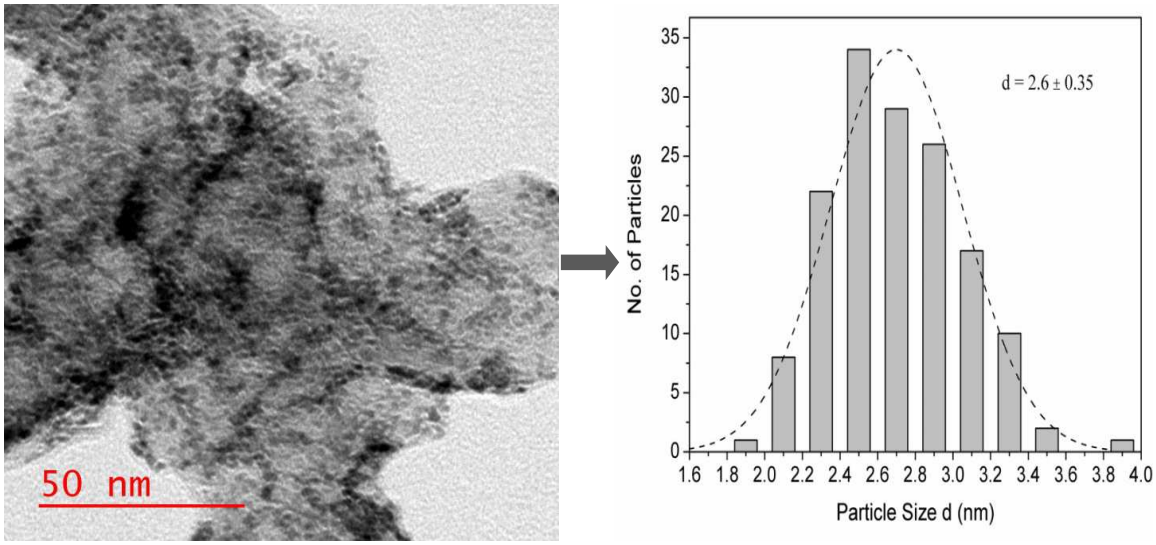

Figure 5.18a TEM image and corresponding size distribution histogram of Pt-Ru/C_{AB}-syn electrocatalyst.

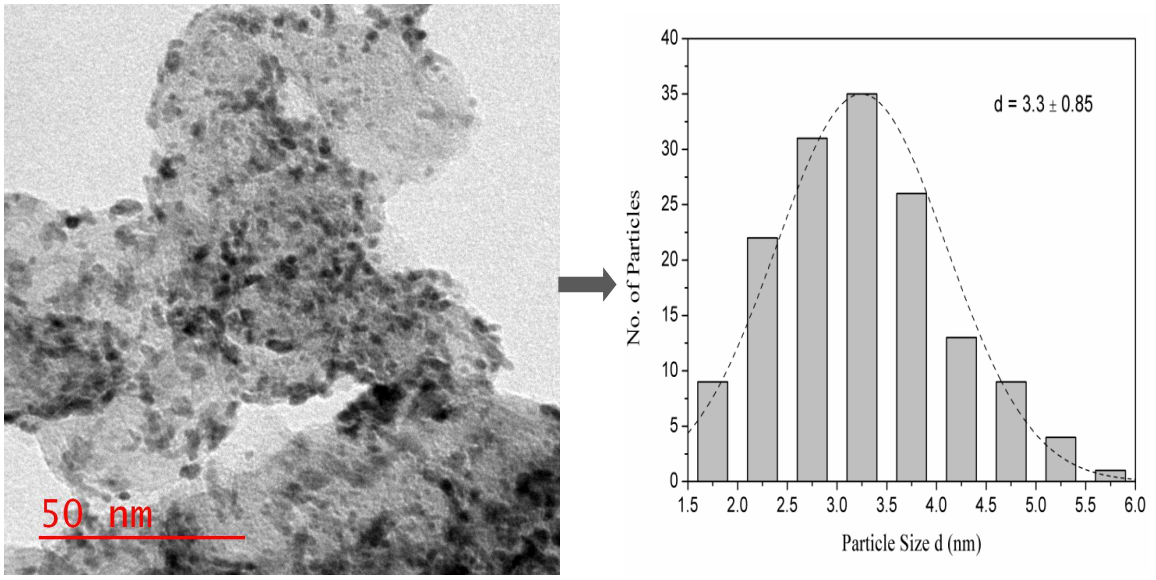

Figure 5.18b TEM image and corresponding size distribution histogram of Pt-Ru/C_{AB}-H_2-RT electrocatalyst.

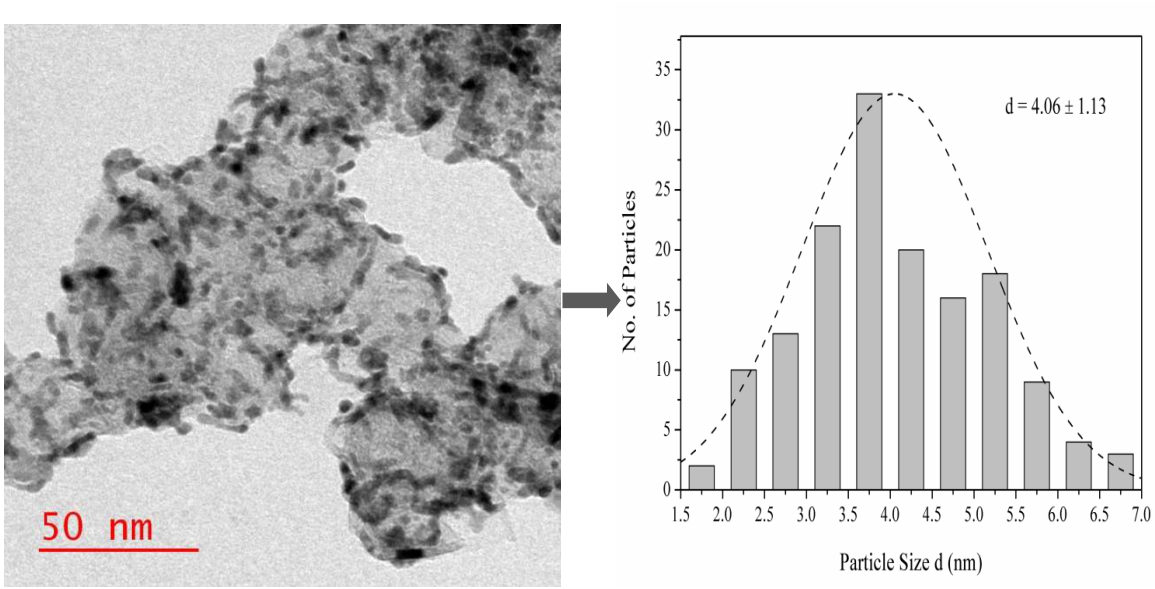

Figure 5.18c TEM image and corresponding size distribution histogram of Pt-Ru/C_{AB}-Air-160 electrocatalyst.

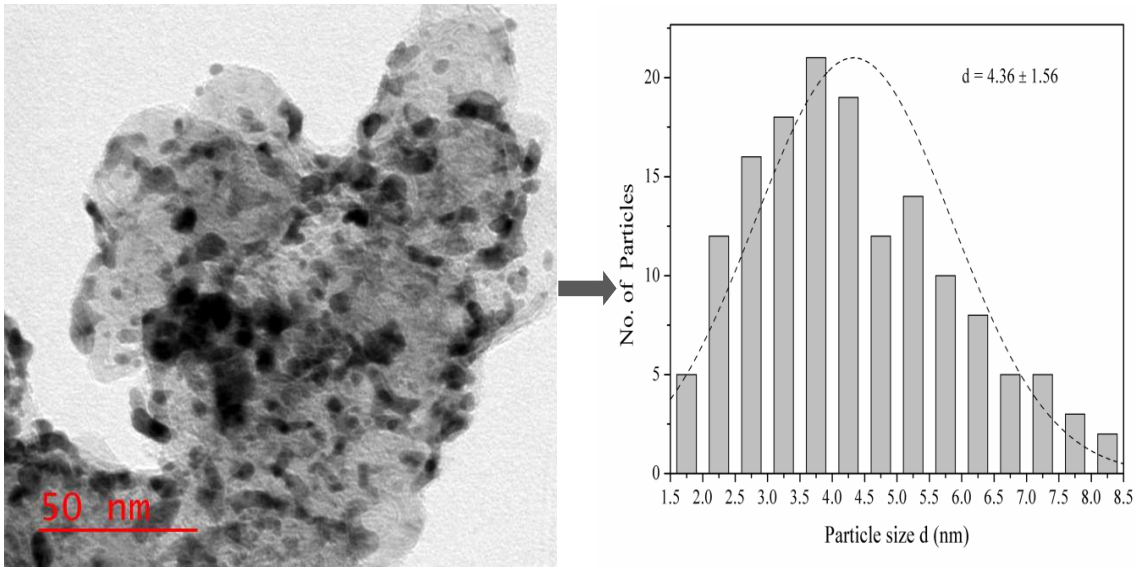

Figure 5.18d TEM image and corresponding size distribution histogram of Ru/C_{AB}-H_2-160 electrocatalyst.

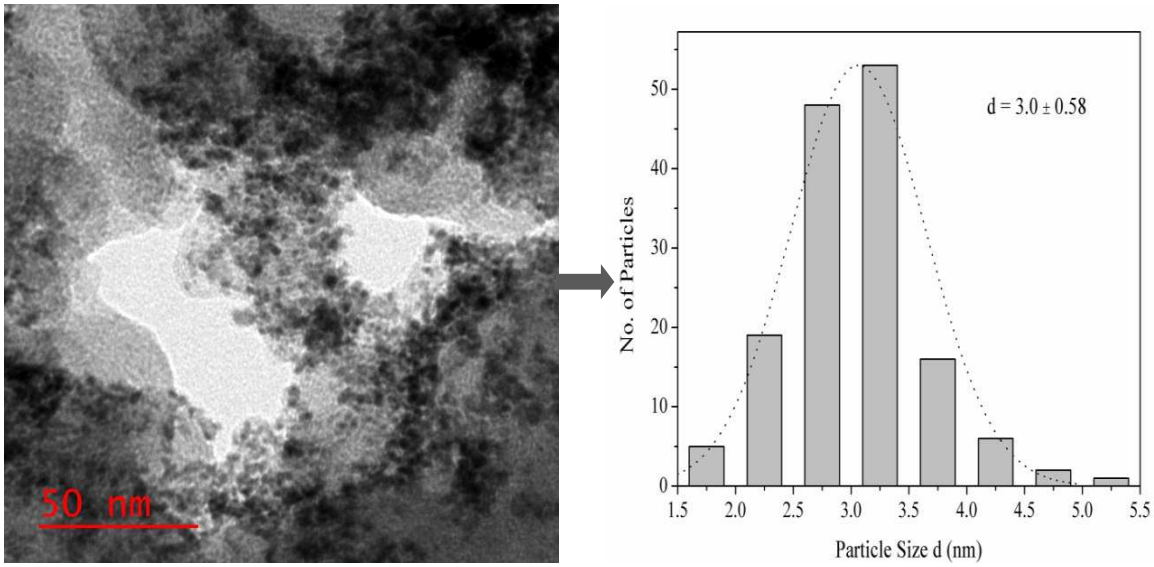

Figure 5.18e TEM image and corresponding size distribution histogram of commercial Pt-Ru/C electrocatalyst.

However, when the Pt-Ru/C_{AB}-syn electrocatalyst undergoes post-treatment in the H_2 gas stream at room temperature (30 °C), the nanoparticles are interconnected together to form bigger particles. This indicates that the post-treatment of electrocatalyst in H_2 gas flow modifies the morphological structures of the Pt-Ru/C_{AB}-H_2-RT electrocatalyst and crystallite size. Post-treatment in an airstream at a temperature of 160 ºC also modified slightly morphological structures and the growth of nanoparticles is also observed in the Pt-Ru/C_{AB}-Air-160 electrocatalyst. When the electrocatalyst was post-treated under H_2 gas flow stream at a temperature of 160 ºC, greatly promoted further agglomeration and interconnection of metal nanoparticles as observed in the Pt-Ru/C_{AB}-H_2-160 electrocatalyst (Fig 5.18d). The particle size for Pt-Ru/C_{AB}-syn electrocatalyst ranges from 1.5 to 4 nm, with an average particle size of 2.6 ± 0.35 nm. The average particle size for Pt-Ru/C_{AB}-H_2-RT synthesized electrocatalyst is 3.3 ± 0.85 nm and the size distribution lies in the range of 1.5 to 6 nm. Similarly, for the commercial Pt-Ru/C electrocatalyst, the average particle size is 3.0 ± 0.58 nm, and size distribution range from

1.5 to 5.5 nm, which is very close to the synthesized post-treated electrocatalyst Pt-Ru/C_{AB}-H_2-RT. However, the average particle size of Pt-Ru/C_{AB}-Air-160 (4.06 ± 1.13 nm) and Pt-Ru/C_{AB}-H_2-160 (4.36 ± 1.56 nm) are larger than Pt-Ru/C_{AB}-H_2-RT and commercial Pt-Ru/C electrocatalysts, respectively. The size distribution ranges are also wider for Pt-Ru/C_{AB}-Air-160 (1.5 nm to 7.0 nm) and Pt-Ru/C_{AB}-H_2-160 (1.5 nm to 8.5 nm) in comparison to Pt-Ru/C_{AB}-H_2-RT and commercial Pt-Ru/C electrocatalysts. The average particle sizes obtained from the TEM (Table 5.10) images agreed with the crystallite size values calculated from XRD measurements.

Table 5.10 The average particle size of electrocatalysts from TEM analysis and comparison with XRD results.

Electrocatalysts	**Average particle size (d_p) by TEM (nm)**	**Average crystallite size (d_c) by XRD (nm)**
Pt-Ru/C_{AB}-syn	2.6 ± 0.35	---
Pt-Ru/C_{AB}-H_2-RT	3.3 ± 0.85	3.2
Pt-Ru/C_{AB}-Air-160	4.06 ± 1.13	3.5
Pt-Ru/C_{AB}-H_2-160	4.36 ± 1.56	3.8
Commercial Pt-Ru/C	3.0 ± 0.58	2.8

5.1.2.2 Electrochemical characterization of anode electrocatalysts

5.1.2.2.1 Cyclic voltammetry (CV) analysis

The ethanol electrooxidation activities of all the synthesized electrocatalysts were evaluated in cyclic voltammetry (CV) tests. Fig (5.19) shows the CV curves of ethanol electrooxidation on the polyol synthesized electrocatalysts in nitrogen saturated atmosphere in the potential range from 0 to 1.0 V using a uniform scan rate of 20 mV/s. It

is seen from Fig (5.19) that all the electrocatalysts resulting in a well-defined peak during the forward and backward scans as well.

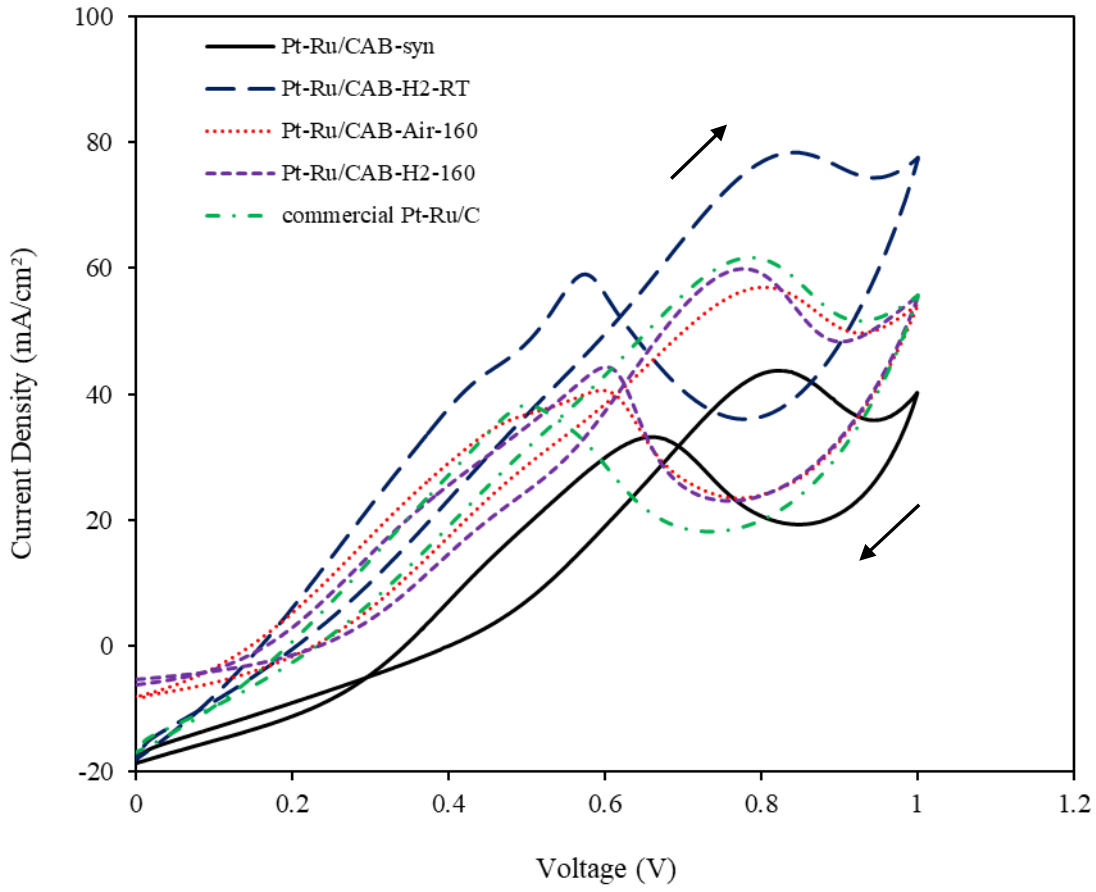

Figure 5.19 Cyclic voltammograms of synthesized Pt-Ru/C_{AB}-syn, Pt-Ru/C_{AB}-H_2-RT, Pt-Ru/C_{AB}-Air-160, Ru/C_{AB}-H_2-160 and commercial Pt-Ru/C electrocatalysts in 0.5 M $HClO_4$ containing 2 M ethanol with a scan rate of 20 mV/s and at a temperature of 40 °C.

The forward and reverse peak potentials and their corresponding current densities of ethanol electrooxidation on the synthesized and commercial electrocatalysts obtained by CV tests are summarized in Table (5.11). The synthesized electrocatalyst Pt-Ru/C_{AB}-H_2-RT gives the highest peak current density of 78.35 mA/cm^2 at a peak potential of 0.845 V. Moreover, during the reverse scan of the same electrocatalyst also produced the highest peak current density of 59.08 mA/cm^2 at a peak potential of 0.576 V.

Table 5.11 CV results of synthesized Pt-Ru/C_{AB}-syn, Pt-Ru/C_{AB}-H_2-RT, Pt-Ru/C_{AB}-Air-160, Ru/C_{AB}-H_2-160, and commercial Pt-Ru/C electrocatalysts at 20 mV/s sweep rate for ethanol electrooxidation.

Anode electrocatalyst	**Forward scan**		**Reverse scan**	
	peak potential (V)	**peak current density (mA/cm^2)**	**peak potential (V)**	**peak current density (mA/cm^2)**
Pt-Ru/C_{AB}-syn	0.825	43.74	0.658	33.20
Pt-Ru/C_{AB}-H_2-RT	0.845	78.35	0.576	59.08
Pt-Ru/C_{AB}-Air-160	0.808	56.95	0.596	40.60
Pt-Ru/C_{AB}-H_2-160	0.779	59.90	0.60	44.31
commercial Pt-Ru/C	0.796	61.60	0.52	37.50

On the other hand, the peak current density of 61.60 mA/cm^2 at a peak potential of 0.796 V was obtained for commercial Pt-Ru/C electrocatalyst. Although, peak potential for commercial Pt-Ru/C during the reverse scan was less positive (0.52 V), the peak current density was the lowest (37.50 mA/cm^2) of all synthesized post-treated electrocatalysts. The anodic peaks during the forward scan for Pt-Ru/C_{AB}-Air-160 and Pt-Ru/C_{AB}-H_2-160 electrocatalysts were appeared at about 0.808 V and 0.779 V, respectively. The forward scan anodic peak current densities were 56.95 mA/cm^2 and 59.90 mA/cm^2 for Ru/C_{AB}-Air-160 and Pt-Ru/C_{AB}-H_2-160 electrocatalysts, respectively. It should be noted that the peak current densities for fresh synthesized Pt-Ru/C_{AB}-syn without post-treatment was the lowest of all the electrocatalysts during the forward scan (43.74 mA/cm^2) and reverse scan (33.20 mA/cm^2), respectively. The electrooxidation peak in the reverse scan is due to further oxidation of carbonaceous intermediates species formed on the electrode surface and near the vicinity of the electrode during the forward scan. As already mentioned, the synthesized Pt-Ru/C_{AB}-H_2-RT shows the highest anodic peak current density of 78.35 mA/cm^2 and possesses the highest electrocatalytic activity among all the electrocatalysts.

The physical characterizations also showed excellent properties for Pt-Ru/C_{AB}-H_2-RT electrocatalyst. The difference in the peak potentials and corresponding current densities is attributed to the surface composition particle size, particle size, defects, and degree of alloying.

5.1.2.2.2 Chronoamperometry (CA) analysis

The stability or rate of surface poisoning of electrocatalysts was evaluated by the chronoamperometry measurement tests at two different cell potentials i.e. 0.45 V and 0.80 V in a solution of 0.5 M $HClO_4$ and 2 M ethanol (Fig 5.20a and Fig 5.20b). The lower reference potential value of 0.45 V was selected, which corresponds to the working anode potential in DEFC operations (Roca-Ayats et al., 2015). The higher reference potential value of 0.8 V was chosen since the average anodic electrooxidation potential for all the studied electrocatalysts in CV analysis (Fig 5.19) was found very close to 0.8 V. It is seen from Fig (5.20a) to Fig (5.20b) that the currents for ethanol electrooxidation on the supported Pt-Ru electrocatalysts dropped sharply at the initial stage, followed by a slow decrease in the current density and then steady-state current was obtained after ~400 s. The sharp decrease in current value is due to diffusion effects or charging current and the gradual decrease to the poisoning of electrocatalysts due to the formation of intermediates during ethanol electrooxidation. It is observed that at a lower potential of 0.45 V (Fig 5.20a), the current density for ethanol electrooxidation on Pt-Ru/C_{AB}-H_2-RT electrocatalyst is significantly higher than that of all the other electrocatalysts. Similarly, at the higher potential of 0.8 V (Fig 5.20b), the electrooxidation current density on Pt-Ru/C_{AB}-H_2-RT synthesized electrocatalyst is always higher in comparison to the synthesized Pt-Ru/C_{AB}-syn, Pt-Ru/C_{AB}-Air-160, Pt-Ru/C_{AB}-H_2-160, and commercial Pt-Ru/C electrocatalysts. The residual current density for ethanol electrooxidation at a

potential of 0.45 V for the synthesized Pt-Ru/C_{AB}-syn, Pt-Ru/C_{AB}-H_2-RT, Pt-Ru/C_{AB}-Air-160, Ru/C_{AB}-H_2-160 and commercial Pt-Ru/C electrocatalysts were 6.30 mA/cm^2, 32.50 mA/cm^2, 9.5 mA/cm^2, 21.47 mA/cm^2 and 22.91 mA/cm^2, respectively.

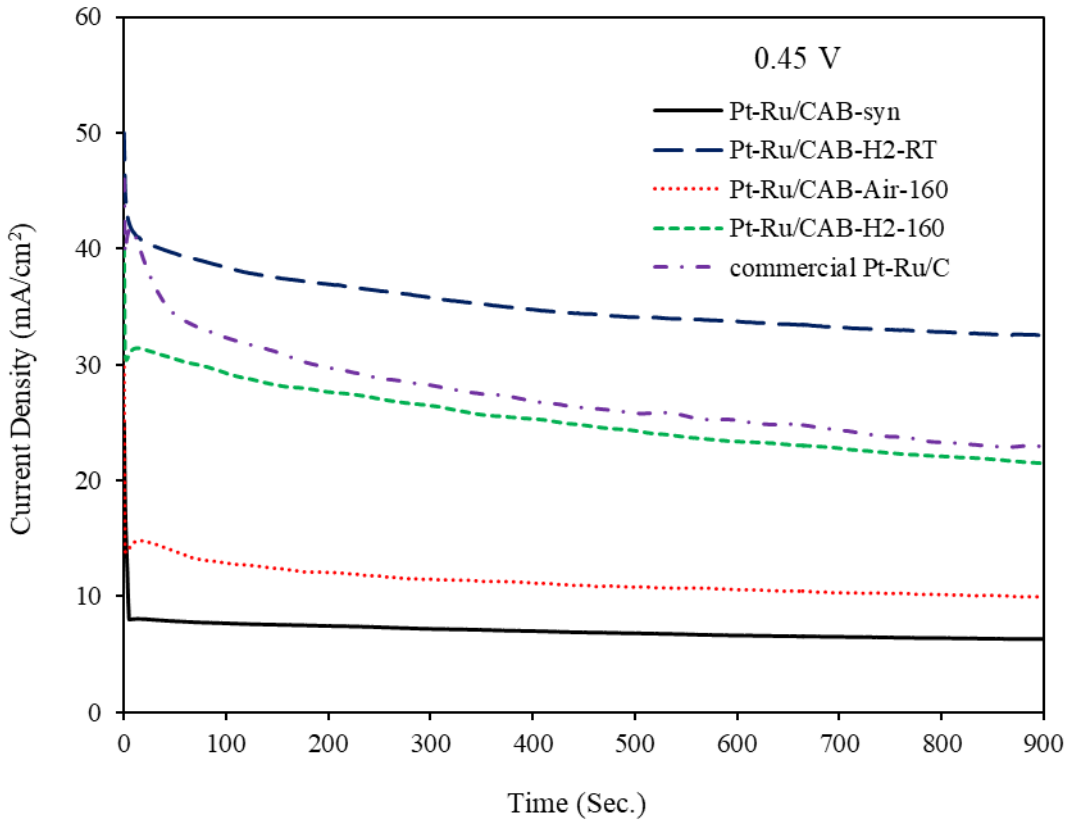

Figure 5.20a CA tests of ethanol oxidation in 0.5 M perchloric acid ($HClO_4$) containing 2 M ethanol solution on synthesized Pt-Ru/C_{AB}-syn, Pt-Ru/C_{AB}-H_2-RT, Pt-Ru/C_{AB}-Air-160, Ru/C_{AB}-H_2-160, and commercial Pt-Ru/C electrocatalysts at 0.45 V vs. Ag/AgCl at room temperature of 40 ^oC.

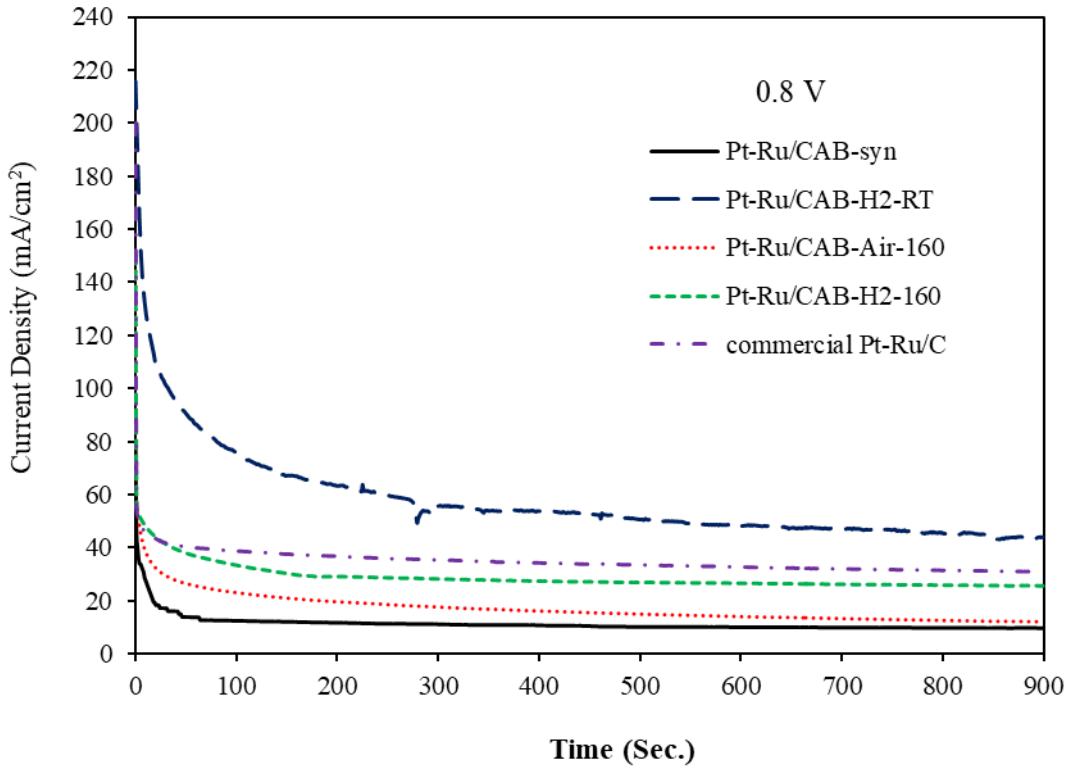

Figure 5.20b CA tests of ethanol oxidation in 0.5 M perchloric acid ($HClO_4$) containing 2 M ethanol solution on synthesized Pt-Ru/C_{AB}-syn, Pt-Ru/C_{AB}-H_2-RT, Pt-Ru/C_{AB}-Air-160, Ru/C_{AB}-H_2-160, and commercial Pt-Ru/C electrocatalysts at 0.8 V vs. Ag/AgCl at room temperature of 40 ^oC.

Furthermore, at the higher potential of 0.8V, the residual current density of 9.74 mA/cm^2, 44 mA/cm^2, 12.1 mA/cm^2, 25.70 mA/cm^2 and 31 mA/cm^2 were obtained for ethanol electrooxidation using the synthesized Pt-Ru/C_{AB}-syn, Pt-Ru/C_{AB}-H_2-RT, Pt-Ru/C_{AB}-Air-160, Ru/C_{AB}-H_2-160, and commercial Pt-Ru/C electrocatalysts, respectively. The synthesized Pt-Ru/C_{AB}-H_2-RT shows the superior performance in terms of current density for the tested period at both electrode potentials of 0.45 V and 0.8 V. This can be attributed to the synergic effect of alloyed Ru and internal microstructure. The chronoamperometry studies also substantiate the results of CV (Fig 5.19) obtained using synthesized and commercial electrocatalysts.

5.1.2.3 DEFC study

5.1.2.3.1 Effect of electrocatalyst type

Fig (5.21) shows the polarization and power density characteristics of DEFC single cell using synthesized Pt-Ru/C_{AB}-syn, Pt-Ru/C_{AB}-H_2-RT, Pt-Ru/C_{AB}-Air-160, Ru/C_{AB}-H_2-160, and commercial Pt-Ru/C electrocatalysts as the anode of 1 mg/cm^2 loading in each electrode. The commercial Pt/C_{HiSPEC} of 1 mg/cm^2 was used as a cathode electrocatalyst.

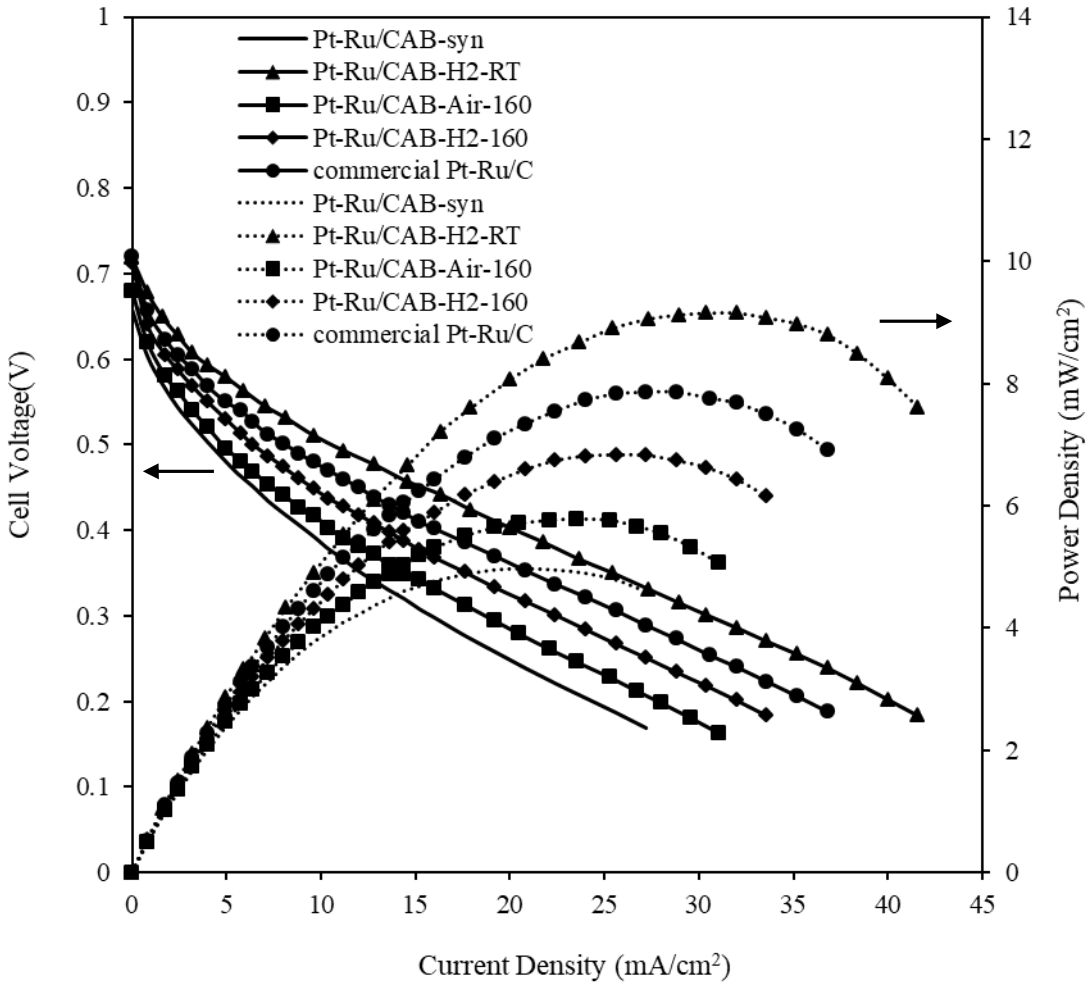

Figure 5.21 Polarization and power density curves for different synthesized electrocatalysts as anode with 1 mg/cm^2 electrocatalyst loading and the cathode (commercial Pt/C_{HiSPEC}) with 1 mg/cm^2 electrocatalyst loading at a cell temperature of 40 °C. Anode: 2 M C_2H_5OH, 1.2 ml/min. Cathode: humidified oxygen, 60 ml/min. Solid electrolyte: Nafion® 117 membranes.

The electrolyte used was a commercial Nafion® 117 membrane. The DEFC temperature was kept similar to that of CV experiments performed i.e 40 °C. The maximum power density, the current density at maximum power density, and OCV of single cell output for various anode electrocatalysts are presented in Table (5.12).

Table 5.12 Summary of performance of synthesized Pt-Ru/C_{AB}-syn, Pt-Ru/C_{AB}-H_2-RT, Pt-Ru/C_{AB}-Air-160, Pt-Ru/C_{AB}-H_2-160 and commercial Pt-Ru/C electrocatalysts in single fuel cell tests for 2 M ethanol at a cell temperature of 40 °C.

Anode electrocatalysts	**Open circuit Voltage (V)**	**Maximum power Density (mW/cm^2)**	**Current density at maximum power density (mA/cm^2)**
Pt-Ru/C_{AB}-syn	0.658	4.97	20.8
Pt-Ru/C_{AB}-H_2-RT	0.718	9.15	32.0
Pt-Ru/C_{AB}-Air-160	0.68	5.79	23.52
Pt- Ru/C_{AB}-H_2-160	0.712	6.84	25.60
commercial Pt-Ru/C	0.720	7.86	28.80

It is seen from Fig (5.21) that the synthesized Pt-Ru/C_{AB}-H_2-RT electrocatalyst resulting in an open circuit voltage (OCV) of 0.718 V, which is near about the same that of the commercial Pt-Ru/C (0.720 V) electrocatalyst. Whereas the OCV for the synthesized Pt-Ru/C_{AB}-Air-160 and Pt-Ru/C_{AB}-H_2-160 electrocatalysts were 0.68 V and 0.712 V, those are lower than the commercial Pt-Ru/C electrocatalyst. The maximum power density of 9.15 mW/cm^2 at a current density of 32 mA/cm^2 and cell voltage of 0.286 V were obtained for synthesized Pt-Ru/C_{AB}-H_2-RT electrocatalyst, which is higher than that of all the other electrocatalysts. The best cell performance of synthesized Pt-Ru/C_{AB}-H_2-RT can be ascribed to the mild condition of the post-treatment so that the phase separation and agglomeration of metal nanoparticles are weak (Lee et al., 2010 and Rizo et al., 2017).

Whereas, the Pt-Ru/C_{AB}-Air-160 electrocatalyst produced the lowest OCV of 0.68 V and a power density of 5.79 mW/cm^2 at a current density of 23.52 mA/cm^2 (Table 5.12). The single cell performance using as-synthesized Pt-Ru/C_{AB}-syn electrocatalyst as an anode was the lowest of all post-treated and commercial electrocatalysts due to lower crystallinity and alloying degree of Ru. The reason for such poor performance of Pt-Ru/C_{AB}-syn has already been discussed in the XRD section. It should be noted that CV and CA tests also showed the highest activity for the synthesized Pt-Ru/C_{AB}-H_2-RT electrocatalyst as observed in the single cell study.

Due to the highest electrocatalytic activity of synthesized electrocatalyst Pt-Ru/C_{AB}-H_2-RT, it was used as anode electrocatalyst for optimization of operating parameters like ethanol concentration and cell temperature which are presented in the sections below.

5.1.2.3.2 Effect of ethanol concentration

Fig (5.22) shows the DEFC performance curves for different ethanol concentrations using the synthesized Pt-Ru/C_{AB}-H_2-RT as anode and Pt/C_{HiSPEC} as cathode electrocatalyst at a temperature of 40 ºC. The cathode oxidant used was humidified oxygen. The electrocatalyst loading at anode and cathode were 1 mg/cm^2. It is seen from Fig (5.22) that with the rise in ethanol concentration from 0.5 M to 2 M, the polarization and power density curves shifted upward, while the concentration increased further to 3 M, the curves shifted downwards.

Fig (5.22) shows that the OCV of 0.718 V and the maximum power density of 9.15 mW/cm^2 at a current density of 32 mA/cm^2 were obtained for ethanol concentration of 2 M. Whereas, the ethanol concentrations of 1 M and 3 M produced a maximum power density of 6.77 mW/cm^2 at a current density of 24 mA/cm^2 and a maximum power

density of 7.81 mW/cm^2 at a current density of 27.2 mA/cm^2, respectively. The OCV values of 0.715 V and 0.684 V were obtained for 1 M and 3 M of ethanol respectively. The ethanol concentration of 0.5 M produced an OCV of 0.72 V and a very low power density of 5.70 mW/cm^2 at a current density of 20.8 mA/cm^2.

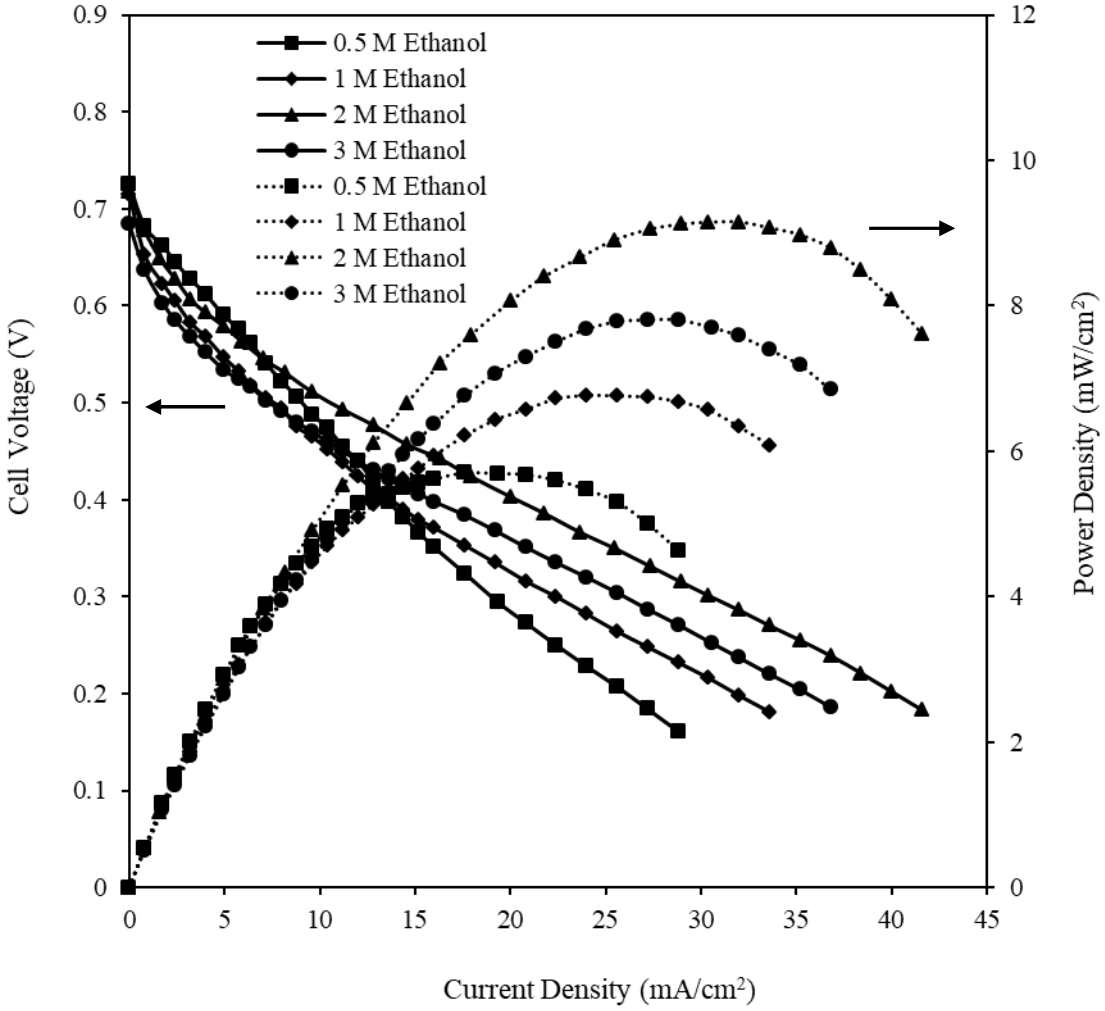

Figure 5.22 Single cell performance characteristics for anode electrocatalyst Pt-Ru/C_{AB}-H_2-RT using varying ethanol concentration as anode feed at a cell temperature of 40 °C. Cathode feed: pure humidified oxygen; $P_{cathode}$ = 1 bar (absolute); Dotted line-power density curves; Solid line- polarization curves.

Initially, with an increase in fuel ethanol concentration, the current density increases as the reaction kinetics improves at a higher fuel concentration. At the higher ethanol

concentration of 3 M the cell performance decreases. This may be due to the rise in fuel at very high concentrations and, at the same time, the supply of H_2O molecules at the electrocatalyst site decreases due to the coverage of the electrocatalyst active sites.

5.1.2.3.3 Effect of cell temperature

Fig (5.23) illustrates the effect of cell performance at various temperatures ranging from 40 °C to 80 °C for the synthesized best anode electrocatalyst Pt–Ru/C_{AB}-H_2-RT. The positive effect of temperature can be observed in terms of high current density and power density. The maximum power density of 9.15 mW/cm^2 at a cell voltage of 0.286 V and a current density of 32 mA/cm^2 were achieved at the cell temperature of 40 °C. The DEFC power density reached at 16.23 mW/cm^2 at a cell voltage of 0.317 V and a current density of 51.2 mA/cm^2 when cell temperature was increased to 80 ºC. There was an almost 77.4 % increase in power density for the rise of cell temperature of 40 °C. The effect of temperatures on a single DEFC's open circuit voltage and cell performance is summarized in Table (5.13). The enhanced performance accompanied by an increment in cell operating temperatures can be attributed to the combined effect of a reduction of activation overpotential and ohmic polarization. The electrocatalytic activity of synthesized Pt-Ru/C_{AB}-H_2-RT for ethanol electrooxidation increases with the increase in cell temperature, thereby increasing current density (Song et al., 2005, Alzate et al., 2011 and Pramanik et al., 2008). Furthermore, high cell temperature enhances the proton conductivity of the Nafion® membrane and Nafion® ionomer in the electrocatalyst layers, therefore ohmic polarization gets reduced (Alzate et al., 2011). As already mentioned, a similar trend for effect of cell temperature is also observed commercial Pt-Ru/C as anode electrocatalyst. The detailed single cell study is presented in Appendix D (Fig D.1, Page no. 281).

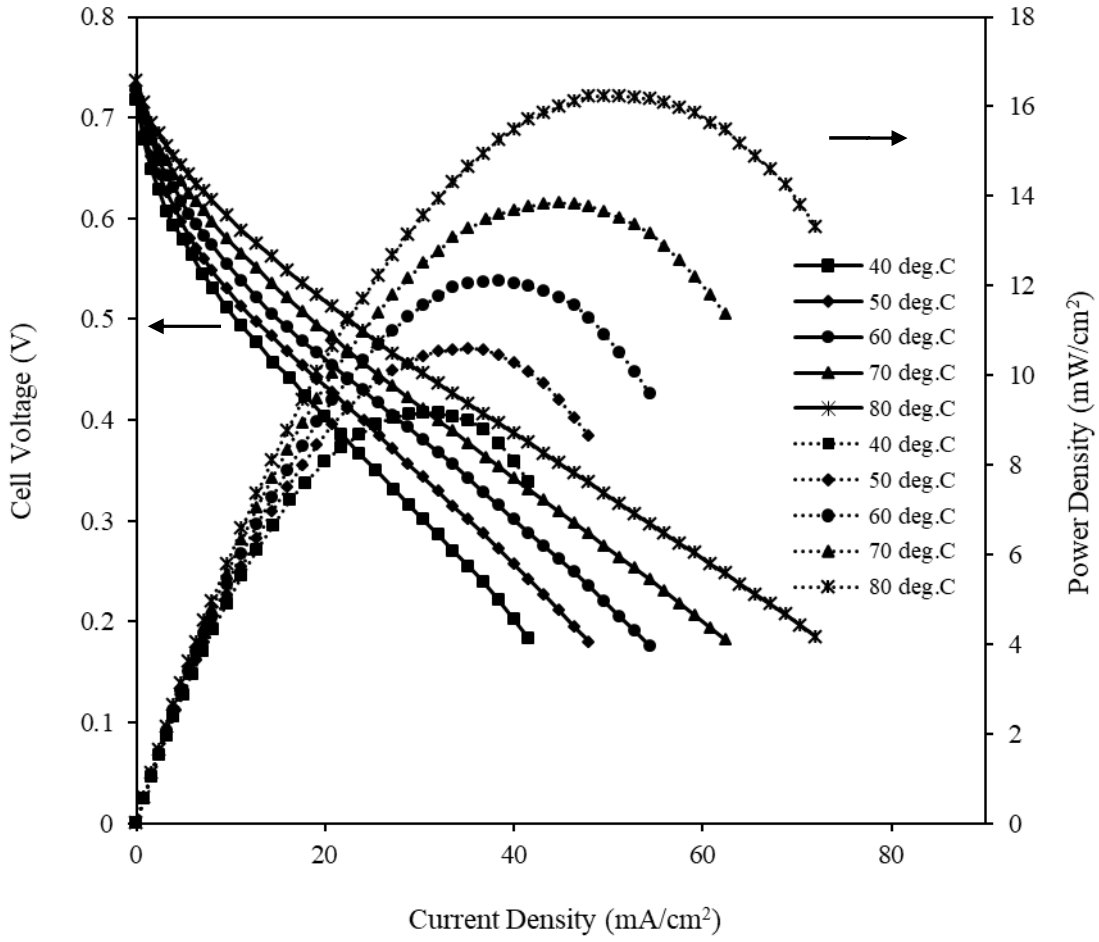

Figure 5.23 Performance curves of the synthesized Pt–Ru/C_{AB}-H_2-RT electrocatalyst with 1 mg/cm^2 electrocatalyst loading in anode side and the commercial Pt/C_{HiSPEC} electrocatalyst as a cathode with 1 mg/cm^2 electrocatalyst loading at various temperatures. Anode: 2 M ethanol, 1.2 ml/min flow rate. Cathode: humidified oxygen, 60 ml/min. Solid electrolyte: Nafion® 117 membranes.

Table 5.13 Summary of performance of synthesized Pt-Ru/C_{AB}-H_2-RT electrocatalysts in single fuel cell tests for 2 M ethanol at different operating cell temperature.

Electrocatalyst	Temperature (°C)	Open circuit Voltage (V)	Maximum power density (mW/cm^2)	Current density at maximum power density (mA/cm^2)
Pt-Ru/C_{AB}-H_2-RT	40	0.718	9.15	32.0
	50	0.723	10.60	35.2
	60	0.728	12.10	38.4
	70	0.732	13.84	44.8
	80	0.737	16.23	51.2

5.2 Performance evaluation of Pt-based bi-metallic and tri-metallic electrocatalysts supported on f-MWCNT: Part II

The bi-metallic and tri-metallic electrocatalysts are synthesized by the method described in chapter 3 (Experimental, Page no. 86-87) were characterized and their tested in half cell, and single DEFC. The results are reported and discussed below.

5.2.1 Physical characterization of MWCNT support material

5.2.1.1 X-ray diffraction (XRD) analysis

The X-ray diffraction **(**XRD) patterns of pristine multi-walled carbon nanotubes (p-MWCNT) and functionalized multi-walled carbon nanotubes (f-MWCNT) support materials are presented in Fig (5.24).

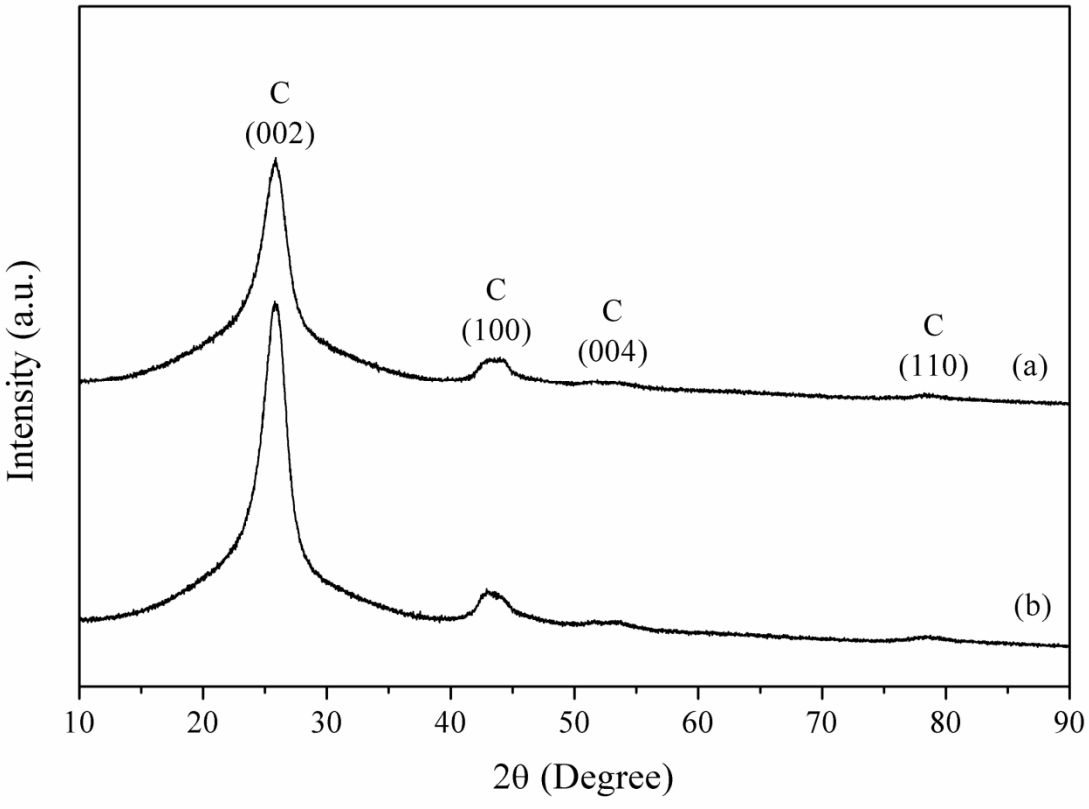

Figure 5.24 XRD patterns of (a) p-MWCNT and (b) f-MWCNT support material.

The diffraction peaks at 25.86°, 43.4°, 53.1° and 78.77° observed in the diffraction patterns of MWCNTs are ascribed to the ordered hexagonal graphite structures (002), (100), (004) and (110), respectively (Li et al., 2003). The peak intensity of f-MWCNT was sharper and intense due to the functionalization. It is seen from Fig (5.24) that the crystallinity of f-MWCNT improved due to the removal of amorphous phase/impurities from p-MWCNT. However, the characteristics of diffraction peaks of hexagonal graphite carbon remained in the same position (Fig 5.24).

5.2.1.2 Fourier transform infrared spectroscopy (FTIR) analysis

The FTIR was performed to observe the surface groups after the functionalization of the p-MWCNT support material as illustrated in Fig (5.25). More pronounced relative peak intensity at 3433 cm^{-1} in f-MWCNT than that of p-MWCNT suggests that more -OH groups are attached to the MWCNTs after acid treatment. The observed peaks at 2923 cm^{-1} and 2851 cm^{-1} in both samples are assigned to the C−H stretching vibration of asymmetric/symmetric methylene located at the defects sites of p-MWCNT side walls surface (Montanheiro et al., 2015). However, the relative intensity of these peaks for the f-MWCNT sample significantly decreased, which suggests that alkyl chains were cleaved from the p-MWCNT surface. The peak that appears at 1570 cm^{-1} is ascribed to the C=C stretching vibrations of MWCNT backbones/side walls, confirming the integrity of the hexagonal structure of p-MWCNT (Li et al., 2011 and Theodore et al., 2011). The same peak is also observed for f-MWCNT with a higher intensity (Fig 5.25). For f-MWCNT (Fig 5.25), the characteristic absorption peaks at 1720 cm^{-1} and 1638 cm^{-1} are indexed as C=O stretching vibrations of the carboxylic groups (–COOH) and of ketone/quinone, respectively (Chen et al., 2006, Xu et al., 2010 and Stobinski et al., 2010).

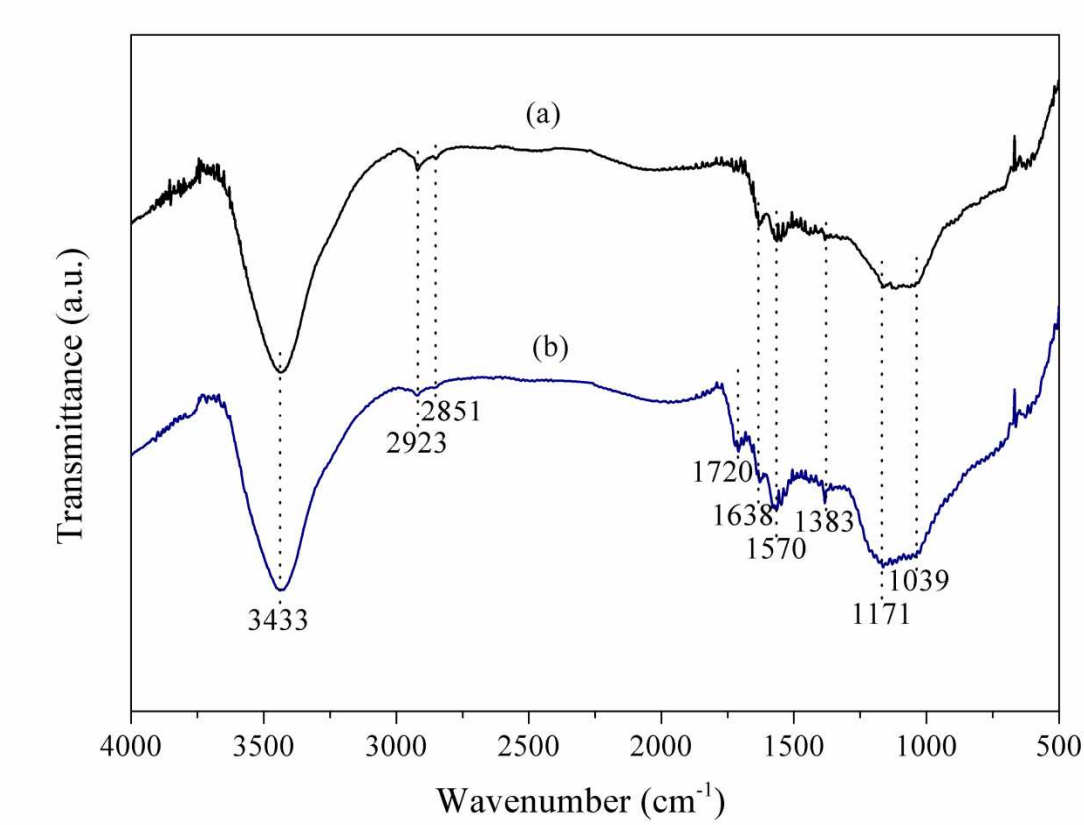

Figure 5.25 FTIR spectra of (a) p-MWCNT and (b) f-MWCNT support material.

The absorption peak at 1638 cm^{-1} for p-MWCNT is also observed with weak strength, which may result from the oxidation of some p-MWCNT defects oxygen presence in the air (Chen et al., 2006). After functionalization, the relative increase in peak intensity and partial separation of bands in the 1250–950 cm^{-1} wave region points are observed (Fig 5.25), which is due to an increase in amounts of hydrated surface oxides combination of phenols, hydroquinones, and aromatic carboxylic acids. The characteristic absorption peaks at 1171 cm^{-1} and 1039 cm^{-1} are indexed as C–O stretching vibrations of the carboxylic groups (–COOH) and phenols/hydroquinones, respectively. While, the absorption peak at 1383 cm^{-1} is associated with O–H bending in carboxylic groups (–COOH) (Li et al., 2011 and Her et al., 2013). It is clear from Fig (5.25) and Table (5.14) that sufficient oxygenated groups have been generated on the surface of p-MWCNT after

functionalization in a mixture of HNO_3/H_2SO_4 solution. Meanwhile, ultrasonic treatment in nitric acid also helps to purify p-MWCNT from foreign objects embedded on their surface and the individual MWCNTs from the entangled bundle form. Furthermore, it can cause opening the port of MWCNTs and shortening of their lengths, resulting in an increase of defects and surface area for better dispersion of precursor metal ions.

Table 5.14 Comparison and shifting of bands data of p-MWCNT and f-MWCNT support using FTIR analysis.

Stretching or bending functional groups	**Wavenumber (cm^{-1})**	
	p-MWCNT	**f-MWCNT**
C-O stretching in phenols/hydroquinones	1039	1039
C–O stretching in carboxylic groups (–COOH)	1171	1171
O–H bending deformation in carboxylic acid	1383	1383
C=C stretching vibrations of MWCNT backbones	1570	1570
C=O stretching vibrations ketone/quinone	1638	1638
C=O stretching in carboxylic groups (–COOH)	…	1720
C-H stretching asymmetric	2851	2851
C-H stretching symmetric	2923	2923
O-H moieties and/or O-H in carboxyl groups and sorbed water	3433	3433

5.2.2 Physicochemical characterization of electrocatalysts

5.2.2.1 X-ray diffraction (XRD) analysis

The synthesized Pt-Ru supported on the functionalized MWCNT (f-MWCNT) resulting in smaller crystallite size and higher degree of Ru alloying. The XRD results of Pt-Ru (1:1)/p-MWCNT and Pt-Ru (1:1)/f-MWCNT are reported in Appendix E (Fig E.1, Table E.1, Page no. 282). In view of this, all the electrocatalysts discussed in this section were synthesized using the functionalized MWCNT (f-MWCNT) support.

The crystalline features of synthesized Pt-Ru (1:1)/f-MWCNT, Pt-Re (1:1)/f-MWCNT, Pt-Ru-Re (1:1:1)/f-MWCNT, Pt-Ru-Re (1:1:0.5)/f-MWCNT, and Pt-Ru-Re (1:1:0.25)/f-MWCNT electrocatalysts were analyzed by XRD measurements as shown in Fig (5.26a-e). The well-defined intense diffraction peak at about 25.86º can be ascribed to the (002) plane of the hexagonal graphitic structure of MWCNT carbon support in all electrocatalysts. Besides, the diffraction peaks at around 2θ of 40º, 46º, 68º, and 82º are assigned to (111), (200), (220) and (311) crystalline planes of the face-centered cubic (fcc) of Pt alloys, respectively. The diffraction peak of MWCNTs (100) is merged with the Pt (200) peak. Comparing with XRD peaks of pure Pt (JCPDS card 04-0802), it is seen that the diffraction peaks of all the bi-metallic and tri-metallic electrocatalysts slightly shifted to higher 2θ values at the plane (111), (200), (220) and (311) (Fig 5.26a-e). However, the shifting of the peak for Pt-Re (1:1)/f-MWCNT electrocatalyst is slightly higher than the pure Pt and lower than the rest of the electrocatalysts. For a better understanding of the diffraction characteristics and shifting of peaks at planes Pt (111) and Pt (220), the XRD diffraction characteristics have been enlarged and presented in Appendix F (Fig F.1 and Fig F.2, Page no. 283, 284). The shifting of peak position (2θ)

values for all planes Pt (111), Pt (200), Pt (220), and Pt (311) of the synthesized electrocatalysts are summarized in Appendix F (Table F.1, Page no. 284).

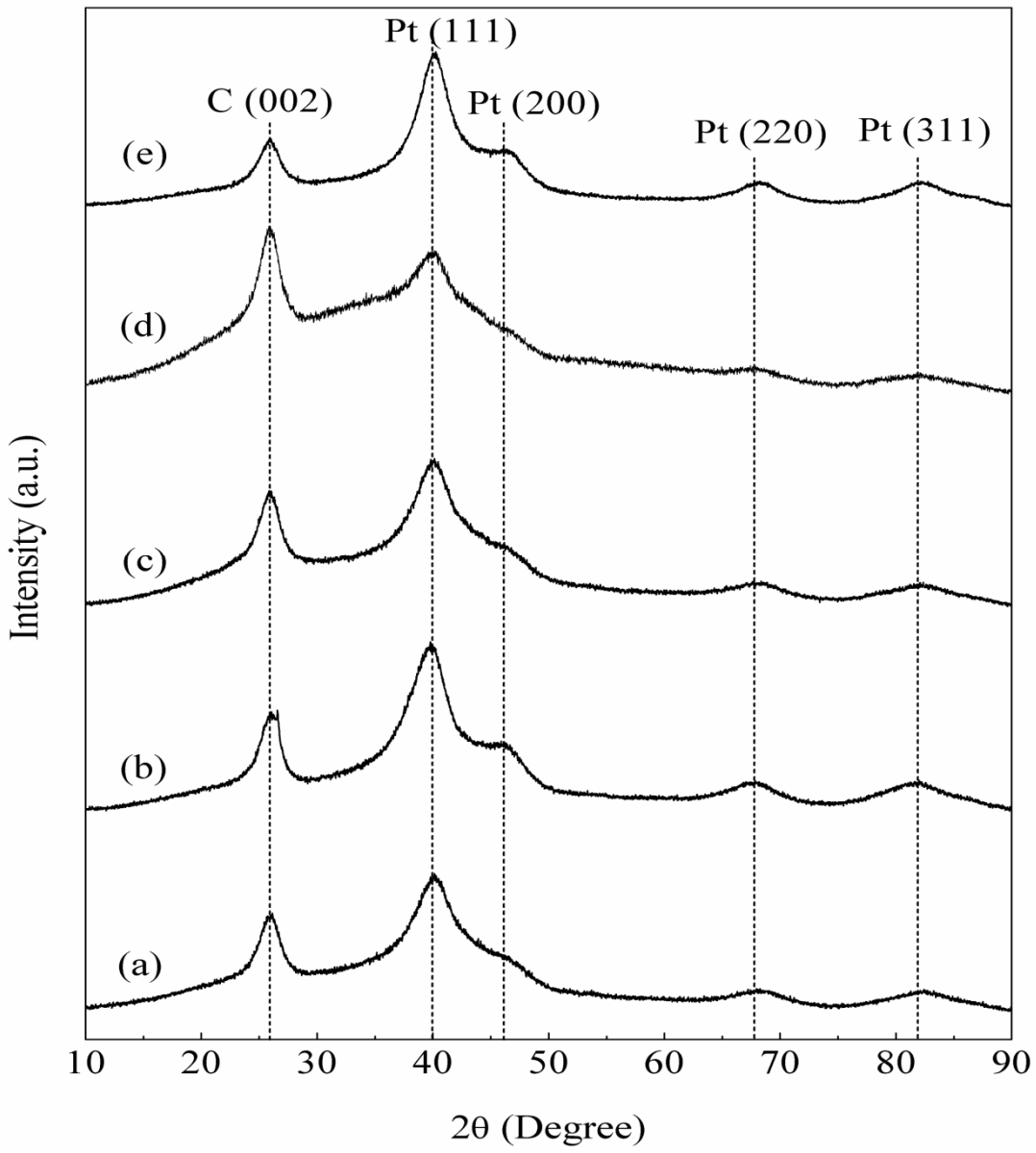

Figure 5.26 XRD patterns of (a) Pt-Ru (1:1)/f-MWCNT, (b) Pt-Re (1:1)/f-MWCNT, (c) Pt-Ru-Re (1:1:1)/f-MWCNT, (d) Pt-Ru-Re (1:1:0.5)/f-MWCNT and (e) Pt-Ru-Re (1:1:0.25)/f-MWCNT electrocatalysts.

This suggests that the atoms of Ru and Re were incorporated into the fcc structure of Pt to form a metal alloy. For Pt-Re (1:1)/f-MWCNT electrocatalyst, no peaks corresponding to Re were found due to possible overlap with Pt peaks. However, the introduction of rhenium does not affect much the Pt crystal structure and it may be due to some extent of alloy formation. Further, it could be better interpreted on the basis of their different atomic sizes to Pt metal (r_{Pt} = 0.139 nm, r_{Ru} = 0.134 nm and r_{Re} = 0.137 nm). The diffraction peaks related to the presence of either pure Ru, Re metal or their oxides/hydroxides species are not detected, suggesting that Ru or Re may be incorporated into the fcc structure of Pt lattice to form Pt-Ru alloys, or partially exists as oxides/hydroxides in amorphous form but not discerned by XRD measurements (Chen et al., 2010, Zhao et al., 2010 and Yang et al., 2012). Furthermore, the broadened diffraction peaks of the metals in XRD spectra indicate that the electrocatalysts have small particle/grain sizes (Zhao et al., 2010). The diffraction peaks for Pt-Ru-Re (1:1:0.5)/f-MWCNT (Fig 5.26d) electrocatalyst are a little broader than the other XRD spectra. The average crystallite size calculated using Equation (3.4) at the peak position of Pt (220) is 2.70 nm, 3.05 nm, 2.30 nm, 2.11 nm, and 2.83 nm for Pt-Ru (1:1)/f-MWCNT, Pt-Re (1:1)/f-MWCNT, Pt-Ru-Re (1:1:1)/f-MWCNT, Pt-Ru-Re (1:1:0.5)/f-MWCNT, and Pt-Ru-Re (1:1:0.25)/f-MWCNT electrocatalysts, respectively. The lowest crystallite size of 2.11 nm was found for the Pt-Ru-Re (1:1:0.5)/f-MWCNT (Fig 5.26d). The lattice parameters related to Pt (220) are calculated using Equation (3.5) and Equation (3.6) and presented in Table (5.15). The lattice parameters obtained for Pt-Ru (1:1)/f-MWCNT (0.3881 nm) and Pt-Re (1:1)/f-MWCNT (0.3913) are smaller than pure Pt (0.3924 nm) metal (Xu et al., 2010). The lattice parameters of tri-metallic Pt-Ru-Re (1:1:1)/f-MWCNT, Pt-Ru-Re (1:1:0.5)/f-MWCNT, and Pt-Ru-Re (1:1:0.25)/f-MWCNT

electrocatalysts are 0.38892 nm, 0.38862 nm and 0.38842 nm, respectively. This clearly shows the incorporation of Re atoms to Pt-Ru (1:1)/f-MWCNT electrocatalyst.

Table 5.15 The Pt (220) peak, lattice parameters, and crystallographic properties of the electrocatalysts from XRD analysis.

Electrocatalyst	**Pt (220) Peak position, 2θ (°)**	**d-spacing (nm)**	**Lattice parameter, a (nm)**	**Average crystallite size, d_c (nm)**
Pt-Ru (1:1)/f-MWCNT	68.30	0.1372	0.3881	2.70
Pt-Re (1:1)/f-MWCNT	67.63	0.1384	0.3913	3.05
Pt-Ru-Re (1:1:1)/f-MWCNT	68.14	0.1375	0.38892	2.40
Pt-Ru-Re (1:1:0.5)/f-MWCNT	68.20	0.1374	0.38862	2.11
Pt-Ru-Re (1:1:0.25)/f-MWCNT	68.24	0.13733	0.38842	2.87
Pt metal (Xu et al., 2010)	---	---	0.3924	---
Ru metal (Xu et al., 2010)	---	---	0.2706	---

5.2.2.2 Transmission electron microscopy (TEM) analysis

The morphology of the synthesized electrocatalysts was analyzed using TEM micrographs and the results are illustrated in Fig (5.27a) to Fig (5.27e). The micrographs reveal that almost spherical shape metal nanoparticles (NPs) are well deposited onto the external surface of f-MWCNTs support. The TEM micrographs neither depict remarkable differences in shape nor particle size for the whole series. There is almost no agglomeration of metal nanoparticles in the electrocatalysts, and the metal nanoparticles were found to be homogeneously distributed on the wall of f-MWCNT. The average particle size and the distribution histograms were evaluated statistically by measuring the

sizes of 150 randomly selected NPs on the surface of f-MWCNT from TEM micrographs and presented in Fig (5.27a) to Fig (5.27e).

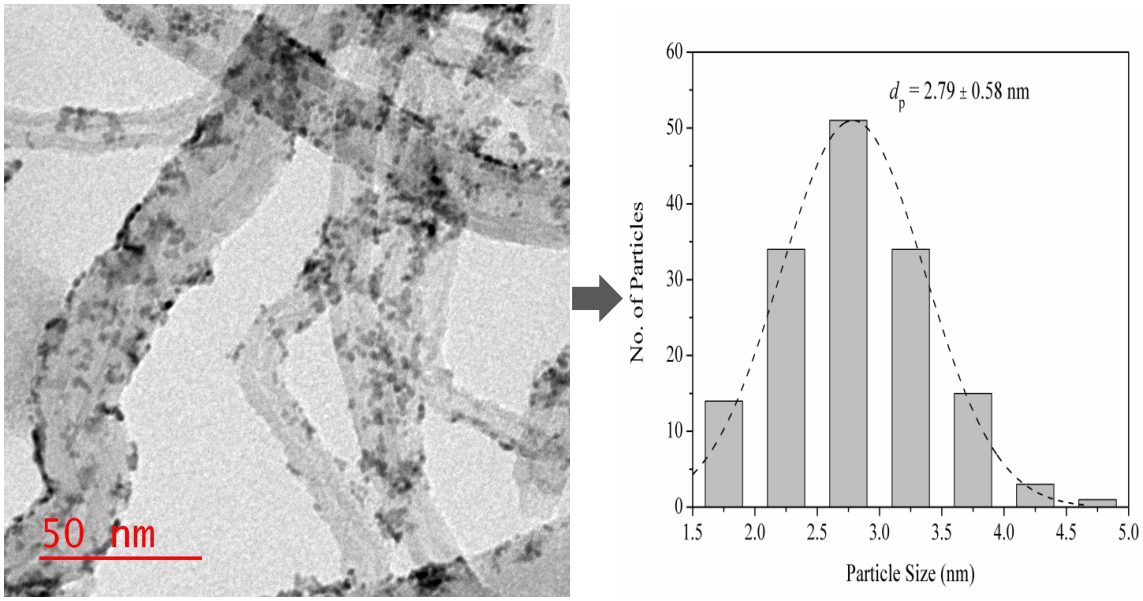

Figure 5.27a TEM micrograph and the corresponding particle size distribution histogram of Pt-Ru (1:1)/f-MWCNT electrocatalyst.

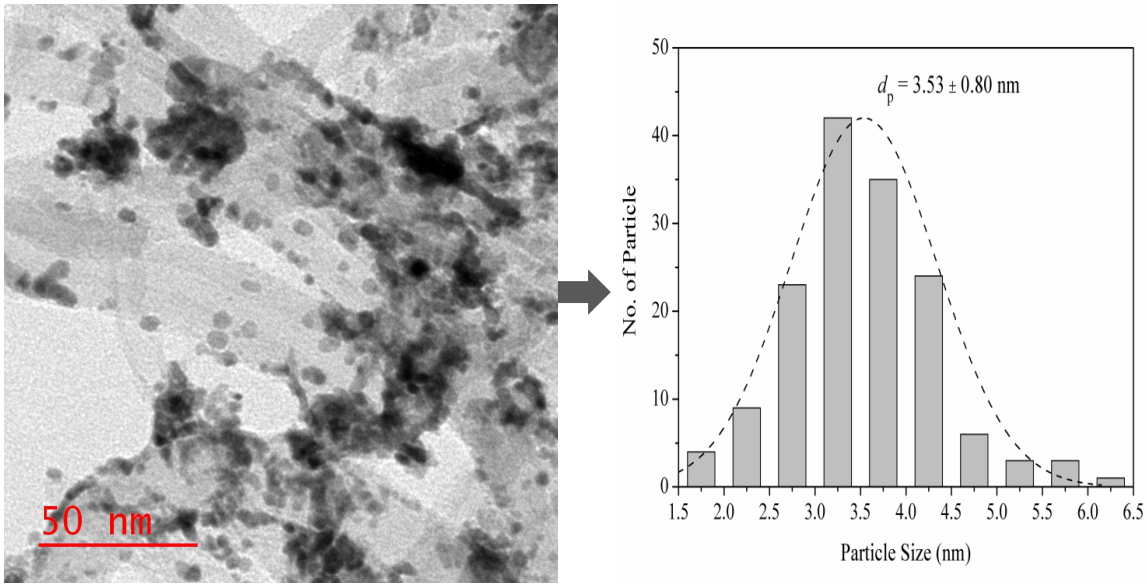

Figure 5.27b TEM micrograph and the corresponding particle size distribution histogram of Pt-Re (1:1)/f-MWCNT electrocatalyst.

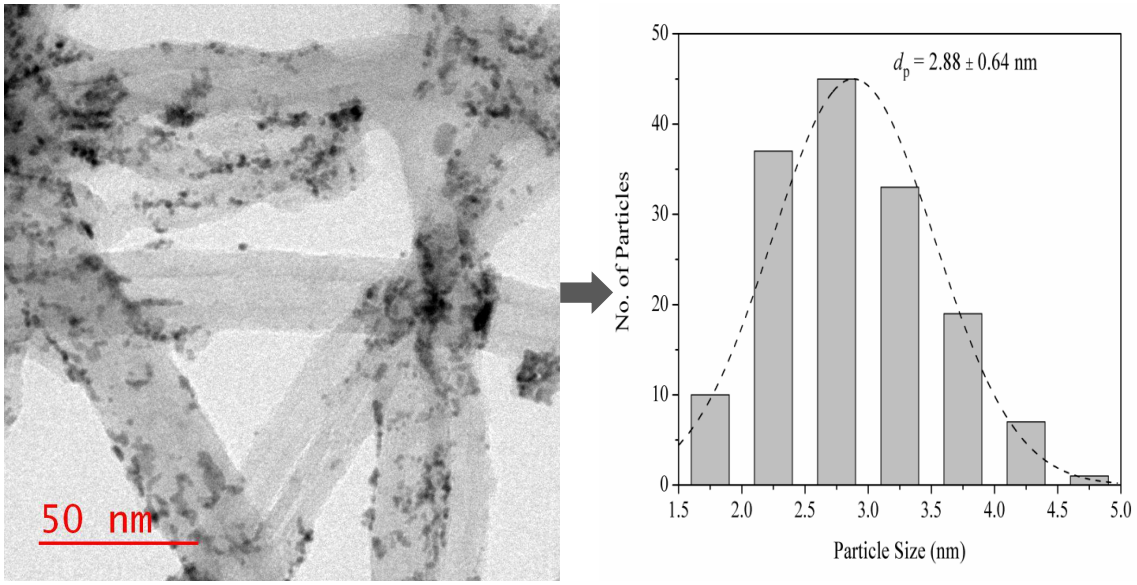

Figure 5.27c TEM micrograph and the corresponding particle size distribution histogram of Pt-Ru-Re (1:1:1)/f-MWCNT electrocatalyst.

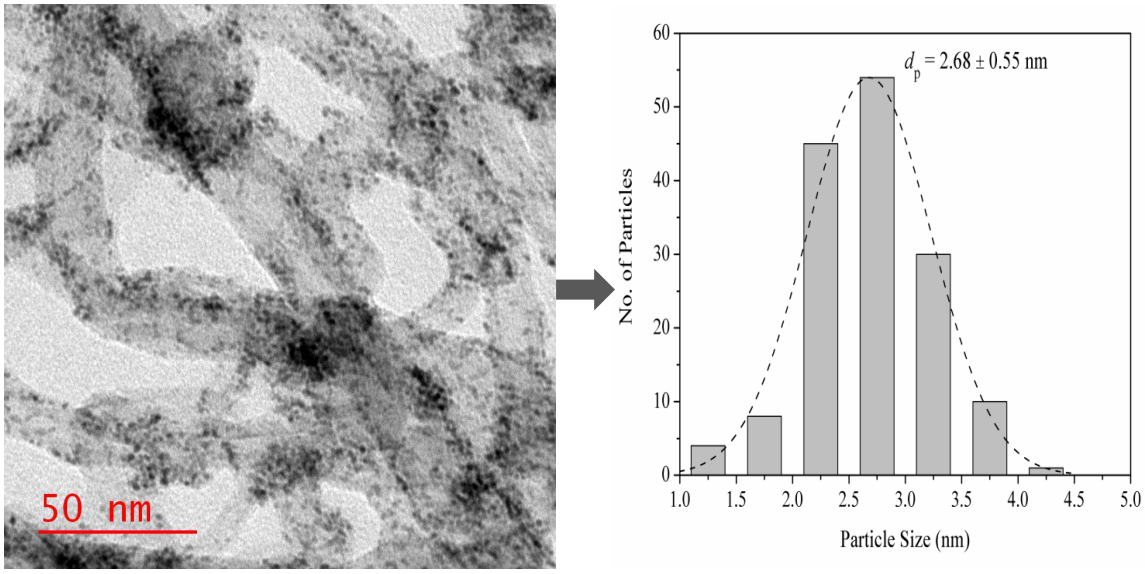

Figure 5.27d TEM micrograph and the corresponding particle size distribution histogram of Pt-Ru-Re (1:1:0.5)/f-MWCNT electrocatalyst.

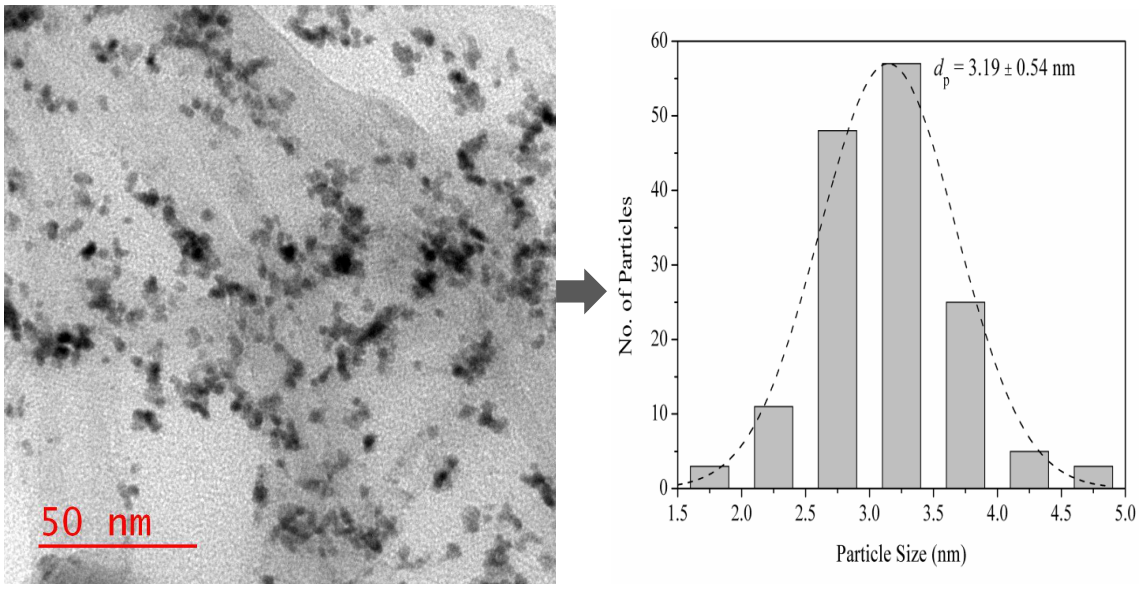

Figure 5.27e TEM micrograph and the corresponding particle size distribution histogram of Pt-Ru-Re (1:1:0.25/f-MWCNT) electrocatalyst.

The average particle size and size distributions of the electrocatalysts are presented in Table (5.16). The average particle sizes of the synthesized electrocatalysts were 2.79 ± 0.58 nm, 3.53 ± 0.80 nm, 2.88 ± 0.64 nm, 2.68 ± 0.55 nm and 3.19 ± 0.54 nm for Pt-Ru (1:1)/f-MWCNT, Pt-Re (1:1)/f-MWCNT, Pt-Ru-Re (1:1:1)/f-MWCNT, Pt-Ru-Re (1:1:0.5)/f-MWCNT and Pt-Ru-Re (1:1:0.25)/f-MWCNT, respectively. The average particle size for Pt-Re (1:1)/f-MWCNT electrocatalyst is larger than the others, which might be due to some agglomeration of the Pt-Re nanoparticles on the surface of f-MWCNTs. The variations in average particle sizes of the electrocatalysts nanoparticles are quite similar in both TEM and XRD, confirming good particle dispersion on the f-MWCNT surface without the formation of large aggregates (Table 5.16). Similar to the XRD results, the lowest average particle size of 2.68 ± 0.55 nm was also obtained in TEM analysis for Pt-Ru-Re (1:1:0.5)/f-MWCNT. Thus, it is expected that the Pt-Ru-Re (1:1:0.5)/f-MWCNT could perform better in half cell and single DEFC for the electrooxidation of ethanol.

Table 5.16 The average particle size of electrocatalysts evaluated from TEM analysis and comparison with XRD results.

Electrocatalysts	**Average particle size (d_p) by TEM (nm)**	**Average crystallite size (d_c) by XRD (nm)**
Pt-Ru (1:1)/f-MWCNT	2.79 ± 0.58	2.70
Pt-Re (1:1)/f-MWCNT	3.53 ± 0.80	3.05
Pt-Ru-Re (1:1:1)/f-MWCNT	2.88 ± 0.64	2.40
Pt-Ru-Re(1:1:0.5)/f-MWCNT	2.68 ± 0.55	2.11
Pt-Ru-Re(1:1:0.25)/f-MWCNT	3.19 ± 0.54	2.87

The electronic diffraction patterns of electrocatalysts reveal the polycrystalline phase of nanoparticles, which is also confirmed by annular patterns in selected area electron diffraction (SAED) patterns presented in Appendix G (Fig (G.1a) to Fig (G.1e), Page no. 285-287).

5.2.2.3 FESEM-EDX analysis

The surface morphology of the synthesized bi-metallic and tri-metallic electrocatalysts were analyzed using field-emission scanning electron microscopy (FESEM) and results are depicted in Fig (5.28a) to Fig (5.28e). The micrographs show spherical shape electrocatalysts nanoparticles with varying particle sizes of 1-6.5 nm. It is clearly observed that metal nanoparticles are well dispersed and anchored onto the external surface of f-MWCNT. Furthermore, agglomeration is almost negligible, probably due to the availability of the large number of nucleation sites on the surface of f-MWCNT. The porous structure of the f-MWCNT support is also seen, which is useful for fuel or oxidant transport from the bulk phase to active electrocatalysts sites for electrochemical reactions. In order to determine the carbon, oxygen, platinum, ruthenium, and rhenium elemental

distribution, FESEM, and corresponding color mapping were performed, as illustrated in Fig (5.28a) to Fig (5.28e).

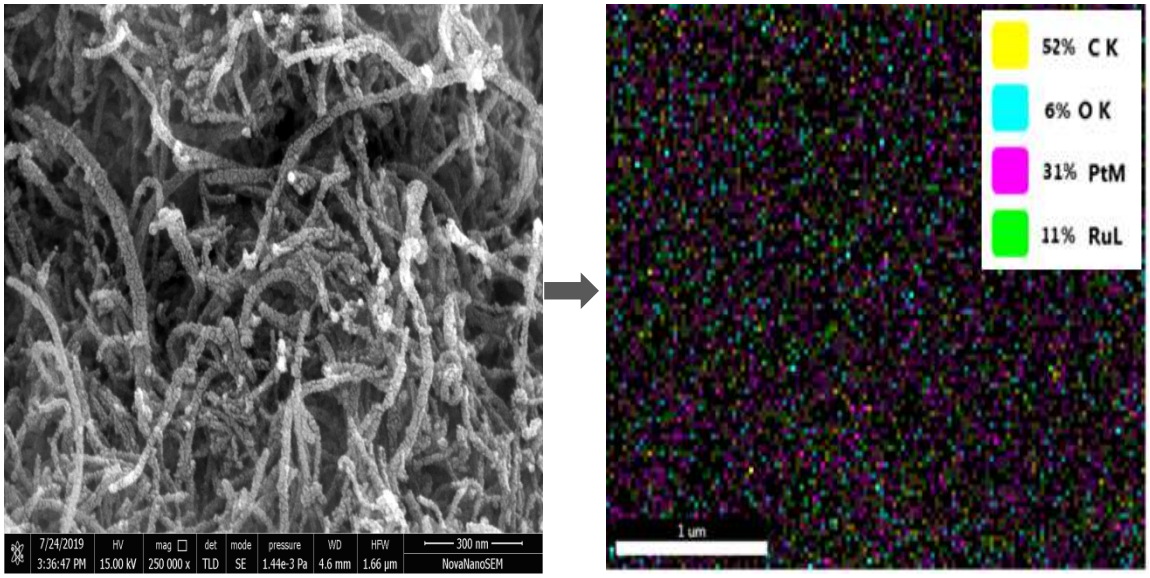

Figure 5.28a FESEM image and corresponding color mapping of Pt-Ru (1:1)/f-MWCNT electrocatalyst.

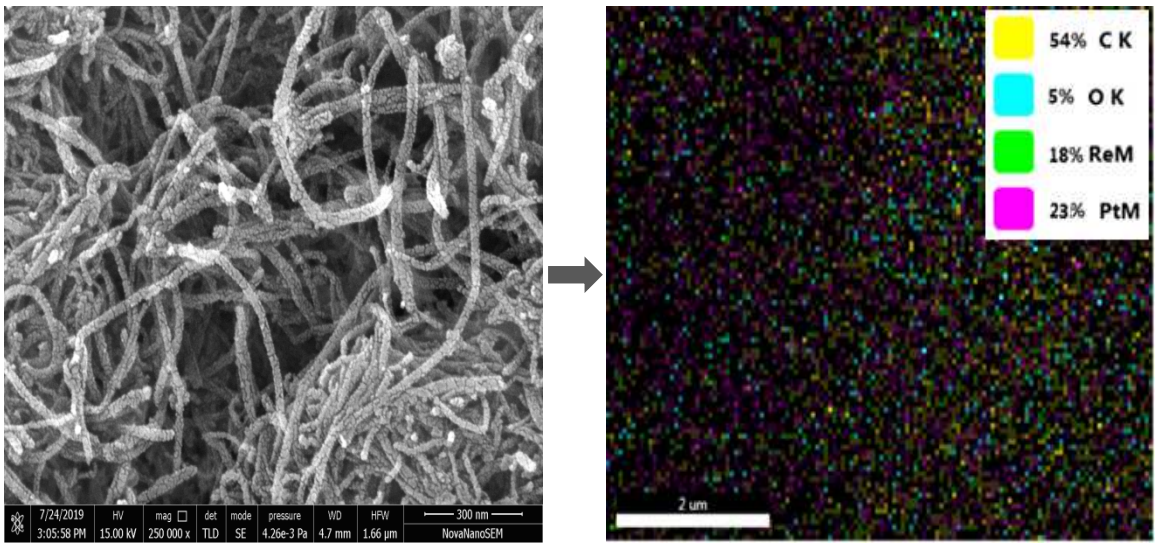

Figure 5.28b FESEM image and corresponding color mapping of Pt-Re (1:1)/f-MWCNT electrocatalyst.

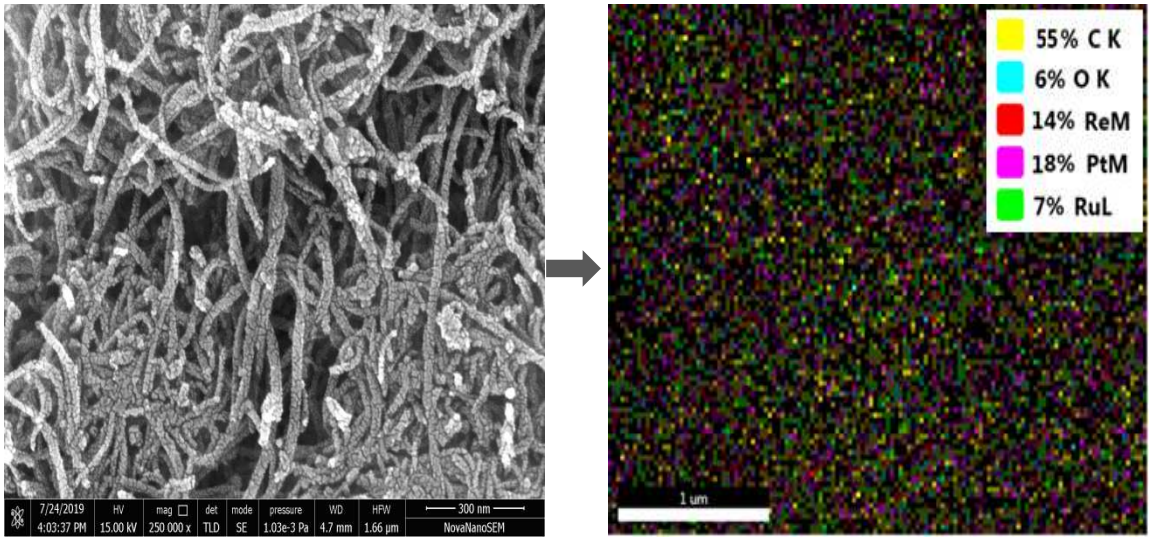

Figure 5.28c FESEM image and corresponding color mapping of Pt-Ru-Re (1:1:1)/f-MWCNT electrocatalyst.

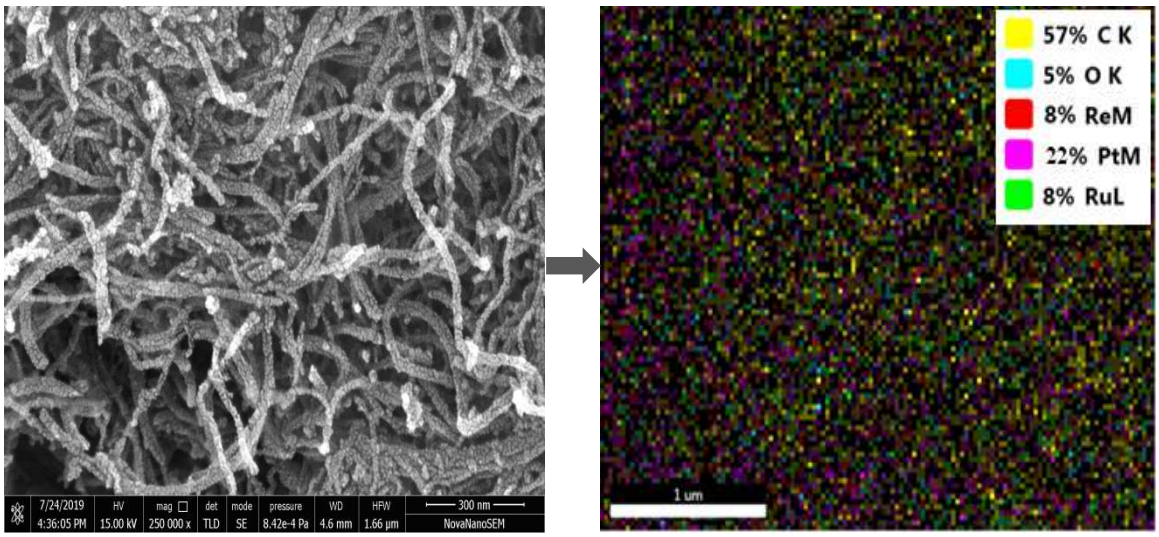

Figure 5.28d FESEM image and corresponding color mapping of Pt-Ru-Re (1:1:0.5)/f-MWCNT electrocatalyst.

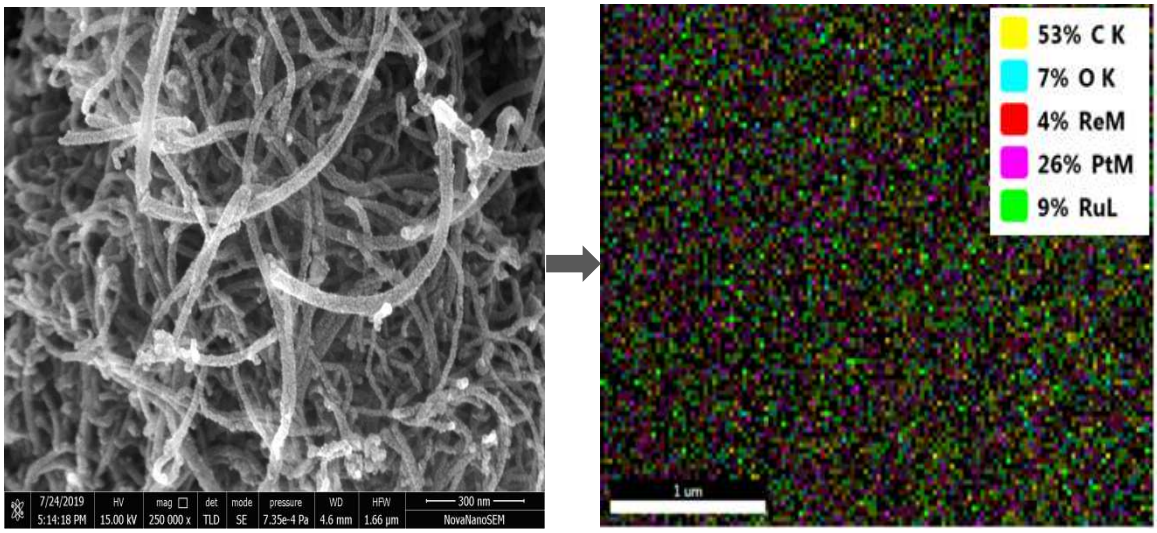

Figure 5.28e FESEM image and corresponding color mapping of Pt-Ru-Re (1:1:0.25)/f-MWCNT electrocatalyst.

It is observed from the color mapping of the synthesized electrocatalysts that each element with a different color is uniformly distributed in the entire image (Fig 5.28a to Fig 5.28e). The alloy formations of Pt, Ru, and/or Re were also clearly seen by FESEM elemental mapping. It is also observed that the Pt, Ru, and/or Re element exist almost in the same area, which confirms the formation of alloy nanostructure of the electrocatalyst. It should be noted that the EDX result provides here semi-quantitative information with a reasonable agreement between EDX results composition and nominal ones for all the electrocatalysts. Very minute discrepancies in actual metal loading of electrocatalysts with the nominal weight were noted, which could be associated with the metal losses during the separation and purification process (Table 5.17).

Table 5.17 Atomic composition of the synthesized bi-metallic and tri-metallic electrocatalysts evaluated from FESEM-EDX results.

Electrocatalysts	Nominal atomic ratio based on the precursor	Atomic ratio obtained by EDX
Pt-Ru (1:1)/f-MWCNT	1.0:1.0	1.46:1.0
Pt-Re (1:1)/f-MWCNT	1.0:1.0	1.21:1.0
Pt-Ru-Re (1:1:1)/f-MWCNT	1.0:1.0:1.0	1.33:1:1.08
Pt-Ru-Re (1:1:0.5)/f-MWCNT	1.0:1.0:0.5	1.42:1:0.543
Pt-Ru-Re (1:1:0.25)/f-MWCNT	1.0:1.0:0.25	1.49:1.0:0.24

5.2.3 Electrochemical characterization of anode electrocatalysts

5.2.3.1 Hydrogen adsorption/desorption study

The electrochemical performance of developed electrodes using all synthesized electrocatalysts were evaluated by cyclic voltammetry (CV) analysis in 0.5 M $HClO_4$ aqueous solution without ethanol. As it is shown in Fig (5.29), the voltammograms of electrocatalysts displayed prominent peaks related to the hydrogen adsorption/desorption process in the potential range of -0.4 V to 0.1 V and Pt surface oxidation/reduction region larger than 0.2 V. The oxide reduction and formation of the electrocatalysts appear at lower potential due to the incorporation of added foreign atoms Ru and Re on the electrocatalyst surface (Themsirimongkon et al., 2019). The hydrogen desorption peak of Pt-Ru-Re (1:1:0.5)/f-MWCNT was the highest and Pt-Re (1:1)/f-MWCNT was fair. Additionally, the current intensities in the hydrogen adsorption/desorption region were found to increase with the addition of foreign atoms in the Pt matrix. The charge densities of the Pt surface matrix could be changed by the incorporation of foreign metal atoms/species and chemical compositions.

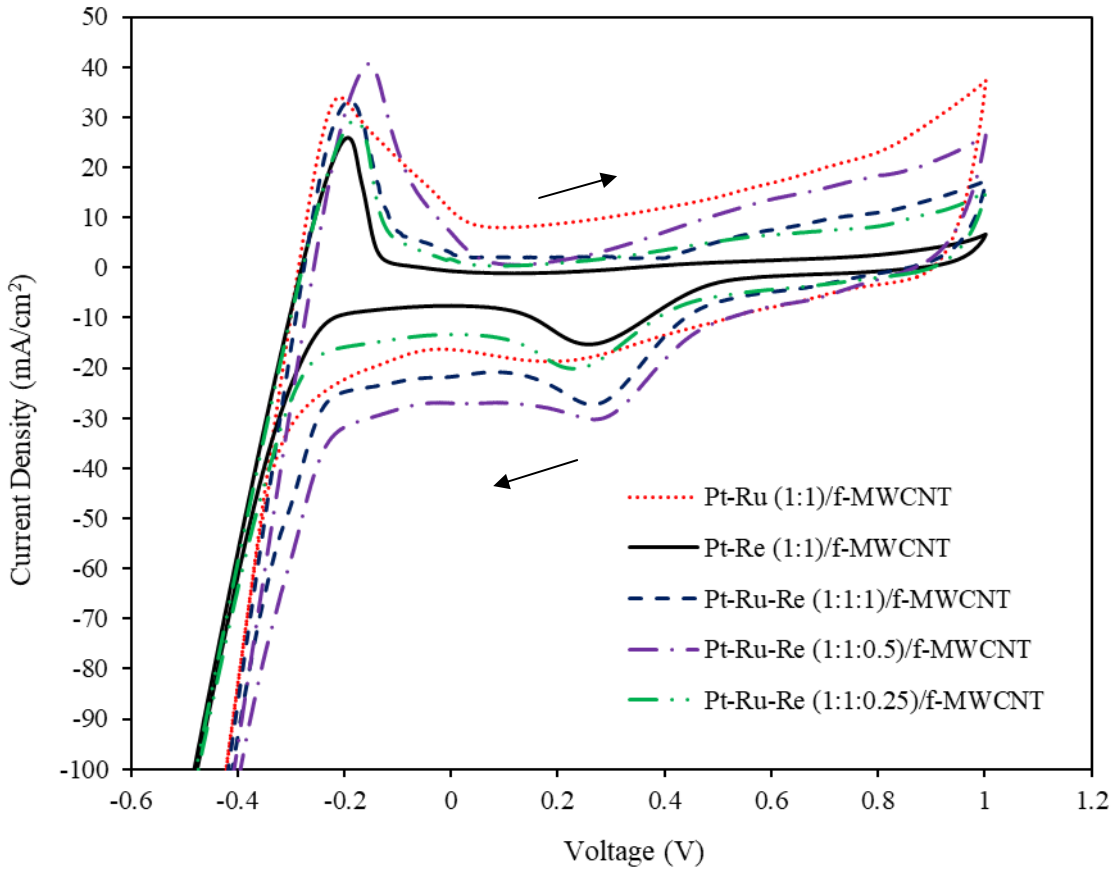

Figure 5.29 Cyclic voltammetry curves of Pt-Ru (1:1)/f-MWCNT, Pt-Re (1:1)/f-MWCNT, Pt-Ru-Re (1:1:1)/f-MWCNT, Pt-Ru-Re (1:1:0.5)/f-MWCNT and Pt-Ru-Re (1:1:0.25)/f-MWCNT electrocatalysts in 0.5 M $HClO_4$ at room temperature of 30 °C with a scan rate of 50 mV/s.

The electrochemically active surface area (ECSA) is an important parameter for electrocatalysts. The ECSA values of the electrode electrocatalysts were estimated by integration of the area under the CV curves corresponding to the hydrogen desorption region after double layer region correction and based on Equation (5.5) and information obtained from Fig (5.29) (Beyhan et al., 2013, Shen et al., 2015 and Themsirimongkon et al., 2019).

$$ECSA = \frac{S}{(v \times 0.21 \times 0.77 \times M_{Pt})} \tag{5.5}$$

Here, S is the hydrogen desorption area (mA Vcm^{-2}) in the CVs curve, v is the scanning rate 0.05 V/s, M_{Pt} is the Pt mass loading (mg cm^{-2}) on the electrode surface, 0.21 (mC cm^{-2}) represents the required charge to oxidize a monolayer of hydrogen desorption on bright Pt and 0.77 is the hydrogen monolayer coverage (Beyhan et al., 2013). According to the results displayed in Table (5.18), obviously, the Pt-Ru-Re (1:1:0.5)/f-MWCNT possesses the largest ECSA of 150.77 m^2/g, which is superior to tri-metallic Pt-Ru-Re (1:1:1)/f-MWCNT (127.66 m^2/g), Pt-Ru-Re (1:1:0.25)/f-MWCNT (73.60 m^2/g) and bi-metallic Pt-Ru (1:1)/f-MWCNT (85.31 m^2/g) and Pt-Re/f-MWCNT (54.55 m^2/g) electrocatalysts. The largest ECSA value of Pt-Ru-Re (1:1:0.5)/f-MWCNT electrocatalyst could be attributed to the smaller particle size and better distribution of nanoparticles on the f-MWCNT surface. It also predicts the best activity of Pt-Ru-Re (1:1:0.5)/f-MWCNT electrocatalyst in the half cell and single cell for ethanol electrooxidation giving excellent DEFC performance.

Table 5.18 Results of hydrogen desorption charge and its electrochemical active surface area (ECSA) of electrode electrocatalysts from CVs analysis.

Electrocatalysts	**Q_H[a] (mC/cm^2)**	**M_{Pt} (mg/cm^2)**	***ECSA*** **(m^2/g$_{Pt}$)**
Pt-Ru (1:1)/f-MWCNT	90.88	0.6588	85.31
Pt-Re (1:1)/f-MWCNT	45.13	0.5116	54.55
Pt-Ru-Re (1:1:1)/f-MWCNT	83.48	0.4044	127.66
Pt-Ru-Re (1:1:0.5)/f-MWCNT	122.19	0.5012	150.77
Pt-Ru-Re (1:1:0.25)/f-MWCNT	67.74	0.5692	73.60

[a]Calculated based on $Q_H = \frac{S}{v}$, where Q_H (mC/cm^2) represents the charges corresponding to desorption of hydrogen on the Pt surface, S is the hydrogen desorption area (mA V/cm^2) in the CVs curve, v is the scanning rate 0.05 V/s.

5.2.3.2 Cyclic voltammetry (CV) measurements of electrodes with ethanol

The cyclic voltammograms (CVs) of the synthesized electrocatalysts for ethanol electrooxidation were recorded in 2 M ethanol mixed with 0.5 M $HClO_4$ solution using the same synthesized electrocatalysts which were used in previous section 5.2.3.1 (Page no. 189) and presented in Fig (5.30). The loading of electrocatalysts were 1 mg/cm^2 for each electrode.

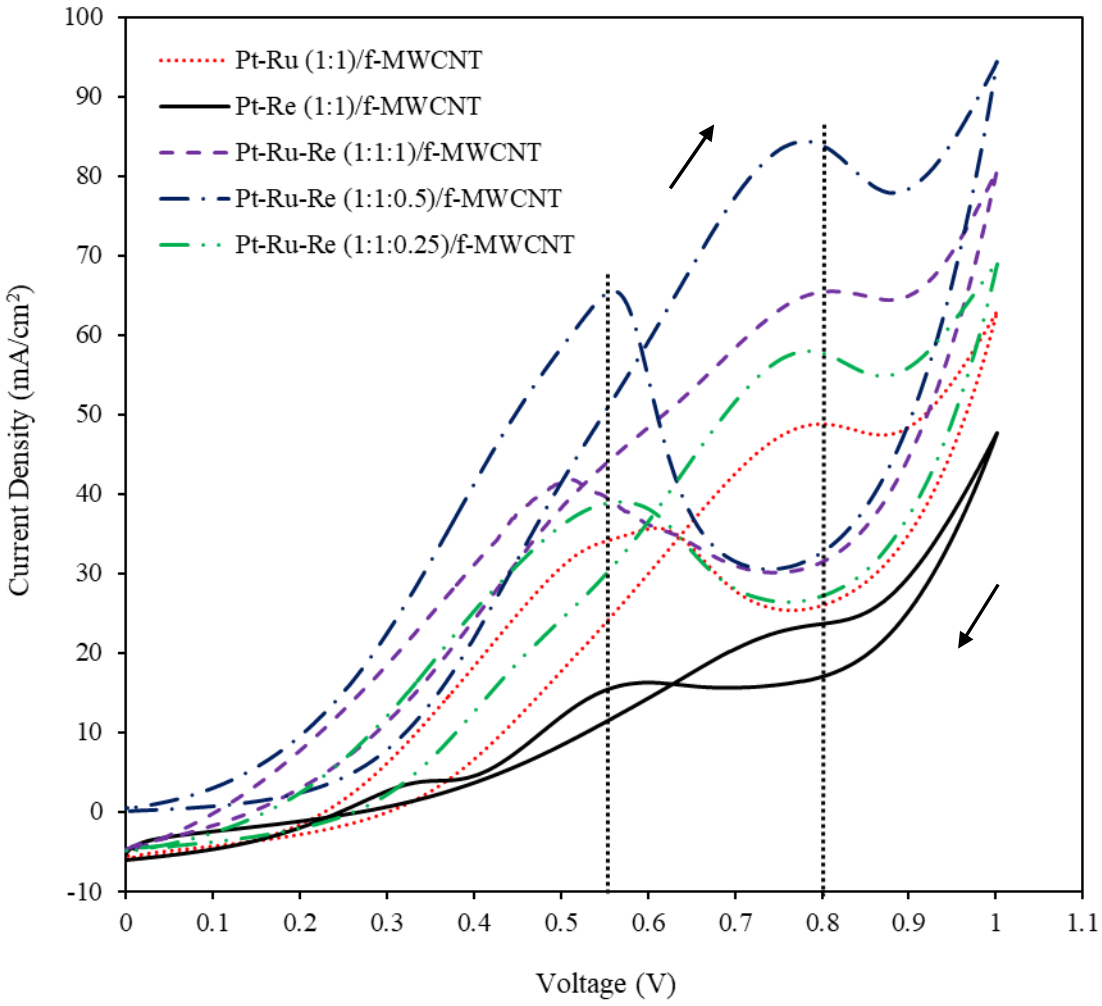

Figure 5.30 CVs characteristics for ethanol electrooxidation on Pt-Ru (1:1)/f-MWCNT, Pt-Re (1:1)/f-MWCNT, Pt-Ru-Re (1:1:1) /f-MWCNT, Pt-Ru-Re (1:1:0.5)/f-MWCNT and Pt-Ru-Re (1:1:0.25)/f-MWCNT electrocatalysts in 2 M ethanol + 0.5 M $HClO_4$ solution at room temperature of 30 ^oC with a scan rate of 5 mV/s.

The CVs of the electrocatalysts showed well-defined electrooxidation peaks for ethanol fuel in the forward and backward scans. The prominent electrooxidation peak during the forward scan is attributed to the electrooxidation of freshly chemisorbed species and the peaks at backward scan were related to the additional electrooxidation of adsorbed carbonaceous species formed during the forward scan to carbon dioxide.

The noticeable CV peaks obtained for ethanol fuel on the electrocatalysts Pt-Ru (1:1)/f-MWCNT, Pt-Re (1:1)/f-MWCNT, Pt-Ru-Re (1:1:1)/f-MWCNT, Pt-Ru-Re (1:1:0.5)/f-MWCNT, and Pt-Ru-Re (1:1:0.25)/f-MWCNT are tabulated in Table (5.19), including onset potential, forward scanning oxidation peak potential (E_f), forward scanning oxidation current density (I_f), backward scanning oxidation peak potential (E_b) and backward scanning oxidation current density (I_b) of electrocatalysts.

Table 5.19 Summary of electrocatalytic performance of electrocatalysts towards ethanol electrooxidation.

Electrocatalysts	**Onset potential (V)**	**E_f (V)**	**I_f (mA/cm^2)**	**E_b (V)**	**I_b (mA/cm^2)**
Pt-Ru (1:1)/f-MWCNT	0.30	0.794	48.76	0.610	35.66
Pt-Re (1:1)/f-MWCNT	0.28	0.798	23.60	0.598	16.23
Pt-Ru-Re (1:1:1)/f-MWCNT	0.15	0.808	65.46	0.513	41.79
Pt-Ru-Re (1:1:0.5)/f-MWCNT	0.10	0.781	83.34	0.559	65.53
Pt-Ru-Re (1:1:0.25)/f-MWCNT	0.25	0.785	57.94	0.570	38.96

The ethanol electrooxidation on Pt-Re/f-MWCNT and Pt-Ru/f-MWCNT started at around 0.30 mV, while the onset potentials for tri-metallic electrocatalysts Pt-Ru-Re (1:1:1)/f-

MWCNT, Pt-Ru-Re (1:1:0.5)/f-MWCNT and Pt-Ru-Re (1:1:0.25)/f-MWCNT were determined to be 0.15 V, 0.10 V, and 0.25 V, respectively. Moreover, the introduction of rhenium (Re) into Pt-Ru/f-MWCNT significantly reduces the onset potential by 0.2 V (Table 5.19) in tri-metallic electrocatalyst Pt-Ru-Re (1:1:0.5)/f-MWCNT and increases the current density. The current densities (I_f) for the tri-metallic electrocatalysts Pt-Ru-Re (1:1:0.5)/f-MWCNT (83.34 mA/cm^2), Pt-Ru-Re (1:1:1)/f-MWCNT (65.46 mA/cm^2) and Pt-Ru-Re (1:1:0.25)/f-MWCNT (57.94 mA/cm^2) are significantly higher than the bi-metallic Pt-Re (1:1)/f-MWCNT (23.60 mA/cm^2) and Pt-Ru (1:1)/f-MWCNT (48.76 mA/cm^2), while no significant shifts in their E_f are observed (Table 5.19). The highest peak current density of 83.34 mA/cm^2 was obtained for the Pt-Ru-Re (1:1:0.5)/f-MWCNT. The current densities of the synthesized electrocatalysts for ethanol electrooxidation in CVs study increased in the ascending order of Pt-Re (1:1)/f-MWCNT < Pt-Ru (1:1)/f-MWCNT < Pt-Ru-Re (1:1:1)/f-MWCNT < Pt-Ru-Re (1:1:0.25)/f-MWCNT < Pt-Ru-Re (1:1:0.5)/f-MWCNT.

The electrochemical reactions on the surface of Pt-based electrocatalyst nanoparticles during ethanol electrooxidation occur via a double pathway mechanism (Choudhary and Pramanik, 2019 and Themsirimongkon et al., 2019). The enhanced electrocatalytic activities of Pt-based electrocatalysts were explained through the cooperative result of the bi-functional, ligand, and strain effects as discussed earlier. The addition of Re atoms to Pt lattice resulted in substantial lattice contraction as discussed in the XRD section. Such lattice contraction is the cause of lattice strain effects, could also shift the d-band center of Pt atoms away from the Fermi level, and reduces the bonding strength and coverage of intermediates on the Pt surface. Thus, the superior electrocatalytic activity of Pt-Ru-Re (1:1:0.5)/f-MWCNT electrocatalysts among synthesized electrocatalysts was ascribed to

the synergistic effects of constituents and excellent conductive f-MWCNT support. The positive effects of Re addition to Pt-based electrocatalysts in the breaking of C-C bond during ethanol electrooxidation were also reported by Tayal et al., (2012). Moreover, the smallest particle size of Pt-Ru-Re (1:1:0.5)/f-MWCNT (Fig 5.26d and Fig 5.27d) probably might give the highest electrochemical active surface area and thus, results in the highest interactions with ethanol molecule. This may results in better ethanol electrooxidation kinetics at the anode with very high current density. As the structural defects or surface roughness of this particular electrocatalyst is very high and thus, activation loss should also below, which consequently must give higher operating cell voltage and current density in single cell experiments for ethanol fuel.

5.2.3.3 Chronoamperometry (CA) analysis

The chronoamperometry (CA) experiments were carried out to examine the electrochemical performance and stability of the electrocatalysts for ethanol electrooxidation. The electrochemical stability of electrocatalysts was measured in 2 M ethanol mixed with 0.5 M $HClO_4$ solution at two constant potentials of 0.55 V and 0.8 V for 900 s, respectively (Fig 5.31a and Fig 5.31b). In all CA curves (Fig 5.31a and Fig 5.31b), the current densities for all the electrocatalysts decayed rapidly during the first few minutes i.e. 10 minutes and then reached relatively stable values after 10 minutes for both potentials (Fig 5.31a and Fig 5.31b). The dramatic decay of current densities could be due to the poisoning of surface active sites of electrocatalysts from carbonaceous intermediates, instability of electrocatalyst nanoparticles, and diffusional effects (Tayal et al., 2011 and Tayal et al., 2012). After about 10 minutes, the adsorption and oxidation rates of the intermediates are in equilibrium, so the current density curve tends to stabilize (Qin et al., 2019). The tri-metallic Pt-Ru-Re (1:1:0.5)/f-MWCNT electrocatalysts attained

higher current density than bi-metallic Pt-Re (1:1)/f-MWCNT and Pt-Ru (1:1)/f-MWCNT and other tri-metallic electrocatalysts. The superior activity of Pt-Ru-Re (1:1:0.5)/f-MWCNT can be attributed to the modification of electronic properties and the presence of ruthenium oxides resulting in a combination of bi-functional, ligand, and strain effects (Shen et al., 2015). The ethanol electrooxidation current density for Pt-Ru-Re (1:1:0.5)/f-MWCNT was higher than all the other electrocatalysts in the entire testing time at both reference potentials (0.55 V and 0.8 V).

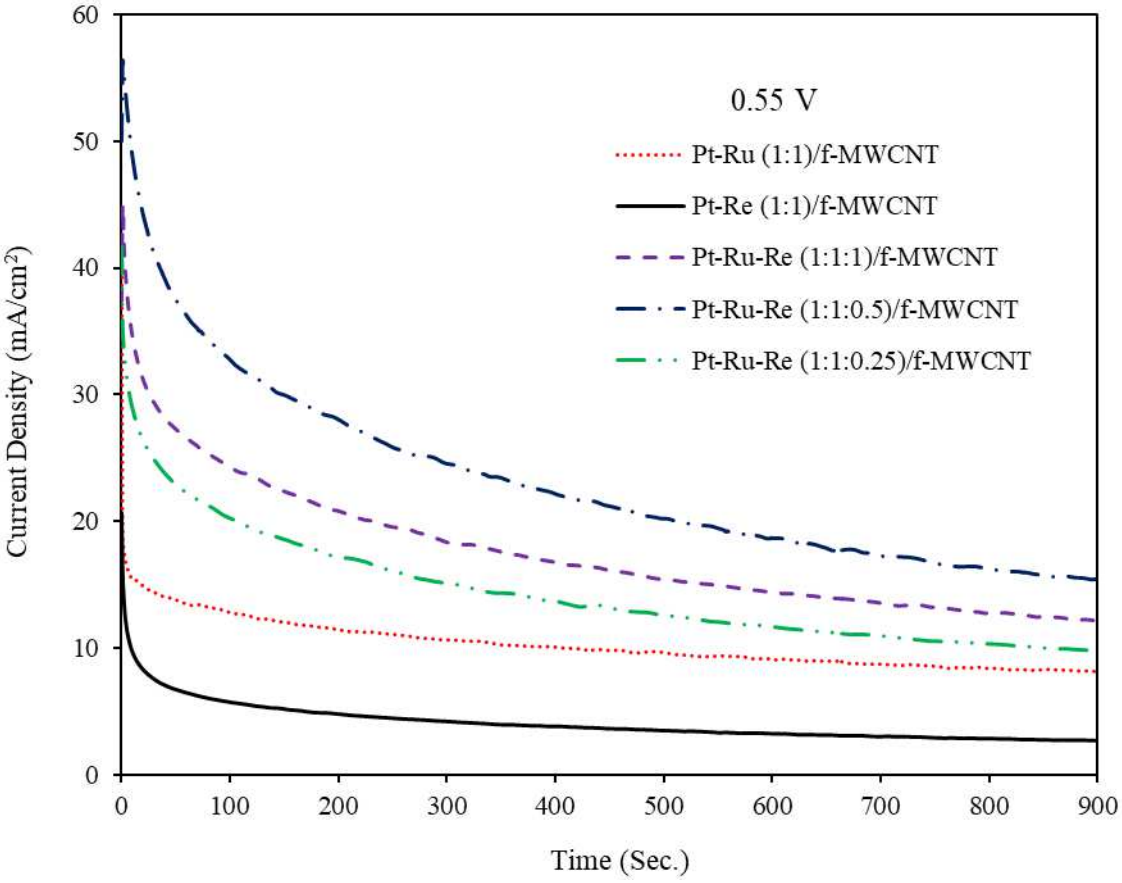

Figure 5.31a CA curves of Pt-Ru (1:1)/f-MWCNT, Pt-Re (1:1)/f-MWCNT, Pt-Ru-Re (1:1:1) /f-MWCNT, Pt-Ru-Re (1:1:0.5)/f-MWCNT and Pt-Ru-Re (1:1:0.25)/f-MWCNT electrocatalysts recorded in 2 M ethanol + 0.5 M $HClO_4$ solution at fixed potential of 0.55 V vs. Ag/AgCl at room temperature of 30 °C.

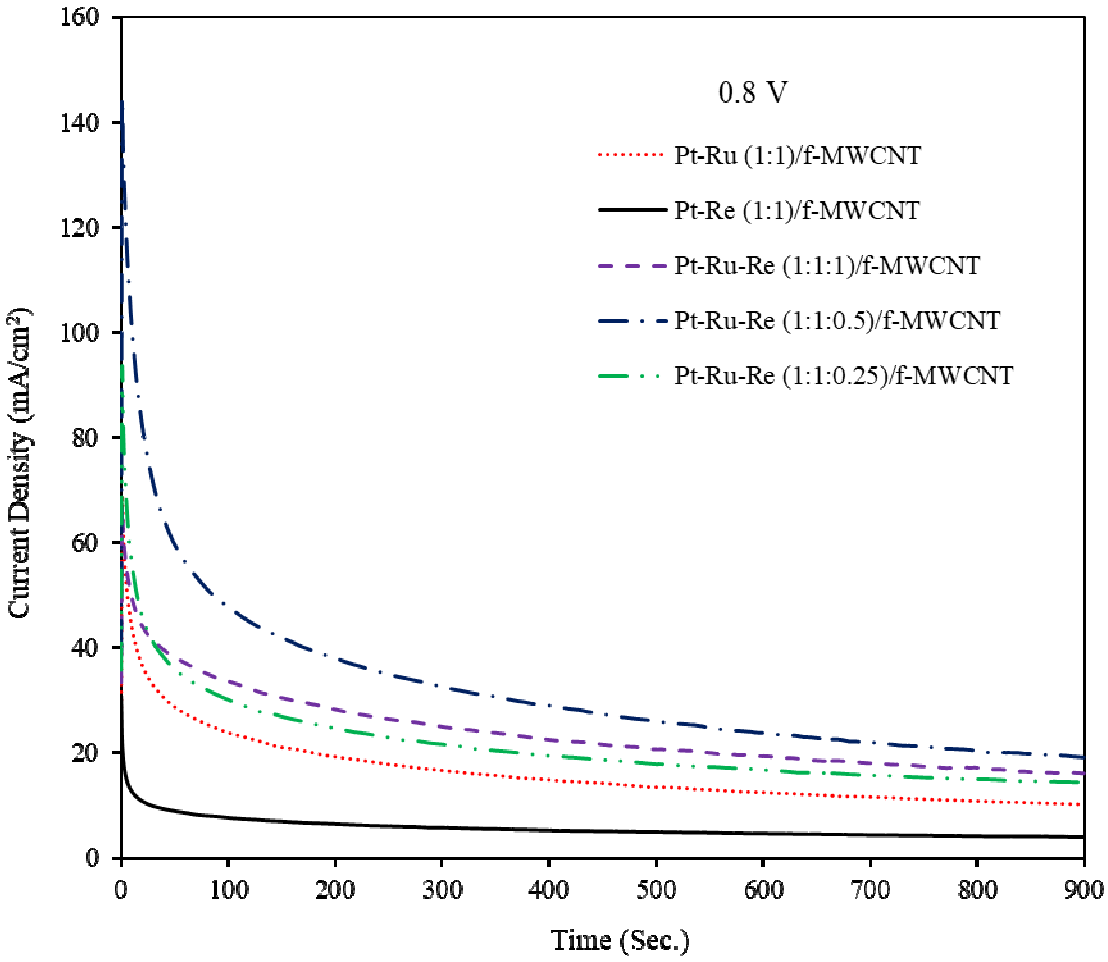

Figure 5.31b CA curves of Pt-Ru (1:1)/f-MWCNT, Pt-Re (1:1)/f-MWCNT, Pt-Ru-Re (1:1:1) /f-MWCNT, Pt-Ru-Re (1:1:0.5)/f-MWCNT and Pt-Ru-Re (1:1:0.25)/f-MWCNT electrocatalysts recorded in 2 M ethanol + 0.5 M $HClO_4$ solution at fixed potential of 0.8 V vs. Ag/AgCl at room temperature of 30 °C.

The stable current obtained for Pt-Ru-Re (1:1:0.5)/f-MWCNT at 900 s was 19.1 mA/cm^2, which is higher than all the other electrocatalysts, suggesting the higher stability of Pt-Ru-Re (1:1:0.5) /f-MWCNT (Fig 5.31b). The similar trend of highest current density (15.4 mA/cm^2) of Pt-Ru-Re (1:1:0.5)/f-MWCNT as observed in Fig (5.31a), was also noticed in Fig (5.31b) for the potential 0.8 V. The stable current densities obtained after 900 s at both reference potentials 0.55 V and 0.8 V were consistent with the CV results.

5.2.4 FESEM observation of electrode

The electrocatalytic performances of the synthesized electrocatalysts in half cell, show that the Pt-Ru-Re (1:1:0.5)/f-MWCNT is exhibiting the better activity for ethanol electrooxidation. Thus the loading of the best electrocatalyst Pt-Ru-Re (1:1:0.5)/f-MWCNT was varied from 0.5 mg/cm^2 to 1.5 mg/cm^2 and surface morphology of the developed electrodes were studied through FESEM analysis. The main purpose/aim of this study/analysis was to correlate the DEFC results for varying load of anode and cathode electrocatalyst with the surface morphology like agglomeration and uniform distribution of electrocatalyst.

5.2.4.1 FESEM of anode

The FESEM image for the blank GDL carbon paper is presented in Fig (5.32a) and that for the sintered mass of laboratory synthesized anode electrocatalyst Pt-Ru-Re (1:1:0.5)/f-MWCNT various loads ranging from 0.5 mg/cm^2 to 1.5 mg/cm^2 are shown in Fig (5.32b), to Fig (5.32d), respectively. The blank GDL demonstrates the distinct and even distribution of rod-like structure carbon fibers with PTFE interconnecting film that makes the GDL/carbon paper porous. The GDL/carbon paper consists of 10 % PTFE dispersion to form a porous structure and a broader pore size distribution. Fig (5.32c) shows a uniform distribution of Pt-Ru-Re (1:1:0.5)/f-MWCNT electrocatalyst on the GDL/carbon paper with porous morphology for loading of 1 mg/cm^2. The porous electrode structure ensures the continuous supply of fuel and oxidant to the anode and cathode electrocatalyst layer, respectively, and enables access to the active electrocatalyst sites for faster electrochemical reaction rates**.** The FESEM image (Fig 5.32d) for electrocatalyst anode with a maximum loading of 1.5 mg/cm^2 shows a slightly denser, less porous surface morphology of the electrocatalyst layer.

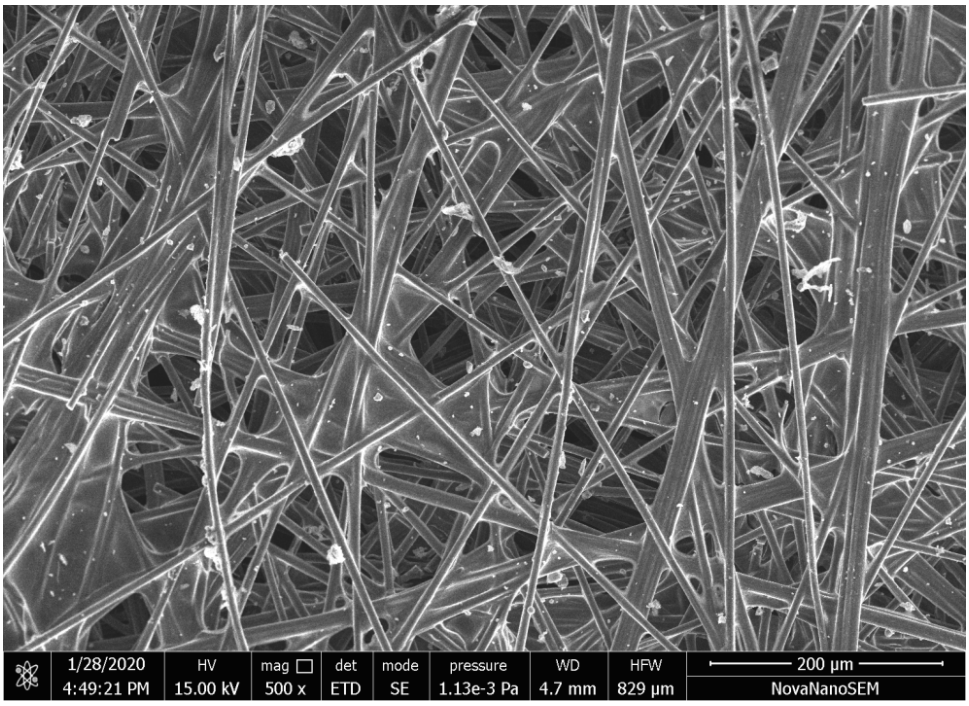

Figure 5.32a FESEM image of blank GDL/carbon paper.

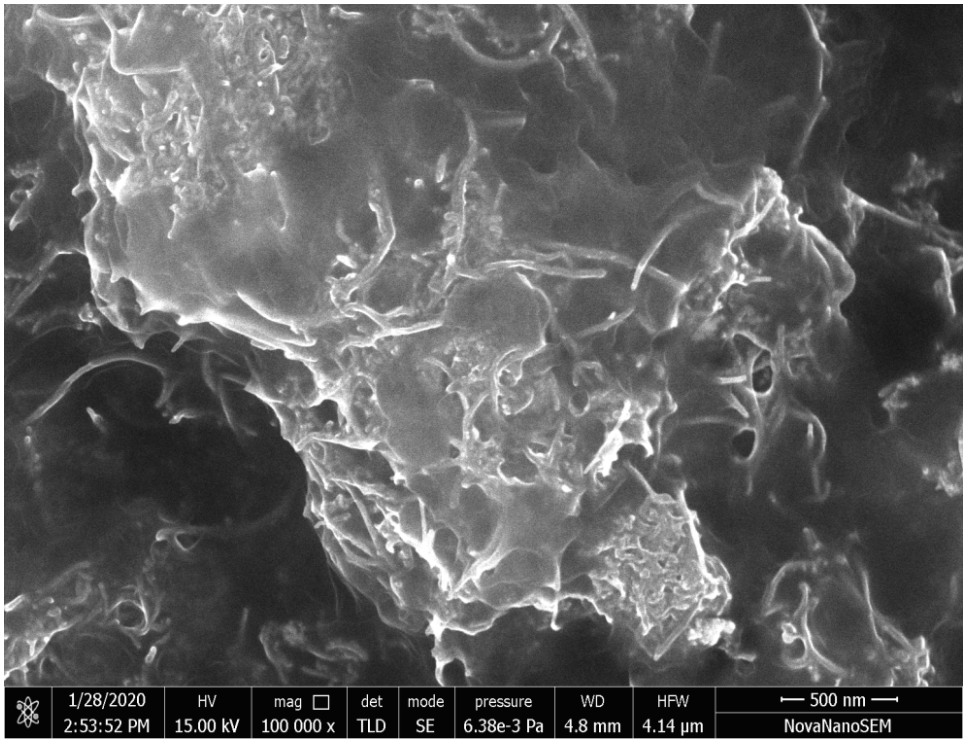

Figure 5.32b FESEM image of anode electrocatalyst Pt-Ru-Re (1:1:0.5)/f-MWCNT loading of 0.5 mg/cm^2.

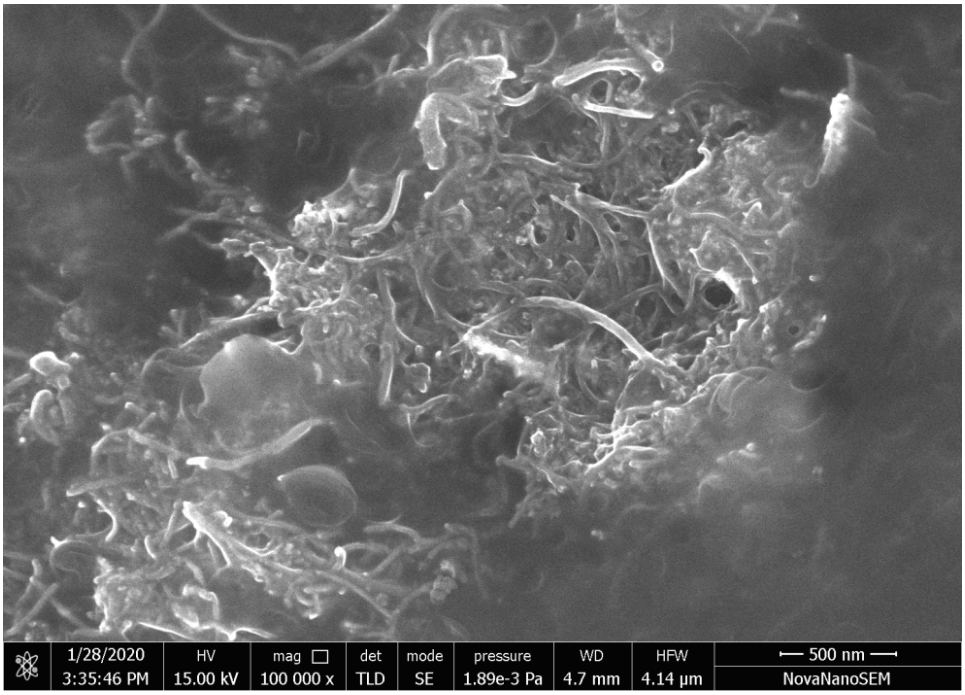

Figure 5.32c FESEM image of anode electrocatalyst Pt-Ru-Re (1:1:0.5)/f-MWCNT loading of 1 mg/cm^2.

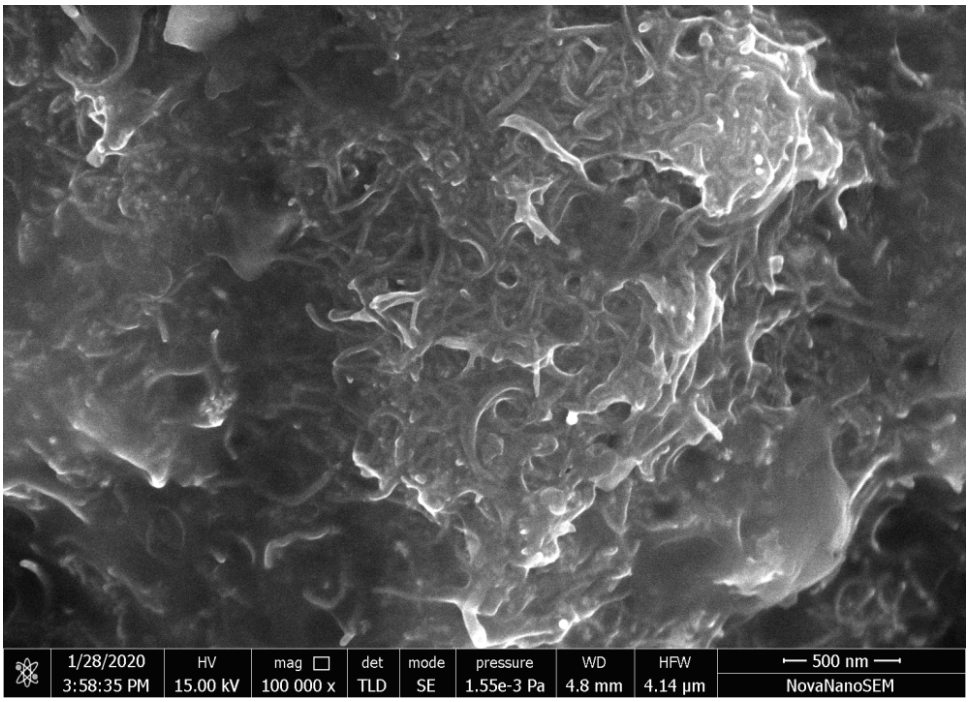

Figure 5.32d FESEM image of anode electrocatalyst Pt-Ru-Re (1:1:0.5)/f-MWCNT loading of 1.5 mg/cm^2.

Some researchers have argued that as electrocatalyst loading increases, the active surface area of the electrode increases, and that beyond a certain loading, the active surface area decreases (Pramanik and Basu, 2007, Pramanik and Rathoure 2017 and Panjiara and Pramanik, 2020a). With an additional increase in electrocatalyst loading above 1.5 mg/cm^2, nanoparticle electrocatalyst agglomeration occurs and therefore the porosity of the electrocatalyst layer is reduced.

5.2.4.2 FESEM of cathode

Fig (5.33a) to Fig (5.33c) show the FESEM of cathode electrodes of varying electrocatalyst loading ranging from 0.5 mg/cm^2 to 1.5 mg/cm^2 of Pt (40 wt. %)/C_{HiSPEC}, respectively. Fig (5.33b) shows the even distribution of Pt (40 wt. %)/C_{HiSPEC} electrocatalyst over the GDL surface along with pores for the loading of 1 mg/cm^2 in comparison to that of loading 0.5 mg/cm^2 (Fig 5.33a). The FESEM image (Fig 5.33c) for electrocatalyst anode with a maximum loading of 1.5 mg/cm^2 shows a slightly denser, less porous surface morphology of the electrocatalyst layer.

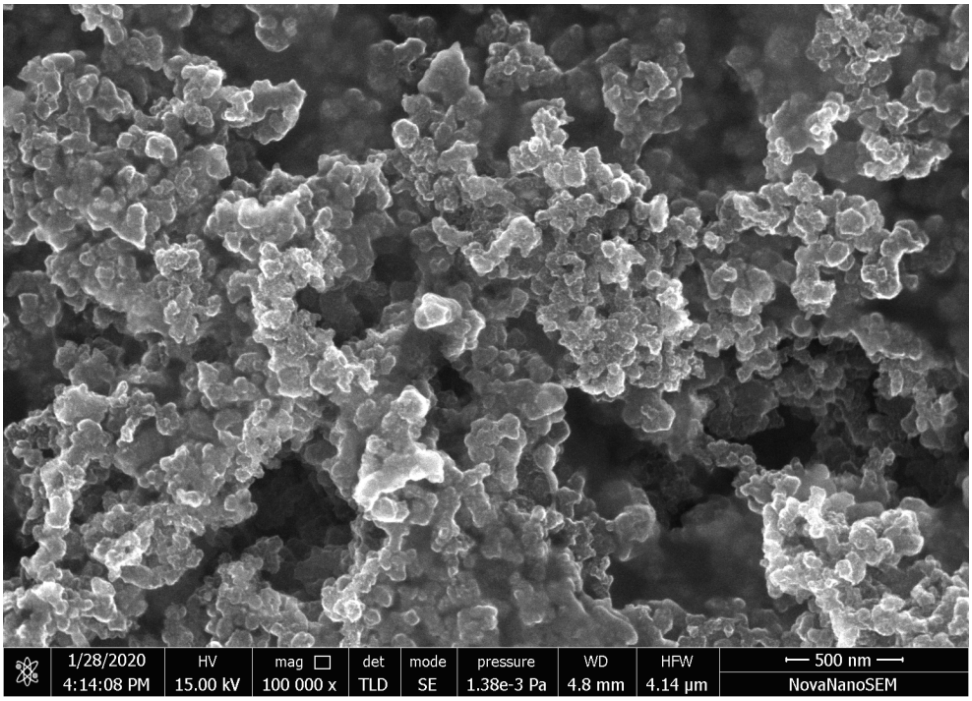

Figure 5.33a FESEM image of cathode electrocatalyst commercial Pt/C_{HiSPEC} loading of 0.5 mg/cm^2.

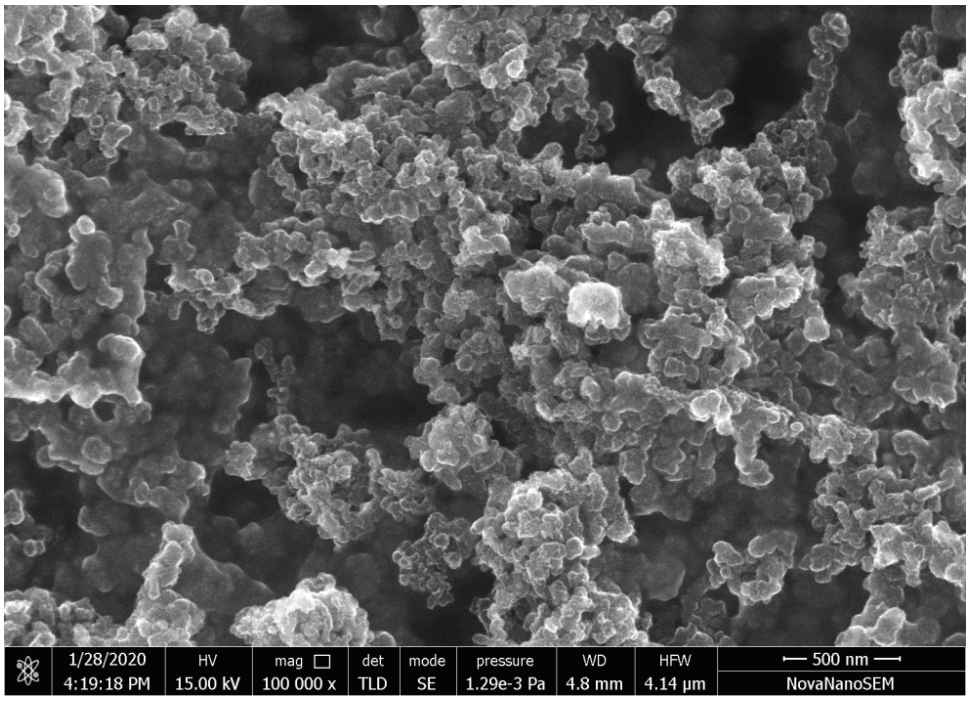

Figure 5.33b FESEM image of cathode electrocatalyst commercial Pt/C_{HiSPEC} loading of 1 mg/cm^2.

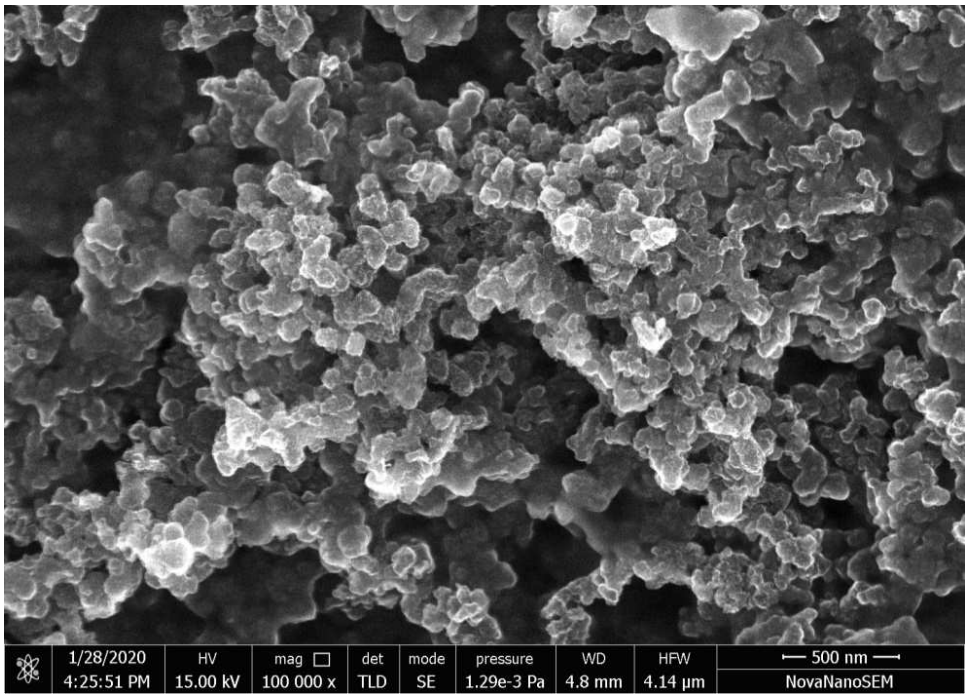

Figure 5.33c FESEM image of cathode electrocatalyst commercial Pt/C_{HiSPEC} loading of 1.5 mg/cm^2.

5.2.5 DEFC study

5.2.5.1 Effect of support functionalization

Fig (5.34) shows the polarization curves and power density curves for the Pt-Ru (1:1)/p-MWCNT and Pt-Ru (1:1)/f-MWCNT as anode electrocatalysts and commercial Pt (40 % wt.)/C_{HiSPEC} as cathode electrocatalyst at a cell temperature of 30 °C. The electrocatalyst loading at the anode and the cathode electrode were fixed at optimum loading of 1 mg/cm^2. It is seen in Fig (5.34) that the maximum OCV of 0.665 V and 0.683 V were produced for fuel ethanol (2 M) using Pt-Ru (1:1)/p-MWCNT and Pt-Ru (1:1)/f-MWCNT as anode electrocatalysts, respectively. The maximum power density of 6.57 mW/cm^2 at a current density of 27.36 mA/cm^2 and maximum power density of 7.48 mW/cm^2 at a current density of 30.4 mA/cm^2 were obtained for Pt-Ru (1:1)/p-MWCNT and Pt-Ru

(1:1)/f-MWCNT as anode electrocatalysts, respectively**.** It is observed that f-MWCNT supported Pt-Ru electrocatalyst exhibits superior cell performance in comparison to p-MWCNT supported Pt-Ru electrocatalyst. The better electrocatalytic activity of Pt-Ru (1:1)/f-MWCNT for ethanol electrooxidation can be attributed to a small number of organic impurities, smaller metal crystallite size and higher alloyed Ru as explained in XRD analysis.

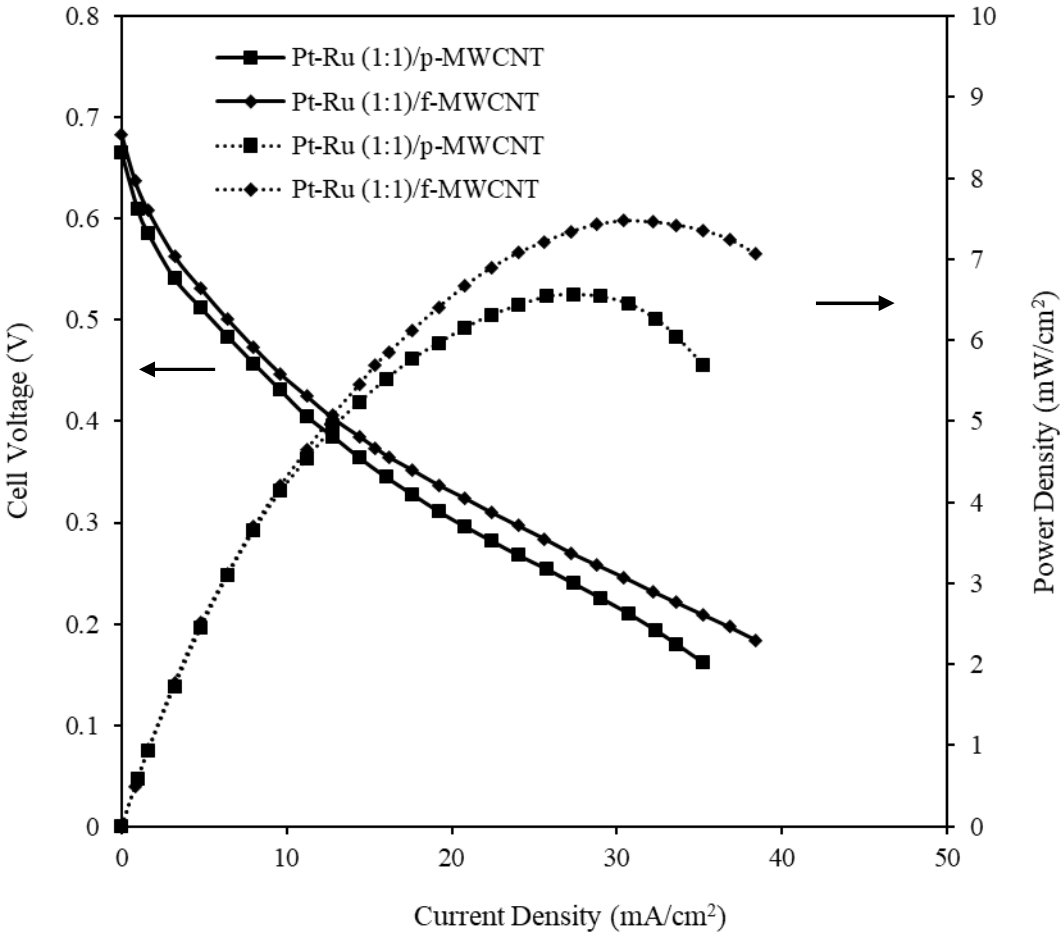

Figure 5.34 Single cell performance characteristics for anode electrocatalysts Pt-Ru (1:1)/p-MWCNT and Pt-Ru (1:1)/f-MWCNT using anode feed of 2 M ethanol solution. Cathode feed: humidified pure oxygen; $P_{cathode}$ = 1 bar (absolute); Solid line-polarization curves; Dotted line-power density curves.

5.2.5.2 Effect of anode electrocatalysts type

Due to the better electrocatalytic activity of Pt-Ru electrocatalyst supported on functionalized MWCNT i.e., Pt-Ru/f-MWCNT (Fig 5.34), all the synthesized bi-metallic and tri-metallic electrocatalysts presented here are supported on f-MWCNT. Fig (5.35) shows the comparison of the single cell DEFC performance curves for the Pt-Ru (1:1)/f-MWCNT, Pt-Re (1:1)/f-MWCNT, Pt-Ru-Re (1:1:1)/f-MWCNT, Pt-Ru-Re (1:1:0.5)/f-MWCNT and Pt-Ru-Re (1:1:0.25)/f-MWCNT as anode electrocatalysts and commercial Pt (40 % wt.)/C_{HiSPEC} as cathode electrocatalyst at a cell temperature of 30 °C.

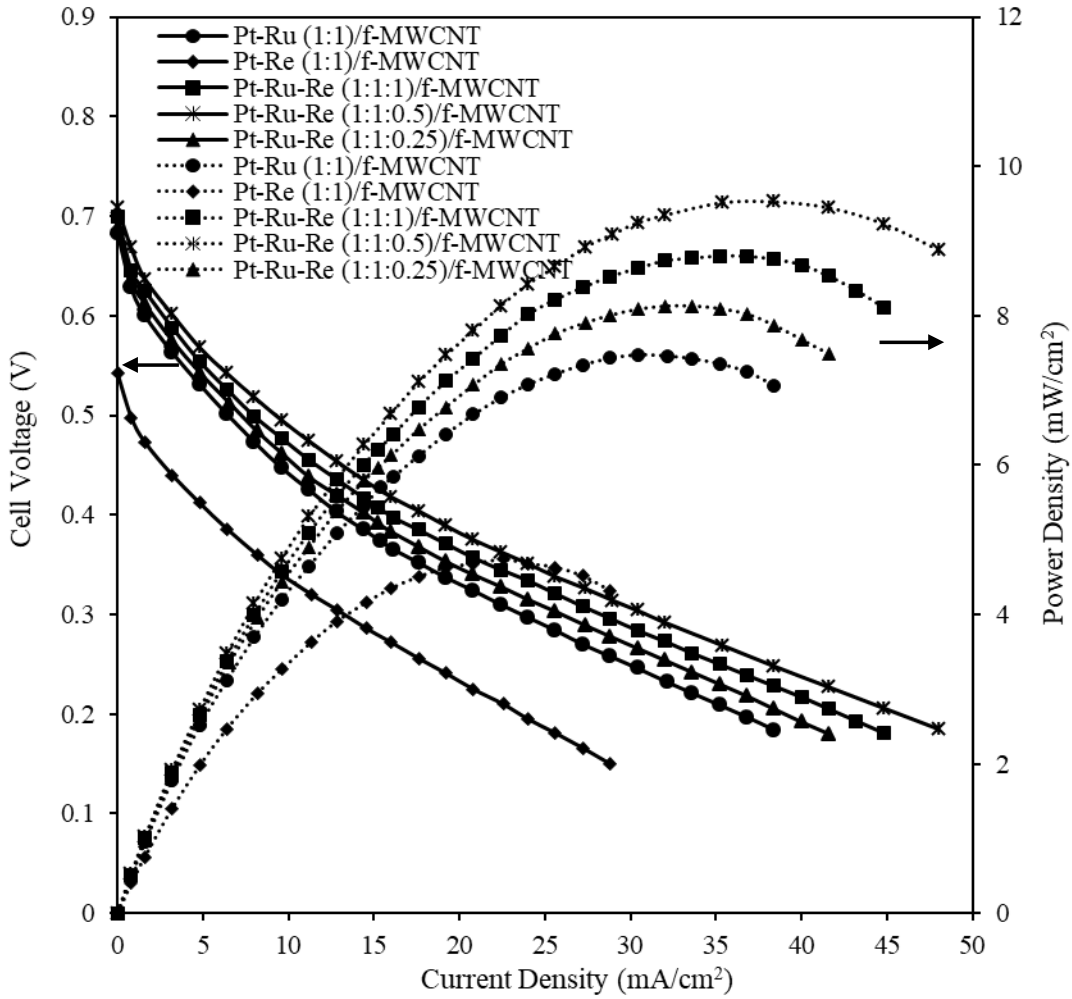

Figure 5.35 Single cell performance characteristics for different anode electrocatalysts using anode feed of 2 M ethanol solution. Cathode feed: humidified pure oxygen; $P_{cathode}$ = 1 bar (absolute); Solid line-polarization curves; Dotted line-power density curves.

The electrocatalyst loading at the anode and the cathode electrode was fixed at 1 mg/cm^2. In Table (5.20), the maximum values of single cell DEFC performance results such as open circuit voltage (OCV), power density, and current density are summarized for comparative study. In the low current density region, the voltage drop at a fixed current density in a single cell is very close for all the electrocatalyst except Pt-Re (1:1)/f-MWCNT. Furthermore, a rapid fall in cell voltage was observed for all electrocatalysts except Pt-Ru-Re/f-MWCNT, which were due to the slow initial ethanol electrooxidation reaction and high activation losses at the electrode surface.

Table 5.20 Summary of performance of different anode electrocatalysts in single cell DEFC tests for 2 M ethanol at a cell temperature of 30 °C.

Anode electrocatalyst	OCV (V)	Maximum power density (mW/cm^2)	Current density at maximum power density (mA/cm^2)
Pt-Re (1:1)/f-MWCNT	0.542	4.74	22.56
Pt-Ru (1:1)/f-MWCNT	0.683	7.48	30.40
Pt-Ru-Re (1:1:1)/f-MWCNT	0.70	8.8	35.20
Pt-Ru-Re (1:1:0.5)/f-MWCNT	0.708	9.52	38.40
Pt-Ru-Re (1:1:0.25)/f-MWCNT	0.688	8.13	33.60

It is observed from the comparative single cell study, initial fall in voltage is pronounced in the case of Pt-Re (1:1)/f-MWCNT electrocatalyst due to very high activation loss, which is similar to the result reported by Tayal et al., (2012). There is a sharp dip in cell voltage with an increase in current density was observed for Pt-Re (1:1)/f-MWCNT electrocatalyst indicating the cell has undergone through ohmic overpotential. This study shows that the cell performance using Pt-Re (1:1)/f-MWCNT as anode electrocatalyst for ethanol electrooxidation is not up to mark. The cell performance was improved, when Pt-

Ru (1:1)/f-MWCNT was adopted as anode electrocatalyst. For bi-metallic Pt-Re (1:1)/f-MWCNT and Pt-Ru (1:1)/f-MWCNT, the maximum power density of 4.74 mW/cm^2 and 7.47 mW/cm^2 was obtained at a current density of 22.56 mA/cm^2 and 22.40 mA/cm^2, respectively. The maximum open circuit voltage (OCV) of 0.683 V was obtained for Pt-Ru (1:1)/f-MWCNT, which was also higher than that of the Pt-Re (1:1)/f-MWCNT (0.542 V), suggesting there is a difference in ethanol oxidation reaction mechanism. Further, the addition of Re to the bi-metallic Pt-Ru (1:1)/f-MWCNT is clearly enhancing the ethanol oxidation reaction as seen from the polarization curves Fig (5.35). When adopting tri-metallic Pt-Ru-Re (1:1:0.5)/f-MWCNT electrocatalysts as anode, it remarkably improves the DEFC cell performance compared to bi-metallic Pt-Re (1:1)/f-MWCNT, Pt-Ru (1:1)/f-MWCNT and other tri-metallic Pt-Ru-Re (1:1:0.25)/f-MWCNT and Pt-Ru-Re (1:1:1)/f-MWCNT electrocatalysts (Table 5.20). It is observed from a single cell comparative study that the performance of Pt-Ru-Re (1:1:0.5)/f-MWCNT electrocatalyst is superior to other synthesized electrocatalysts. The highest power density of 9.52 mW/cm^2 at a current density of 38.4 mA/cm^2 was obtained for Pt-Ru-Re (1:1:0.5)/f-MWCNT. The obtained OCV for this electrocatalyst was the highest (0.708 V) among all electrocatalysts. The addition of Re to the bi-metallic Pt-Ru/f-MWCNT is conducive for the breaking of C-C bonds in ethanol molecules, but a higher percentage of Re in Pt-Ru-Re (1:1:1)/f-MWCNT blocks the further oxidation of intermediates. It may be due to barriers to the adsorption of the intermediates on the active sites of the electrocatalysts. This confirms that only a small of Re addition in Pt-Ru (1:1)/f-MWCNT electrocatalyst favors in breaking of C-C bonds in the electrooxidation of ethanol. It should also be noted that Pt-Ru-Re (1:1:0.5)/f-MWCNT showed excellent physical and electrochemical properties which have already been discussed in the section of electrocatalyst characterizations.

The effect of ethanol concentrations, anode electrocatalyst loading, cathode electrocatalyst loading and cell temperature were studied for the best electrocatalyst Pt-Ru-Re (1:1:0.5)/f-MWCNT and results are discussed in the subsequent section.

5.2.5.3 Effect of ethanol concentration

Fig (5.36) shows the effect of ethanol concentration on the polarization and power density curves using Pt-Ru-Re (1:1:0.5)/f-MWCNT as anode electrocatalyst and commercial Pt (40 wt. %)/C_{HiSPEC} as cathode electrocatalyst at a cell temperature of 30 °C. The electrocatalyst loading at anode and cathode were 1 mg/cm^2. It is seen from the Fig (5.36) that the cell performance increases with the increase ethanol concentration from 0.5 M to 2 M, while the cell performance decrease with further increase in ethanol concentration beyond 2 M. At very low ethanol concentration of 0.5 M, adequate fuel ethanol is not able to access the electrocatalyst layer to maintain the increased current density and thus the cell performance suddenly drops due to mass transport limitations. These results are consistent with the result reported by Song et al., (2005), Pramanik and Basu, (2007), Alzate et al., (2011) and Goel and Basu, (2012). The ethanol concentration of 2 M produces the maximum OCV of 0.708 V and the maximum power density of 9.52 mW/cm^2 at a current density of 38.4 mA/cm^2. At higher ethanol concentration of 3 M in results in low OCV of 0.658V and maximum power density of 8.65 mW/cm^2 at a current density of 36.8 mA/cm^2. The ethanol concentration of 0.5 M produced OCV of 0.704 V and maximum power density of 6.66 mW/cm^2 at a current density of 22.56 mA/cm^2. It is clearly seen that the maximum power density for 0.5 M and 3 M ethanol were lower than the 2 M ethanol concentration.

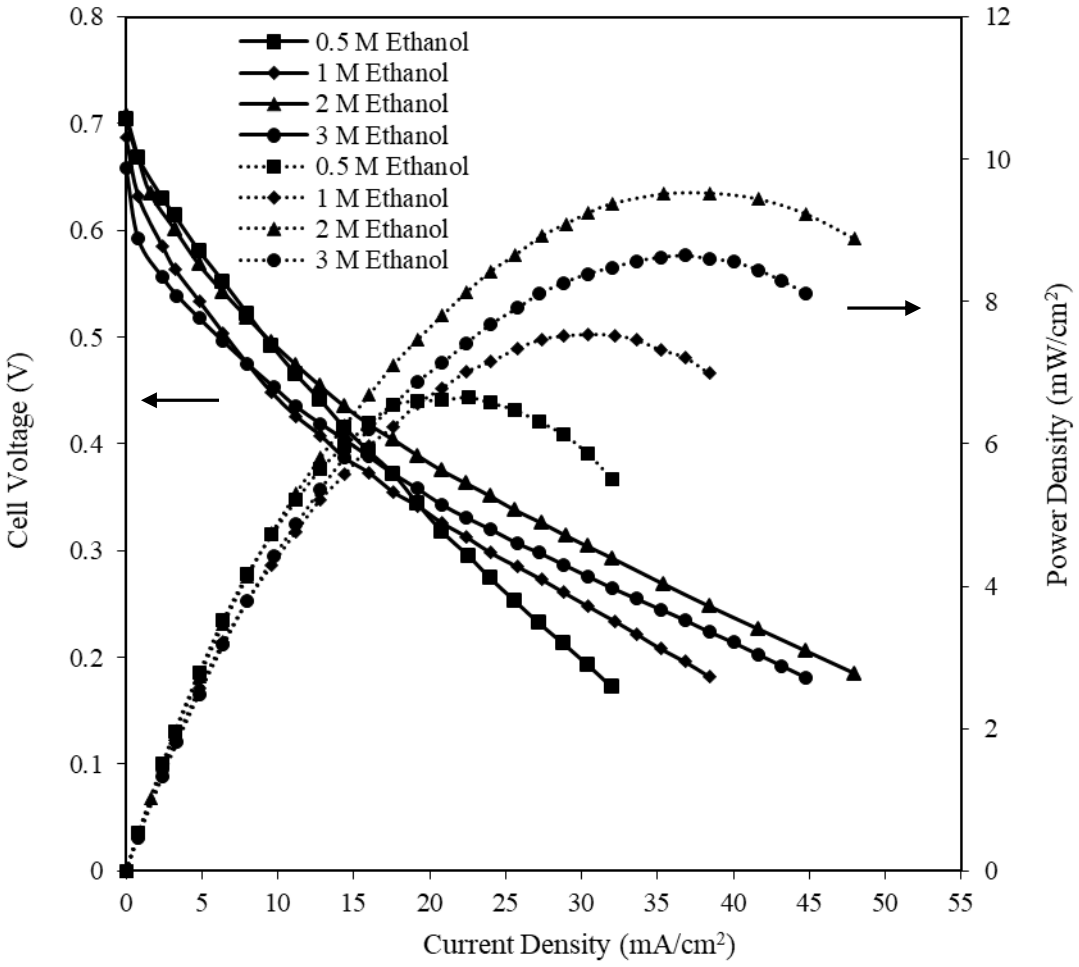

Figure 5.36 Single cell performance characteristics for anode electrocatalyst Pt-Ru-Re (1:1:0.5)/f-MWCNT using varying ethanol concentration as anode feed at a cell temperature of 30 °C. Cathode feed: pure humidified oxygen; $P_{cathode}$ = 1 bar (absolute); Dotted line-power density curves; Solid line- polarization curves.

The reason for the increase in cell performance with increase in ethanol concentration may be due to the replacement of water molecules from the active site of electrocatalyst offer by the ethanol molecules. As per Equation (5.6) presence of water and ethanol molecules both are very much essential for the completion of the reaction at the anode side.

$$C_2H_5OH + 3H_2O \rightarrow 2CO_2 + 12H^+ + 12e^- \quad (5.6)$$

Thus, a delicate balance is required between ethanol and water at the electrocatalyst sites. This is maintain at an ethanol concentration of 2 M and thus gives highest cell performance in terms of power density.

5.2.5.4 Effect of anode electrocatalyst loading

Fig (5.37) shows the effect of different anode loadings i.e., 0.5 mg/cm^2, 1 mg/cm^2 and 1.5 mg/cm^2 of Pt-Ru-Re (1:1:0.5)/f-MWCNT as an anode on the polarization and power density curves at a cell temperature of 30 °C. The cathode was kept fixed loading of 1 mg/cm^2 of commercial Pt (40 % wt.)/C_{HiSPEC}. The anode fuel was 2 M ethanol solution. It is seen in Fig (5.37) that the power density increases as electrocatalyst loading of the anode increase from 0.5 mg/cm^2 to 1 mg/cm^2. While, further increase in electrocatalyst loading beyond 1 mg/cm^2, the cell performance decreases. The reason for the reduction in power density of DEFC of anode loading at 1.5 mg/cm^2, may be attributed to electrocatalyst particle agglomeration/compaction in a limited space and an increase in electrode thickness as discussed in section 5.2.4.1 (Page no. 198) FESEM of anode (Pramanik et al., 2008).

The maximum OCV of 0.708 V and maximum power density of 9.52 mW/cm^2 at a current density of 38.4 mA/cm^2 were achieved for the synthesized Pt-Ru-Re (1:1:0.5)/f-MWCNT electrocatalyst. The electrocatalyst loading of 0.5 mg/cm^2 and 1.5 mg/cm^2 produced maximum power density of 6.30 mW/cm^2 at a current density of 25.6 mA/cm^2 and maximum power density 8.03 mW/cm^2 at a current density of 32 mA/cm^2, respectively. The maximum OCV of 0.686 V and 0.678 V were obtained for 0.5 mg/cm^2 and 1.5 mg/cm^2 loading of anode Pt-Ru-Re (1:1:0.5)/f-MWCNT, respectively.

The cathode loading was varied keeping anode loading fixed at optimum loading of 1 mg/cm^2. The effect of cathode loading is discussed in the next section.

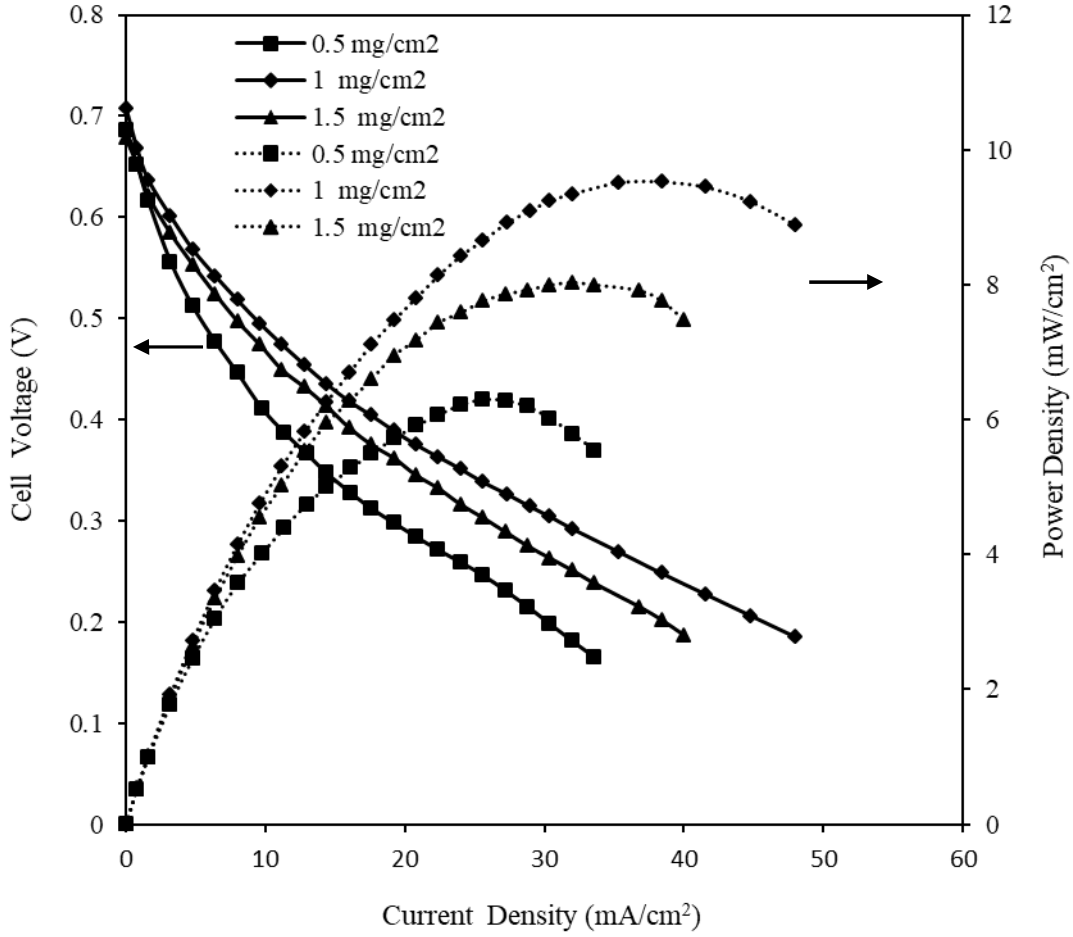

Figure 5.37 Single cell performance characteristics for anode electrocatalyst Pt-Ru-Re (1:1:0.5)/f-MWCNT at different electrocatalyst loading using an anode feed of 2 M ethanol solution. Cathode feed: pure humidified oxygen; $P_{cathode}$ = 1 bar (absolute); Dotted line-power density curves; Solid line- polarization curves.

5.2.5.5 Effect of cathode electrocatalyst loading

Fig (5.38) shows the effect of different cathode loadings i.e., 0.5 mg/cm^2, 1 mg/cm^2 and 1.5 mg/cm^2 of Pt/C_{HiSPEC} as cathode on the polarization and power density curves at a cell temperature of 30 °C. The anode was kept fixed at optimum loading of 1 mg/cm^2 of Pt-Ru-Re (1:1:0.5)/f-MWCNT. The anode fuel was 2 M ethanol solution. It is seen in Fig

(5.38) that the power density increases as electrocatalyst loading of the cathode increase from 0.5 mg/cm^2 to 1 mg/cm^2. While, further increase in electrocatalyst loading beyond 1 mg/cm^2, the cell performance decreases. The reason has already been discussed in the previous section for the varying anode electrocatalyst loading (Page no. 210) and in the section 5.2.4.2 FESEM of cathode (Page no. 201).

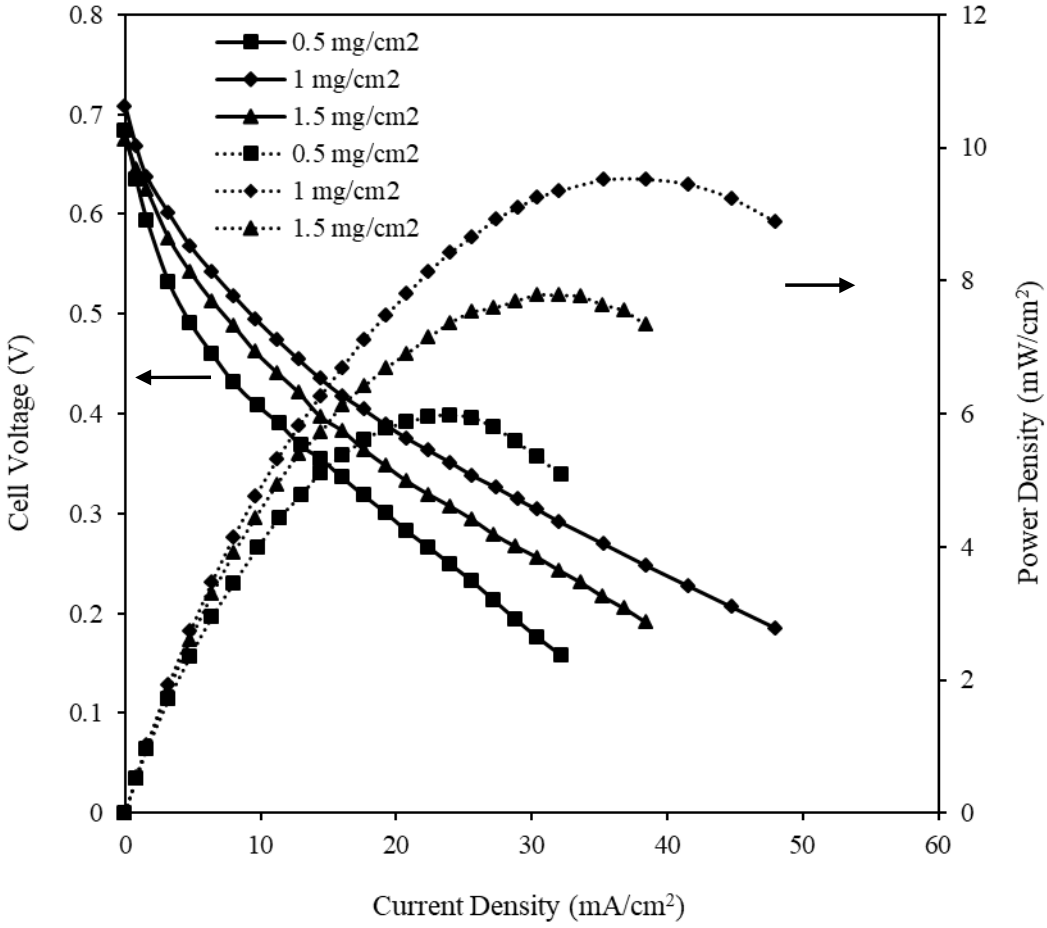

Figure 5.38 Single cell performance characteristics for commercial cathode electrocatalyst Pt/C_{HiSPEC} at different electrocatalyst loading using an anode feed of 2 M ethanol solution. Cathode feed: pure humidified oxygen; $P_{cathode}$ = 1 bar (absolute); Dotted line-power density curves; Solid line- polarization curves.

It is seen in Fig (5.38) that the maximum OCV of 0.708 V and maximum power density of 9.52 mW/cm^2 at a current density of 38.4 mA/cm^2 were obtained for synthesize Pt-Ru-

Re (1:1:0.5)/f-MWCNT electrocatalyst. While, the electrocatalyst loading of 0.5 mg/cm^2 and 1.5 mg/cm^2 of Pt/C_{HiSPEC} produced maximum power density of 5.98 mW/cm^2 at a current density of 24 mA/cm^2 and maximum power density of 7.78 mW/cm^2 at a current density of 30.4 mA/cm^2, respectively. The maximum OCV of 0.683 V and 0.674 V were obtained for 0.5 mg/cm^2 and 1.5 mg/cm^2 loading of commercial cathode Pt/C_{HiSPEC}, respectively. It is seen from Fig 5.38 that the cathode loading of 1 mg/cm^2 is the optimum and thus optimum cathode loading of 1 mg/cm^2 was used for the optimization of cell temperature in the next section (Page no. 213).

5.2.5.6 Effect of cell temperature on DEFC performance

Fig (5.39) shows the effect of temperature on the cell performance using Pt-Ru-Re (1:1:0.5)/f-MWCNT as anode electrocatalyst in DEFC, as it resulted in the best performance at room temperature of 30 °C. As mentioned earlier, the anode and cathode optimum loading of 1 mg/cm^2 were used for electrode fabrication. It is observed in Fig (5.39) that the polarization curve shifts upward with the increase in DEFC temperature up to 80 °C. The high temperature reduces the cell overpotentials mainly activation and ohmic losses (Alzate et al., 2011 and Choudhary and Pramanik, 2019). Moreover, the anode kinetics for ethanol electrooxidation gets enhanced at high temperatures and thus, current density also improves dramatically. It should be noted that maximum cell temperature was maintained at 80 ºC in the view of the boiling point of ethanol of about 78.4 ºC (Choudhary and Pramanik, 2020a and Choudhary and Pramanik, 2020b).

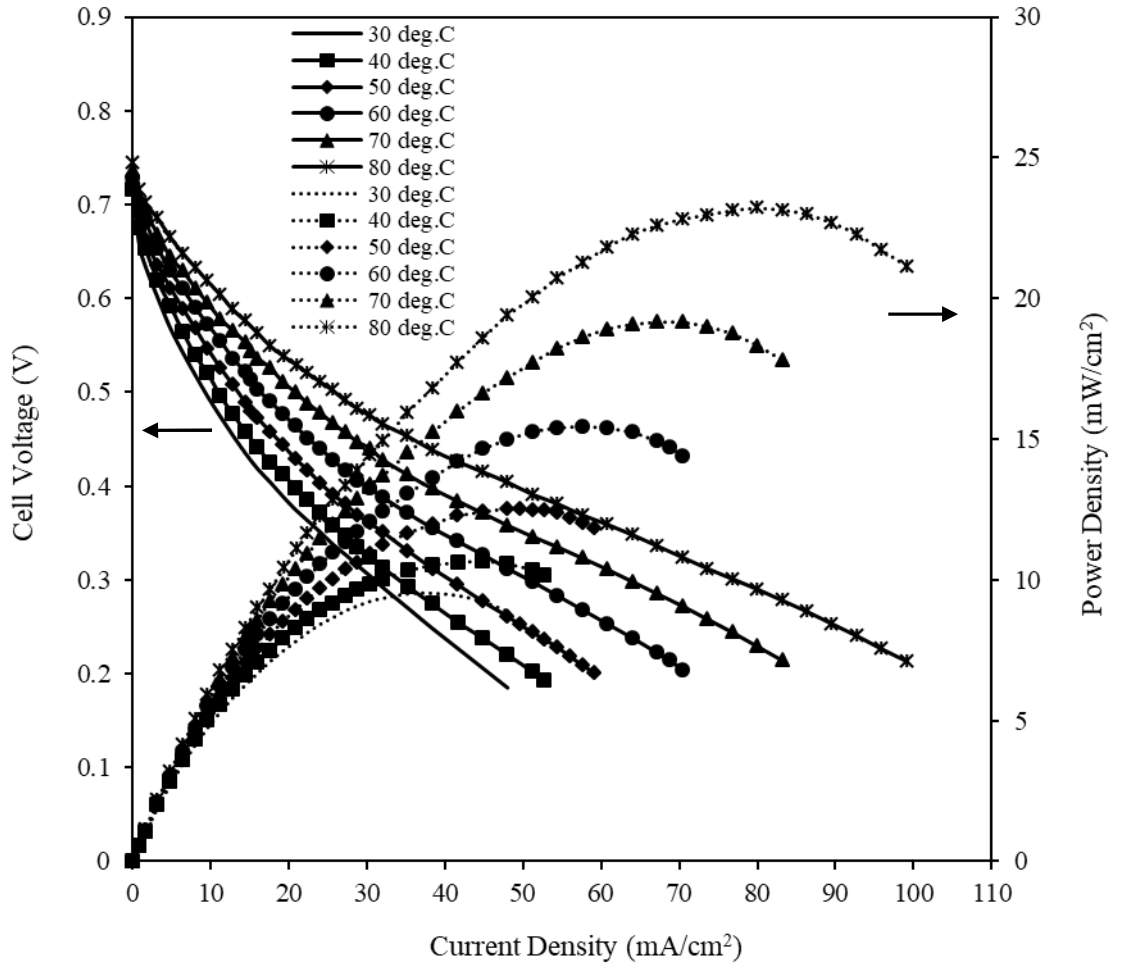

Figure 5.39 Single cell performance characteristics for anode electrocatalyst Pt-Ru-Re (1:1:0.5)/f-MWCNT at varying cell temperatures using an anode feed of 2 M ethanol solution. Cathode feed: pure humidified oxygen; $P_{cathode}$ = 1 bar (absolute); Dotted line- power density curves; Solid line- polarization curves.

The OCV, maximum power density, and current density at maximum power density at varying temperatures are presented in Table (5.21). The positive effects of temperature are also observed in OCV of the single DEFC, which could be explained by the Nernst equation (Larminie and Dicks, 2003). It is clearly observed that raising the temperature greatly enhanced DEFC cell performance, from maximum power density of 9.52 mW/cm^2 at 30 ºC to 23.2 mW/cm^2 at 80 ºC, i.e. about 2.44 times higher. These through study suggest that ethanol electrooxidation is difficult at low temperature generates very

low power density and thus, for practical application, the DEFC should be operated at high temperatures.

Table 5.21 Summary of performance of synthesized Pt-Ru-Re (1:1:0.5)/f-MWCNT electrocatalyst in single fuel cell tests for 2 M ethanol at various operating cell temperature.

Electrocatalysts	Temperature (°C)	Open circuit voltage (V)	Maximum power density (mW/cm^2)	Current density at maximum power density (mA/cm^2)
Pt-Ru-Re (1:1:0.5)/f-MWCNT	30	0.708	9.52	38.4
	40	0.716	10.66	44.8
	50	0.722	12.53	48
	60	0.728	15.44	57.6
	70	0.736	19.15	67.2
	80	0.744	23.2	80

5.2.6 Stability test of DEFC

The stability test is very important for evaluating the long term performance of the developed direct ethanol fuel cell. The stability test of single DEFC were performed using the best bi-metallic electrocatalysts i.e., Pt-Ru/C_{AB}-PLM (without post treated), Pt-Ru/C_{AB}-H_2-RT (with post treated), and best tri-metallic electrocatalyst Pt-Ru-Re (1:1:0.5)/f-MWCNT keeping cathode electrocatalyst same i.e., Pt/C_{HiSPEC} for all set of experiments.

The performances of synthesized electrocatalysts were compared with the available bi-metallic commercial electrocatalysts Pt-Ru/C. It is seen from the Fig (5.39) that the drop in cell voltage is lowest for the tri-metallic Pt-Ru-Re (1:1:0.5)/f-MWCNT even after 15 h of cell operation. The cell operating conditions were optimum as reported in section

5.1.1.5 (Page no. 143), section 5.1.2.3 (Page no. 168) and section 5.2.5 (Page no. 203), respectively. Fig (5.40) shows the data of stability tests recorded for 15 h at a constant load when drawing total current of 20 mA from the direct ethanol fuel cell (DEFC) using Pt-Ru/C_{AB}-PLM, Pt-Ru/C_{AB}-H_2-RT, commercial Pt-Ru/C and Pt-Ru-Re (1:1:0.5)/f-MWCNT as anode electrocatalysts. The solid electrolyte was Nafion® 117 commercial membrane. The humidified oxygen was used as an oxidant at the cathode.

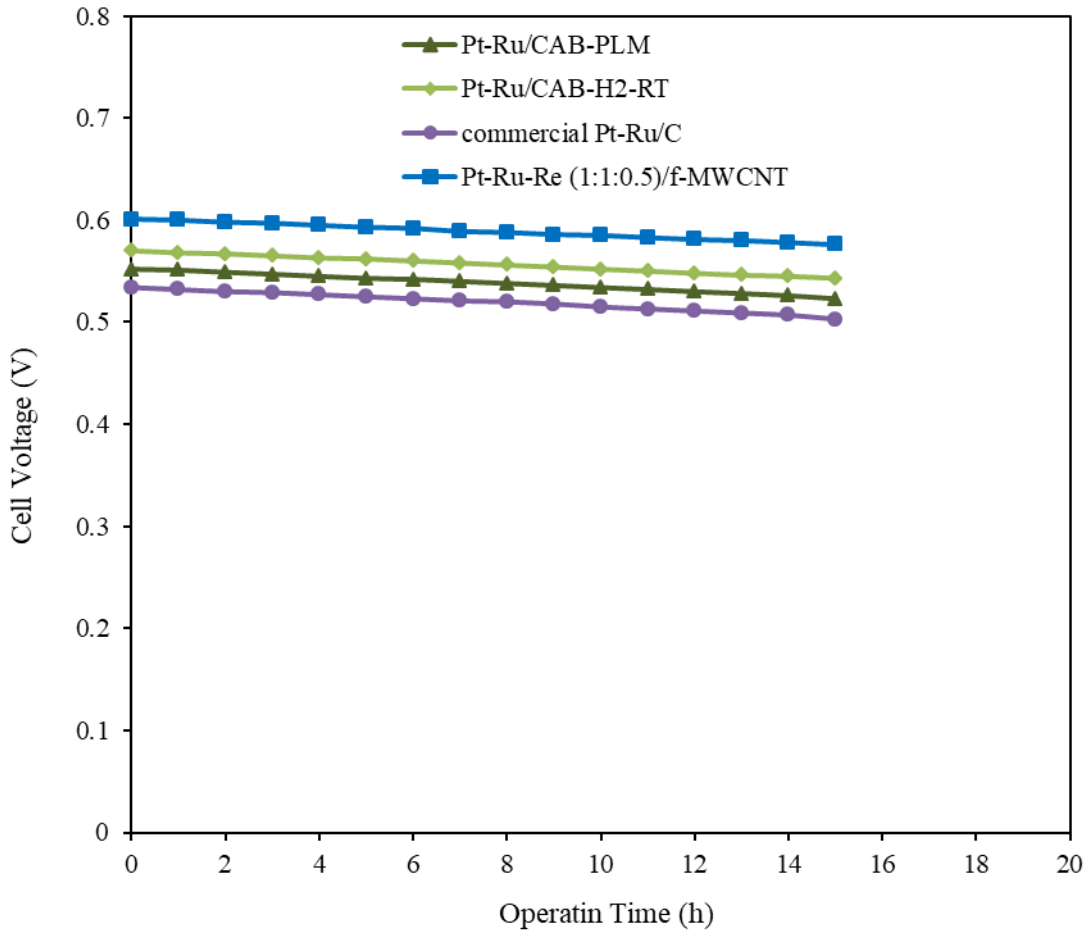

Figure 5.40 Stability test of the DEFC using synthesized bi-metallic Pt-Ru/C_{AB}-PLM (without post treated), Pt-Ru/C_{AB}-H_2-RT (with post treated), commercial Pt-Ru/C and tri-metallic Pt-Ru-Re (1:1:0.5)/f-MWCNT as anode electrocatalysts with 2 M ethanol at constant load of 20 mA at a temperature of 30 ^{o}C.

The cell voltage decreased slightly after 15 h of operation of DEFC from 0.601 V to 0.576 V, 0.57 V to 0.543 V, 0.552 V to 0.523 V and 0.534 V to 0.503 V for anode electrocatalysts Pt-Ru/C_{AB}-PLM, Pt-Ru/C_{AB}-H_2-RT, commercial Pt-Ru/C and Pt-Ru-Re (1:1:0.5)/f-MWCNT, respectively. The chemically synthesized electrocatalysts exhibited stable cell performance in terms of cell voltage for ethanol electrooxidation for the test period of 15 h. The DEFC fabricated with the Pt-Ru-Re (1:1:0.5)/f-MWCNT as anode showed relatively more stable cell voltage compared to the other bi-metallic electrocatalysts. The slight deterioration in cell performance with time may be because of the adsorption of intermediate species such as CO_x on the electrocatalyst surface formed during ethanol electrooxidation.

5.2.7 Comparison of the performance for synthesized and commercial electrocatalysts

Table (5.22) shows the performance comparison for the synthesized best anode bi-metallic electrocatalysts i.e., Pt-Ru/C_{AB}-PLM, Pt-Ru/C_{AB}-H_2-RT, commercial Pt-Ru/C (30%:15%) and tri-metallic Pt-Ru-Re (1:1:0.5)/f-MWCNT electrocatalysts of loading 1 mg/cm^2 for each electrode using ethanol as fuel. The commercial Pt/C_{HiSPEC} of 1 mg/cm^2 was used as cathode electrocatalyst. The solid electrolyte used was a commercial Nafion® 117 membrane. The cathode oxidant used was humidified oxygen. It is seen from Table (5.22) that the highest cell performance in terms of power density and current density is observed for the synthesized tri-metallic Pt-Ru-Re (1:1:0.5)/f-MWCNT electrocatalyst as anode in DEFC. Whereas, the maximum power density of commercial Pt-Ru/C (30%:15%) electrocatalyst was observed lower than all the synthesized bi-metallic and tri-metallic supported electrocatalysts. The maximum open circuit voltage (OCV) of 0.744 V and maximum power density of 23.2 mW/cm^2 at a current density of 80 mA/cm^2

were obtained for the tri-metallic Pt-Ru-Re (1:1:0.5)/f-MWCNT electrocatalyst as anode in DEFC at a temperature of 80 ºC.

Similarly, the single cell DEFC using bi-metallic Pt-Ru/C_{AB}-PLM and Pt-Ru/C_{AB}-H_2-RT as anode electrocatalysts produced maximum power density of 15.12 mW/cm^2 at a current density of 48.16 mA/cm^2 and 16.23 mW/cm^2 at a current density of 51.2 mA/cm^2, respectively. However, an OCV of 0.734 V and a maximum power density of 13.89 mW/cm^2 at a current density of 44.8 mA/cm^2 was obtained for commercial Pt-Ru/C (30%:15%) electrocatalyst as anode at a temperature of 80 ºC. It can be observed from Table (5.22) that the cell performance using synthesized bi-metallic Pt-Ru/C_{AB}-PLM and Pt-Ru/C_{AB}-H_2-RT were superior to that of commercial Pt-Ru/C (30%:15%) electrocatalyst.

Goel and Basu, (2014) reported an OCV of 0.61 V and a peak power density of 17.50 mW/cm^2 using Pt-Ru/C electrocatalyst with 2 mg/cm^2 electrocatalyst loading at 100 ºC. The peak power density is slightly higher than the present study bi-metallic electrocatalysts and it may be due to high cell temperature (100 ºC) and high loading of anode electrocatalyst (2 mg/cm^2). Tayal et al., (2012) obtained the maximum OCV of 0.64 V and a power density of 30.5 mW/cm^2 using the $Pt_{20}Re_5Sn_{15}$ (wt. %)/C as anode electrocatalyst at a cell temperature of 100 ºC. They used higher cell temperature (100 ºC) and high loading of both anode and cathode (2 mg/cm^2). Although cell performance was high, electrocatalyst loading at both anode and cathode were 2 mg /cm^2, respectively, which is higher than the present study. According to Tayal et al., (2011), the impregnation reduction technique synthesized anode electrocatalyst $Pt_{20}Sn_{20}$ (wt. %)/C produced a maximum OCV of 0.705 V and a power density of 22.4 mW/cm^2 at a cell temperature of 90 ºC with the same anode and cathode loading (1 mg/cm^2).

Table 5.22 Performance comparison of synthesized best bi-metallic and tri-metallic Pt-Ru/C_{AB}-PLM, Pt-Ru/C_{AB}-H_2-RT, commercial Pt-Ru/C (30%:15%) and tri-metallic Pt-Ru-Re (1:1:0.5)/f-MWCNT electrocatalysts as anode using optimum conditions.

References	**Electrolyte and electrocatalyst**	**Other operating conditions**	**Maximum power density (mW/cm^2)**	**OCV (V)**
Present Work	Nafion® 117; Anode: Pt-Ru/C_{AB}-PLM (40 wt. %) (1 mg/cm^2); Cathode: Pt/C (40 wt. %, AA**) (1 mg/cm^2)	Fuel: ethanol (2 M) (1.2 ml/min); Oxidant: humidified O_2 (60 ml/min); Temperature: 80 °C	15.12	0.736
Present Work	Nafion® 117; Anode: Pt-Ru/C_{AB}-H_2-RT (40 wt. %) (1 mg/cm^2); Cathode: Pt/C (40 wt. %, AA) (1 mg/cm^2)	Fuel: ethanol (2 M) (1.2 ml/min); Oxidant: humidified O_2 (60 ml/min); Temperature: 80 °C	16.23	0.737
Present Work	Nafion® 117; Anode: Pt-Ru (30%:15% by wt.)/C (1 mg/cm^2); Cathode: Pt/C (40 wt. %, AA) (1 mg/cm^2)	Fuel: ethanol (2 M) (1.2 ml/min); Oxidant: humidified O_2 (60 ml/min); Temperature: 80 °C	13.89	0.734
Present Work	Nafion® 117; Anode: Pt-Ru-Re (1:1:0.5)/f-MWCNT (40 wt. %) (1 mg/cm^2); Cathode: Pt/C (40 wt. %, AA) (1 mg/cm^2)	Fuel: ethanol (2 M) (1.2 ml/min); Oxidant: humidified O_2 (60 ml/min); Temperature: 80 °C	23.2	0.744
Goel and Basu, (2014)	Nafion® 117; Anode: Pt-Ru (1:1)/C (40 wt. %, 2.0 mg/cm^2); Cathode: Pt /C (40 wt. %, JM*) (1.0 mg/cm^2)	Fuel: ethanol (2 M) (1.0 ml/min); Oxidant: humidified (160 SCCM/min); Temperature: 100 °C	17.50	0.610
Tayal et al., (2012)	Nafion®117; Anode: $Pt_{20}Re_5Sn_{15}$ (wt.%)/C (40 wt. %) (2 mg/cm^2); Cathode: Pt /C (40 wt. %, JM) (2 mg/cm^2)	Fuel: ethanol (5 M) (1 ml/min); Oxidant: humidified O_2 (60 ml/min); Temperature: 100 °C	30.5	0.64
Tayal et al., (2011)	Nafion®117; Anode: $Pt_{20}Sn_{20}$ (wt.%)/C (40 wt. %) (1 mg/cm^2); Cathode: Pt /C (40 wt. %, JM) (1 mg/cm^2)	Fuel: ethanol (2 M) (1 ml/min); Oxidant: humidified O_2 (60 ml/min); Temperature: 90 °C	22.4	0.705

*JM-Johnson Matthey, **AA-Alfa Aesar.

In the present study synthesized Pt-Ru-Re (1:1:0.5)/f-MWCNT as anode electrocatalyst resulting in a maximum OCV of 0.744 V and a power density of 23.2 mW/cm^2 using anode and cathode electrocatalyst loading of 1 mg/cm^2 in both electrodes at a cell temperature of 80 ºC.

5.2.8 Efficiency of the direct ethanol fuel cell

The overall/total efficiency of a fuel cell is defined as the product of various individual efficiencies as described below (Carrette et al., 2001):

$$\eta_{FC,Overall} = \eta_r^{Cell} \times \eta_V \times \eta_F \times \eta_U \times \eta_H \quad (5.7)$$

Where $\eta_{FC,Overall}$ represents the overall efficiency of the fuel cell, while η_r^{Cell}, η_V, η_F, η_U and η_H are the thermodynamic efficiency/reversible cell efficiency, the electrochemical efficiency, the Faradaic efficiency, the fuel utilization efficiency and the heating value efficiency, respectively.

The thermodynamic efficiency or reversible cell efficiency (η_r^{Cell}) of a fuel cell is defined as the ratio of the Gibbs free energy change (ΔG) to the enthalpy change (ΔH), of the electrochemical reactions, and can be expressed as follows.

$$\eta_r^{Cell} = -\left(\frac{\Delta G}{\Delta H}\right) \quad (5.8)$$

The electrochemical efficiency (η_V) takes into account the losses resulted due to electrode overpotentials (activation and concentration overpotential) and the resistive losses (electrolyte, interconnects and contact resistances). It is defined as the ratio of the

operating cell potential under load to the reversible cell potential and can be expressed as below.

$$\eta_V = \left(\frac{E_{op}}{E_r^{\circ}} \right) \tag{5.9}$$

Faradaic efficiency or current efficiency (η_F) is expressed as the ratio of the actual number of electrons involved in the oxidation reaction (n_{actual}) to the theoretical maximum number of electrons involved in the complete fuel oxidation reaction (n_{theo}) as given below.

$$\eta_F = \left(\frac{n_{actual}}{n_{theo}} \right) \tag{5.10}$$

The fuel utilization efficiency (η_U) is defined as the actual fuel reacted to the fuel supplied to the fuel cell on a mass basis. Since all the fuel is not consumed in the reaction. Some fuel has to pass through unreacted. Its value is assumed to be 0.95 (Larminie and Dicks, 2003).

The heating value efficiency is defined as the ratio of the heating value of all fuel components that are converted electrochemically to the heating value of fuel supplied in the fuel stream (Carrette et al., 2001). Heating value efficiency is neglected in the present work because the fuel is in pure form. Thus, after considering all the assumptions the final form of the Equation (5.7) is written as:

$$\eta_{FC,Overall} = \eta_r^{Cell} \times \eta_V \times \eta_F \times \eta_U \tag{5.11}$$

The DEFC efficiencies for the synthesized best anode bi-metallic e.g., Pt-Ru/C_{AB}-PLM, Pt-Ru/C_{AB}-H_2-RT and commercial Pt-Ru/C and tri-metallic Pt-Ru-Re (1:1:0.5)/f-

MWCNT were calculated at room temperature using Equation (5.11). The cathode electrocatalyst of commercial Pt (40 wt. %)/C_{HiSPEC} was used for all experiments.

The maximum power density conditions have already been mentioned for the synthesized best anode bi-metallic e.g., Pt-Ru/C_{AB}-PLM (8.28 mW/cm^2 at a current density of 27.36 mA/cm^2) (Page no. 146, Fig. 5.14), Pt-Ru/C_{AB}-H_2-RT (9.15 mW/cm^2 at a current density of 32 mA/cm^2) (Page no. 170, Fig. 5.22) and commercial Pt-Ru/C (7.14 mW/cm^2 at a current density of 25.6 mA/cm^2) (Section: APPENDIX C, Page no. 280, Fig. C.2) and tri-metallic Pt-Ru-Re (1:1:0.5)/f-MWCNT (9.52 mW/cm^2 at a current density of 38.40 mA/cm^2) (Page no. 208, Fig. 5.36). The calculated operating cell voltages are 0.303 V, 0.286 V, 0.279 V and 0.248 V for the anode electrocatalysts Pt-Ru/C_{AB}-PLM, Pt-Ru/C_{AB}-H_2-RT and commercial Pt-Ru/C and tri-metallic Pt-Ru-Re (1:1:0.5)/f-MWCNT, respectively. Table (5.23) shows the individuals and overall efficiency for ethanol fuel using bi-metallic Pt-Ru/C_{AB}-PLM, Pt-Ru/C_{AB}-H_2-RT and commercial Pt-Ru/C and tri-metallic Pt-Ru-Re (1:1:0.5)/f-MWCNT as anode electrocatalysts for DEFC. The overall efficiencies of 16.05 %, 15.43% and 14.82 % were obtained for the best bi-metallic Pt-Ru/C_{AB}-PLM, Pt-Ru/C_{AB}-H_2-RT and commercial Pt-Ru/C as anode electrocatalysts, respectively for ethanol fuel at a temperature of 30 ^oC. The overall efficiency of 13.44 % was obtained for Pt-Ru-Re (1:1:0.5)/f-MWCNT electrocatalyst, which is little bit lower than the bi-metallic electrocatalysts. The reason may be due low operating cell temperature of 30 °C.

Table 5.23 Individual efficiencies for ethanol fuel used in direct ethanol fuel cell using best bi-metallic Pt-Ru/C_{AB}-PLM, Pt-Ru/C_{AB}-H_2-RT and commercial Pt-Ru/C and tri-metallic Pt-Ru-Re (1:1:0.5)/f-MWCNT as anode electrocatalysts at room temperature.

Anode Electrocatalysts	η_r^{Cell}	η_V	η_F	η_U	**Total Efficiency (%)**
Pt-Ru/C_{AB}-PLM (35 ºC)	0.97	0.26	0.67	0.95	16.05
Pt-Ru/C_{AB}-H_2-RT (40 ºC)	0.97	0.25	0.67	0.95	15.43
Commercial Pt-Ru/C (35 ºC)	0.97	0.24	0.67	0.95	14.82
Pt-Ru-Re (1:1:0.5)/f-MWCNT (30 ºC)	0.96	0.22	0.67	0.95	13.44

5.3 Optimization and validation of process parameters using RSM: Part III

5.3.1 Statistical analysis and model development

The set of proposed tests and experimental results for the maximum power density, based on the BBD method, are presented in Table (5.24).

Table 5.24 Box-Behnken design (BBD) matrix for three independent variables with response values, i.e. the DEFC power density.

Run	A-Ethanol concentration (M)	B-Anode electrocatalyst loading (mg/cm^2)	C-Cell temperature (^oC)	Power density (mW/cm^2)	
				Experimental value	Predicted value
1	2	1.00	60	15.44	15.47
2	2	1.00	60	15.85	15.47
3	3	1.00	80	21.80	21.51
4	1	0.5	60	7.8	7.48
5	3	1	40	9.98	10.15
6	3	1.5	60	13.2	13.52
7	1	1	80	18.3	18.13
8	2	1.5	40	9.8	9.31
9	2	0.5	40	7.5	7.54
10	2	1.5	80	21.6	21.57
11	1	1	40	8.7	8.99
12	2	0.5	80	15.3	15.79
13	2	1	60	15.70	15.47
14	2	1	60	15.2	15.47
15	3	0.5	60	10.2	10.0
16	2	1	60	15.15	15.47
17	1	1.5	60	11.3	11.50

It can be seen from the last two-column of Table (5.24) that the experimentally calculated actual values of power density are closer to the predicted values obtained from the model which approves the reliability of the RSM model. The highest power density of 21.80 mW/cm^2 was obtained when the DEFC was operated with an ethanol concentration of 3 M, anode electrocatalyst loading of 1 mg/cm^2 and operating cell temperature of 80 ºC. However, the lowest cell performance in terms of power density 7.5 mW/cm^2 was achieved at an ethanol concentration of 2 M, anode electrocatalyst loading of 0.5 mg/cm^2 and operating cell temperature of 40 ºC.

Table (5.25) shows the comparison of four response models i.e., linear, two factor interaction (2FI), quadratic and cubic summary statistics, which focuses on maximizing the adjusted and predicted R^2. Among the four response models, the quadratic model is selected on the basis of the maximum adjusted and predicted R^2 values as presented in Table (5.25). Moreover, the predicted residual error sum of squares (PRESS) value of the quadratic model is also smaller than that of the other response model, which implies how fine the model fits the data (Panjiara and Pramanik, 2020b).

Table 5.25 Comparison of the ANOVA model results for ethanol concentration, anode electrocatalyst loading and cell temperature.

Source	**Std Dev.**	**R^2**	**Adjusted R^2**	**Predicted R^2**	**PRESS values**
Linear	2.22	0.7952	0.7479	0.6208	118.80
2FI	2.43	0.8121	0.6994	0.2404	237.97
Quadratic	0.44	0.9956	0.9900	0.9474	16.49
Cubic	0.31	0.9988	0.9952	Aliased	Aliased

The ANOVA statistics of the quadratic model are presented in Table (5.26). The significance of each independent variable to the response is evaluated on the basis of the value of two parameters i.e., F-value and p-value. The ANOVA (Table 5.26) was implemented to verify the statistical significance of the regression model, model coefficient and lack of fit (Charoen et al., 2017). The quadratic model is chosen because of the high F value (177.40) and the lower p-value of the model than 0.0001. In addition, the difference between the adjusted R^2 and the predicted R^2 for the quadratic model is less than 0.2. The p-value < 0.05 and the higher F value indicate the suitability of the model (Charoen et al., 2017). For the present model, the "F-value" of the 177.40 with a very low "p-value" (< 0.0001) suggests that the developed model is well applicable to the experiments (Table 5.26). The variance analysis of Table (5.26) showed that the values of R^2 and adjusted R^2 were estimated at 0.9956 and 0.9900, respectively. The model with a small standard deviation (0.44) and a regression coefficient R^2 (0.9956) closer to the unity, indicates that the predicted power density values were accurate and close to the experimental data (Zainoodin et al., 2015). Besides, the R^2 value of 0.9956 shows that 99.56 % of the total power density variation is attributed to the experimental variables and exhibits a high correlation between the experimental data and the model predicted ones. The predicted R^2 of 0.9474 is in reasonable agreement with the adjusted R^2 of 0.9900. Herein, "Adeq Precision" measures the ratio of signal to noise and a value greater than 4 is a general requirement. In the present study, the value of 41,556 "Adeq Precision" indicates adequate precision. In addition, the lower coefficient of variation (CV % = 3.23) attests to the reliability of the experimental design with higher precision. Besides, the p-value of the "lack of fit" is equal to 0.1264 (Table 5.26), which is a higher significance level value ($\alpha = 0.05$). Thus, the "lack of fit" is not significant for the power density of the DEFC, which implies the conformity of the model presented.

Table 5.26 ANOVA results of the quadratic model for the response.

Source	Sum of squares	Degree of freedom	Mean square	F-value	p-value (Prob > F)	Remark
Model	311.93	9	34.66	177.40	< 0.0001	Significant
A-Ethanol concentration	10.31	1	10.31	52.75	0.0002	
B- Anode electrocatalyst loading	28.50	1	28.50	145.88	< 0.0001	
C- Cell temperature	210.33	1	210.33	1076.58	< 0.0001	
AB	0.063	1	0.063	0.32	0.5893	
AC	1.23	1	1.23	6.31	0.0403	
BC	4.00	1	4.00	20.47	0.0027	
A^2	14.39	1	14.39	73.68	< 0.0001	
B^2	37.74	1	37.74	193.19	< 0.0001	
C^2	4.87	1	4.87	24.95	0.0016	
Residual	1.37	7	0.20			
Lack of fit	0.99	3	0.33	3.55	0.1264	Not significant
Pure Error	0.37	4	0.093			
Correlation Total	313.30	16				
Std. Dev.	**0.44**					
Mean	**13.70**					
CV%	**3.23**					
R^2	**0.9956**					
Adjusted R^2	**0.9900**					
Predicted R^2	**0.9474**					
Adeq. Precision	**41.556**					

Besides, the p-values for linear terms (A, B and C) were less than 0.05, indicating the benchmark impact of these variables on power density. The p-value of interaction terms (AC, BC) was less than the significance level ($\alpha = 0.05$), showing the interactive

influence of these parameters on power density. In contrast, the p-value of the interaction effect of AB ($p = 0.5893$) was higher than the significant level ($\alpha = 0.05$). The p-values < 0.05 for all quadratic terms (A^2, B^2 and C^2) showed that a curved line appears to follow the relationship between each variable and the power density. In the regression models, the F-values of significant terms A, B and C are 52.75, 145.88 and 1076.58, respectively. The influence of the three factors on the response i.e., the power density of a DEFC are: C > B > A, and the influence of the interaction terms are: BC > AC > AB.

According to these results, the quadratic regression model equation in terms of coded parameters, which relates to dependent variables and independent variables and could be used to estimate the maximum power density of the DEFC, is illustrated by Equation (5.12).

$$\text{Power Density } (Y) = 15.47 + 1.14A + 1.89B + 5.13C - 0.12AB + 0.55\ AC + 1.00BC - 1.85A^2 - 2.99B^2 + 1.08C^2 \quad (5.12)$$

Where A, B, and C are the coded terms for the three independent test variables i.e., ethanol concentration, electrocatalyst loading, and operating cell temperature, respectively. A positive sign before the term in Equation (5.12), suggests that the term effect favors the response, while a negative sign indicates an antagonistic effect on the response i.e., power density. The positive coefficient values of the terms A, B, C, AC, BC and C^2 have a positive impact on the response value, as seen in Equation (5.12). However, the binary interaction of AB and the quadratic terms A^2 and B^2 have a negative effect on the power density of DEFC. The predicted power density values as responses using Equation (5.12) were also presented in Table (5.24).

The relationship between the experimental and the predicted power density (response) values of the DEFC is indicated in Fig (5.41). It is seen from Fig (5.41) that the experimental results (point) have been found closer to the RSM based model predicted results (line). The value at each power density point is represented in different colors. Red color, for example, represents the highest power density down to blue which represents the minimum power density (Charoen et al., 2017). Fig (5.41) also reveals that all the points lie in the vicinity of a straight line. For the current model, the value of the correlation coefficient (R^2) for the DEFC power density is 0.9956, indicating an efficient consistency between the RSM based predicted results and the experimental ones.

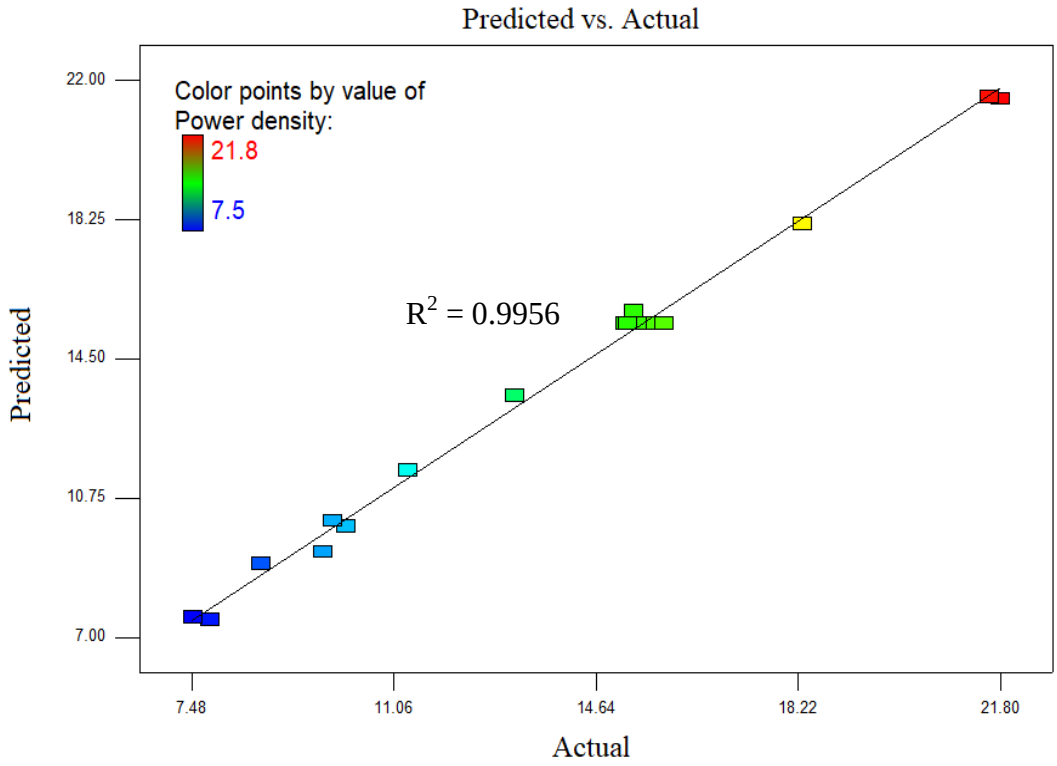

Figure 5.41 Response surface plot of the model predicted versus actual power density of DEFC.

The plot of residuals versus predicted power density values (Fig 5.42) shows the predictive accuracy of the model. Studentized residues are randomly scattered on the

display indicating that the constant range of residuals across the graph and no single residual value being examined stands out from the x-axis red line (greater than +3 or less than −3). Each residual value point fluctuates slightly over the x-axis and confirms the assumptions of constant variance. It can be noted that the model and experiment findings have been considered satisfactory.

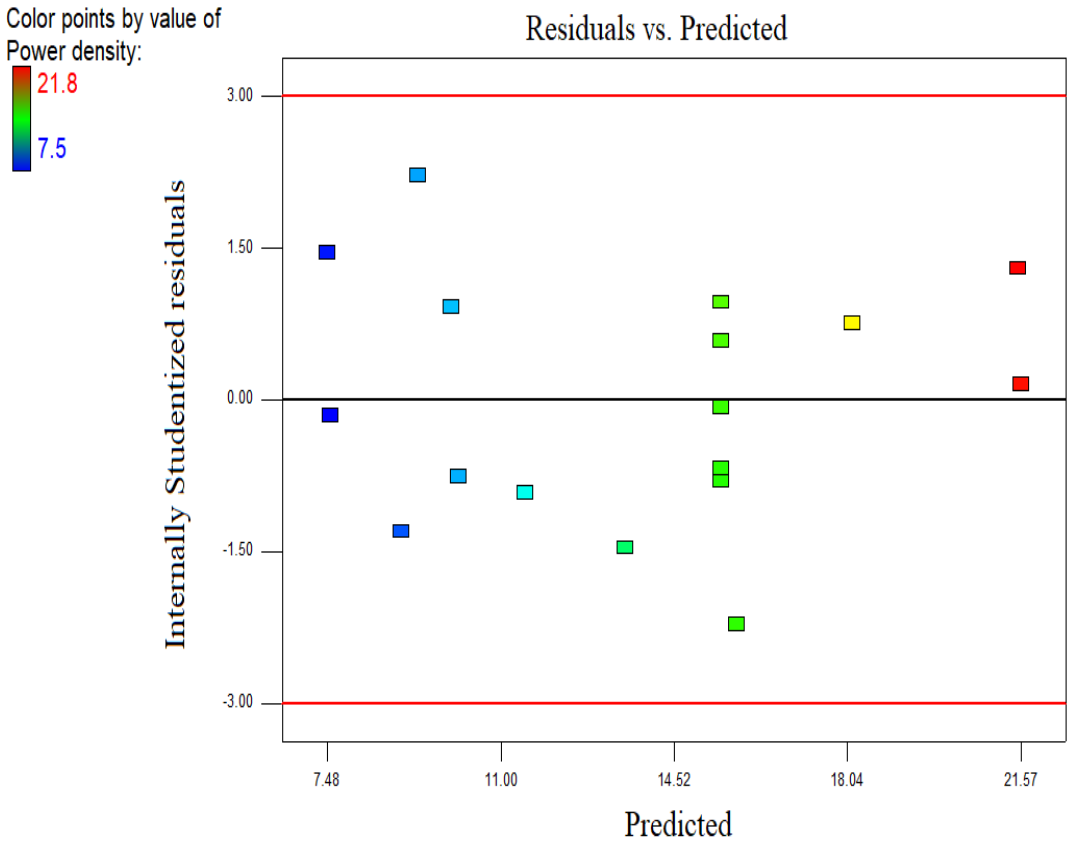

Figure 5.42 Response surface plot of the residuals versus model predicted power density of DEFC.

5.3.2 Effect of ethanol concentration

Fig (5.43a) and Fig (5.43b) represent the two-dimensional (2D) contour plot and three-dimensional (3D) response surface to illustrate the effect of ethanol concentration and electrocatalyst loading on the power density at an operating temperature of 79.48 ºC. At

the same loading of electrocatalysts, increasing the concentration of ethanol from 1 to 3 M, the peak power density is experiencing a rising trend, reaching the peak point and then falling. The power density was first observed to increase as ethanol concentration and electrocatalyst loading increased to a certain point, and then began to decrease with further increase in ethanol concentration and electrocatalyst loading. The optimum conditions resulting in the highest power density are set in the circular region. In addition, the change in color from blue to red represents higher response values. A high ethanol concentration gradient (greater than 2 M) results in a faster and more fuel ethanol crossover through the membrane on the cathode side.

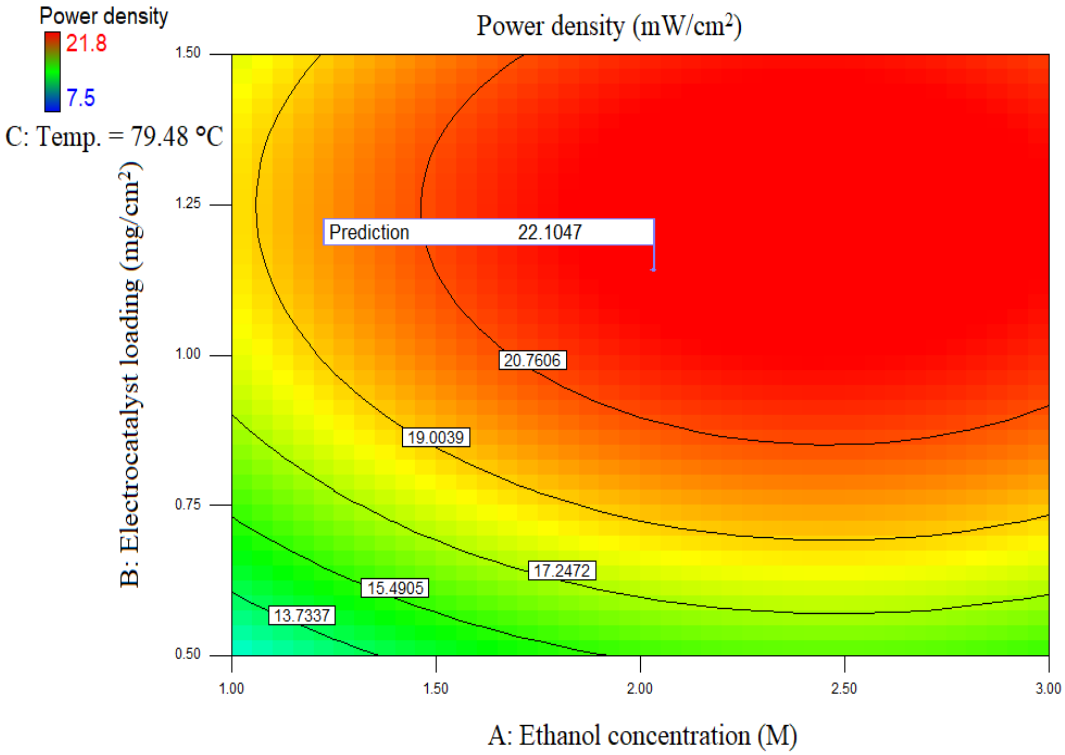

Figure 5.43a Two-dimensional contour plot showing the effect of ethanol concentration, anode electrocatalyst loading and their mutual interaction on the power density at an operating temperature of 79.48 ° C.

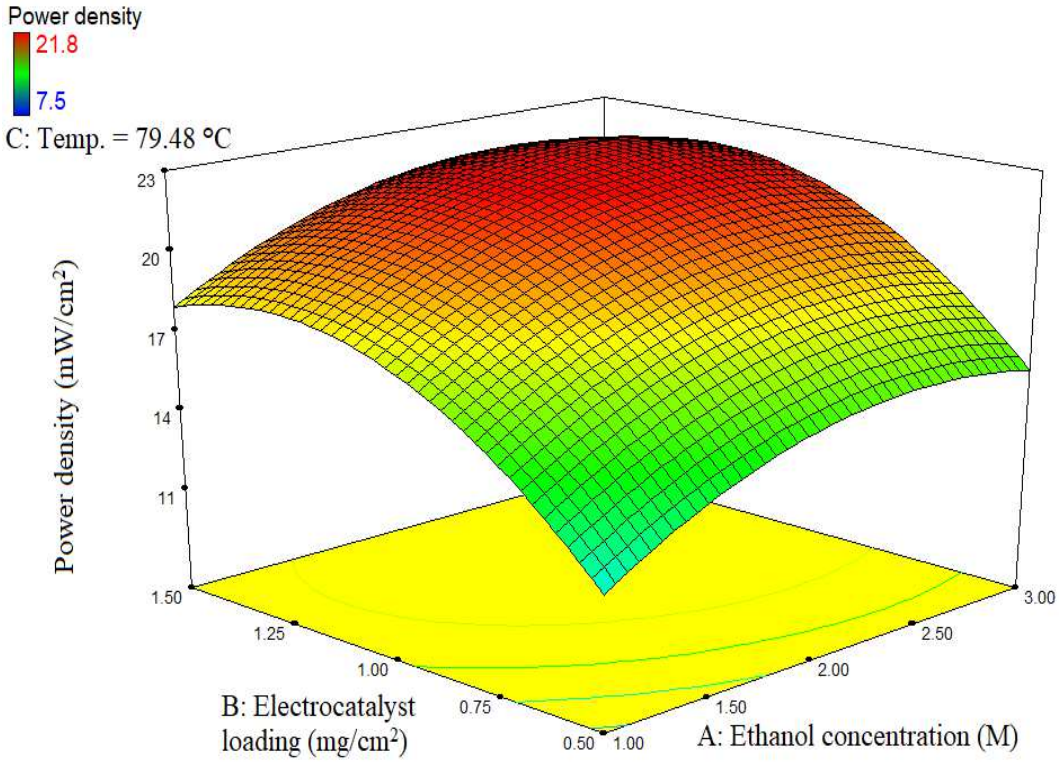

Figure 5.43b Three-dimensional response plot showing the effect of ethanol concentration, anode electrocatalyst loading and their mutual interaction on the power density at an operating temperature of 79.48 ° C.

The cross ethanol fuel through the polymer membrane results in a mixed potential and electrocatalyst poisoning of the cathode (Pramanik and Basu, 2007, Alzate et al., 2011 and Charoen et al., 2017). This results in a decrease in cell voltage and a significant reduction in power density. It was observed that not only the concentration of ethanol but also the loading of electrocatalysts had a significant influence on the power density of DEFC.

5.3.3 Effect of operating cell temperature

Fig (5.44a) and Fig (5.44b) depicts the two-dimensional (2D) contour plot and three-dimensional (3D) response surface to explain the maximum power density as a function

of operating temperature and ethanol concentration at a constant anode electrocatalyst loading of 1.14 mg/cm^2 for DEFC. Considering the same concentration of ethanol, it is seen that the maximum power density increases significantly as the operating temperature rises from 40 ºC to 80 ºC. It has been consistent with research by Charoen et al., (2017), Pramanik and Basu, (2007), Song et al., (2005) and Alzate et al., (2011). Improved performance of DEFC is mainly due to accelerated electrode reaction kinetics of both ethanol electrooxidation at the anode and oxygen electro-reduction at the cathode according to the Arrhenius equation **(**Charoen et al., 2017).

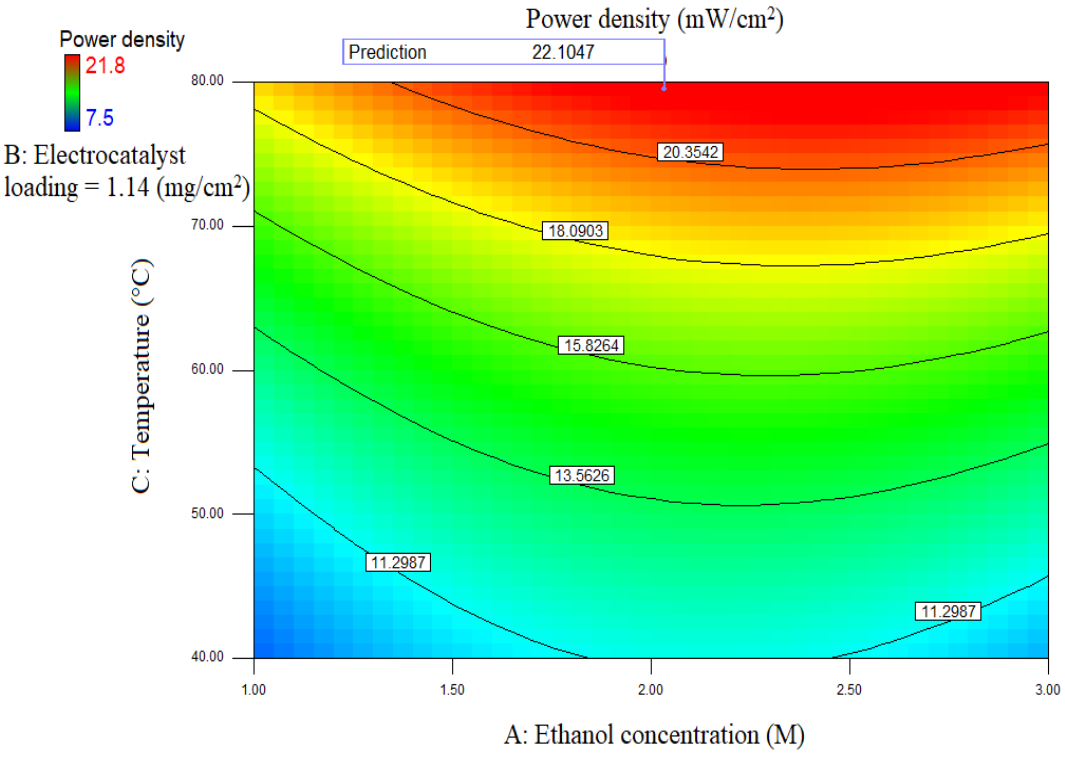

Figure 5.44a Two-dimensional contour plot showing the effect of operating temperature, ethanol concentration and their mutual interaction on the power density at an electrocatalyst loading of 1.14 mg/cm^2.

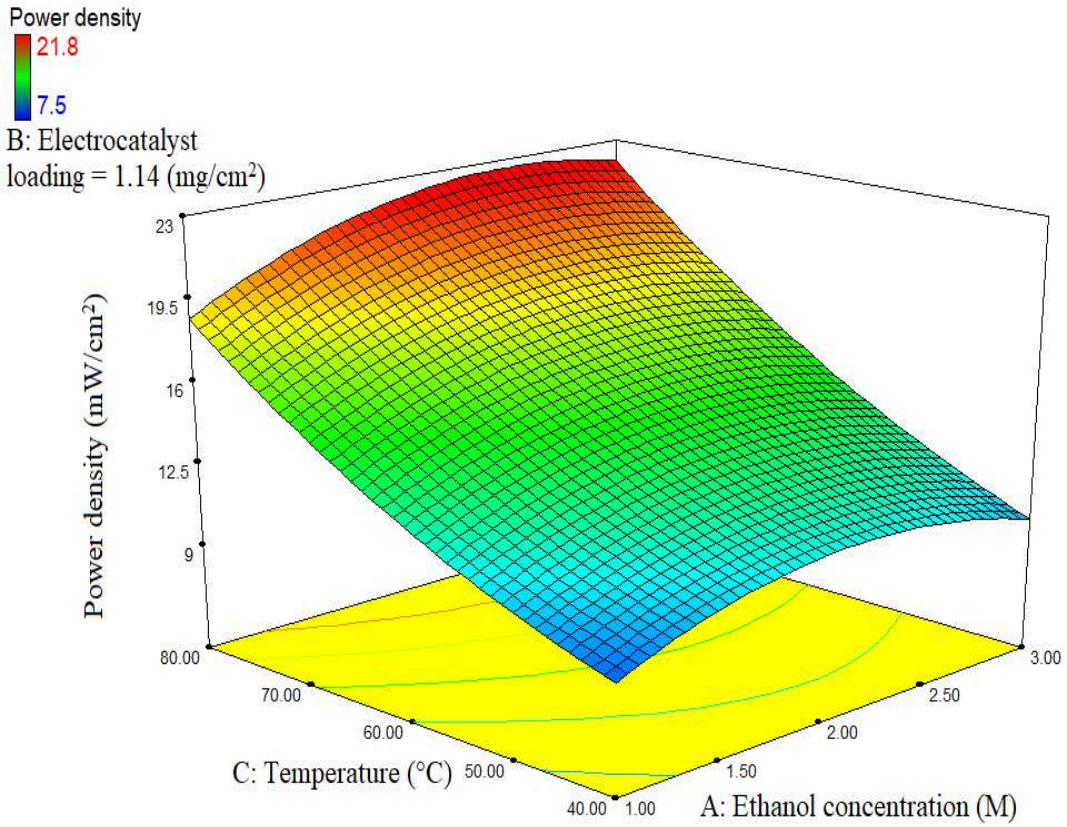

Figure 5.44b Three-dimensional response plot showing the effect of operating temperature, ethanol concentration and their mutual interaction on the power density at an electrocatalyst loading of 1.14 mg/cm^2.

In addition, the higher cell operating temperature increases the proton conductivity of the Nafion® membrane and Nafion® ionomer in the electrocatalyst layers and thus increases the amount of H^+ (proton) traveling through the membrane (Choudhary and Pramanik, 2019, Song et al., 2005 and Heysiattalab et al., 2011). On the other hand, the Nafion® membrane had a high degree of swelling at elevated operating temperature and a higher ethanol concentration, resulting in severe ethanol crossover through the polymeric membrane. The higher temperature causes the expansion of the polymer backbone of the Nafion® membrane due to the softening of the fluorinated chain. As a result, fuel loss on the anode side and cross fuel on the cathode creates a mixed potential that reduces overall efficiency. Thus, the power density decreases slightly at a high ethanol concentration. It

can be seen from Fig (5.44a) and Fig (5.44b) that the maximum power density of DEFC was significantly affected by the operating cell temperature and ethanol concentrations.

5.3.4 Effect of electrocatalyst loading at the anode electrode

Fig (5.45a) and Fig (5.45b) shows the two-dimensional (2D) contour plot and three-dimensional (3D) response surface plot to explain the effect of electrocatalyst loading and operating temperature on the power density of DEFC at an ethanol concentration of 2.03 M. With regard to the same operating temperature, it is evident that the power density increases as electrocatalyst loading of the anode increase from 0.5 mg/cm^2 to 1.14 mg/cm^2.

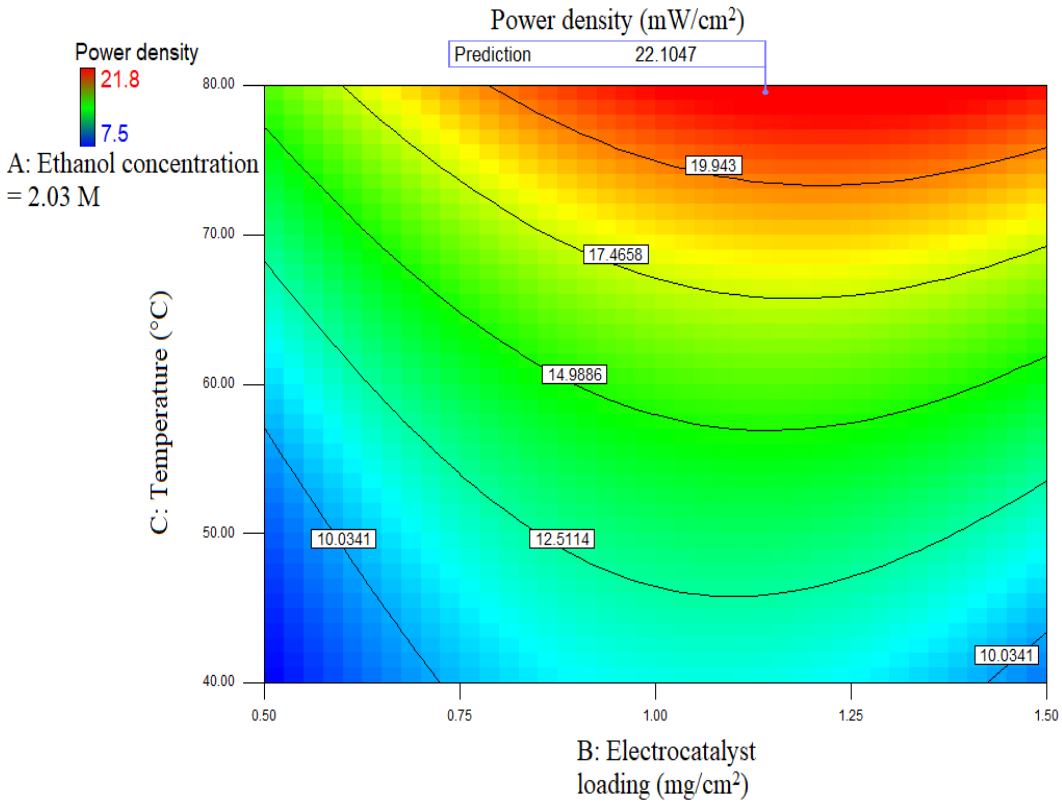

Figure 5.45a Two-dimensional contour plot showing the effect of electrocatalyst loading, operating temperature and their mutual interaction on the power density at an ethanol concentration of 2.03 M.

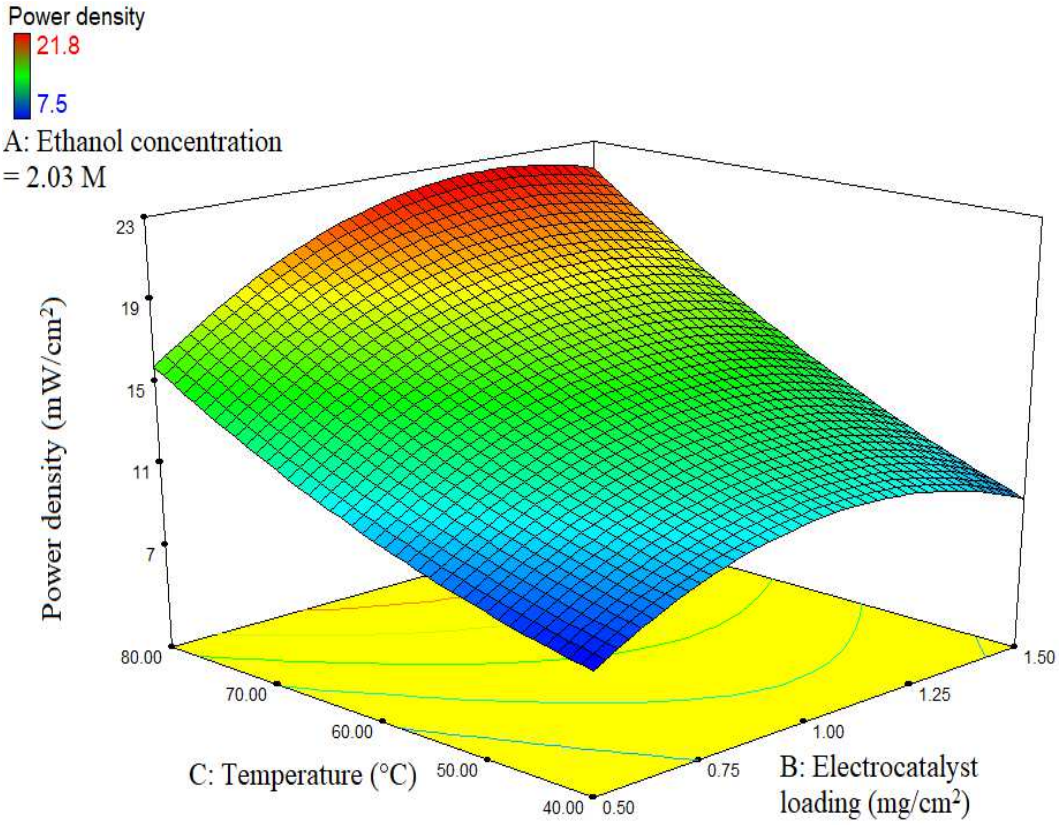

Figure 5.45b Three-dimensional response plot showing the effect of electrocatalyst loading, operating temperature and their mutual interaction on the power density at an ethanol concentration of 2.03 M.

However, a further increase in the electrocatalyst loading power density begins to decrease. The reason for the reduction in power density of DEFC of anode loading at 1.5 mg/cm^2 can be attributed to electrocatalyst particle agglomeration/compaction in a limited space and an increase in electrode thickness. This results in a decrease in the active electrocatalyst sites per unit area and the porosity of the electrode catalyst layer (Pramanik and Basu, 2007 and Panjiara and Pramanik, 2020a). As a result, the mass transfer resistance to the diffusion of ethanol from the bulk phase to the active electrocatalyst layer is increased. It could be seen from Fig (5.45a) and Fig (5.45b) that the operating temperature has a greater effect on the response (power density) than electrocatalyst loading at the anode.

5.3.5 Verification of the model

The research is conducted to optimize the operating conditions of DEFC such as concentration of ethanol, anode electrocatalyst loading and operating temperature. The objective is to maximize the power density of DEFC. The optimum parameters are obtained for the maximum power density of DEFC by RSM Design – Expert 7.0 is shown in Fig (5.46). Optimum conditions of DEFC resulted in a maximum power density of 22.10 mW/cm^2 at an ethanol concentration of 2.03 M, an electrocatalyst anode loading of 1.14 mg/cm^2 and an operating temperature of 79.48 °C (Table 5.27).

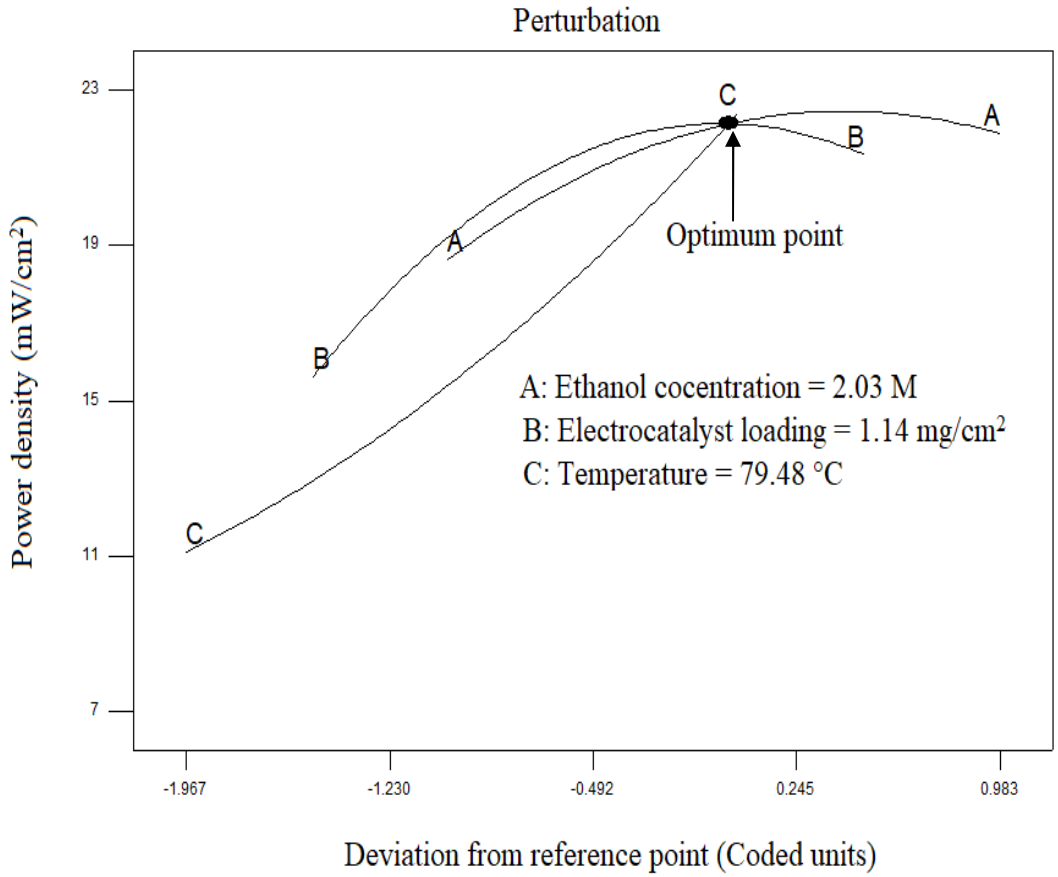

Figure 5.46 Optimum point detection for the maximum power density of DEFC from the perturbation curve.

In order to verify the predicted optimum results of the model, three new confirmation experiments under suggested optimal conditions were carried out with the same DEFC set-up and the results are shown in Fig (5.47) and Table (5.27). The difference in maximum power density was a 2.58 % error between the predicted model and the experimental values. Such an error is within an acceptable range of 5 % and confirms that the predicted model is sufficiently accurate within the 95 % prediction interval.

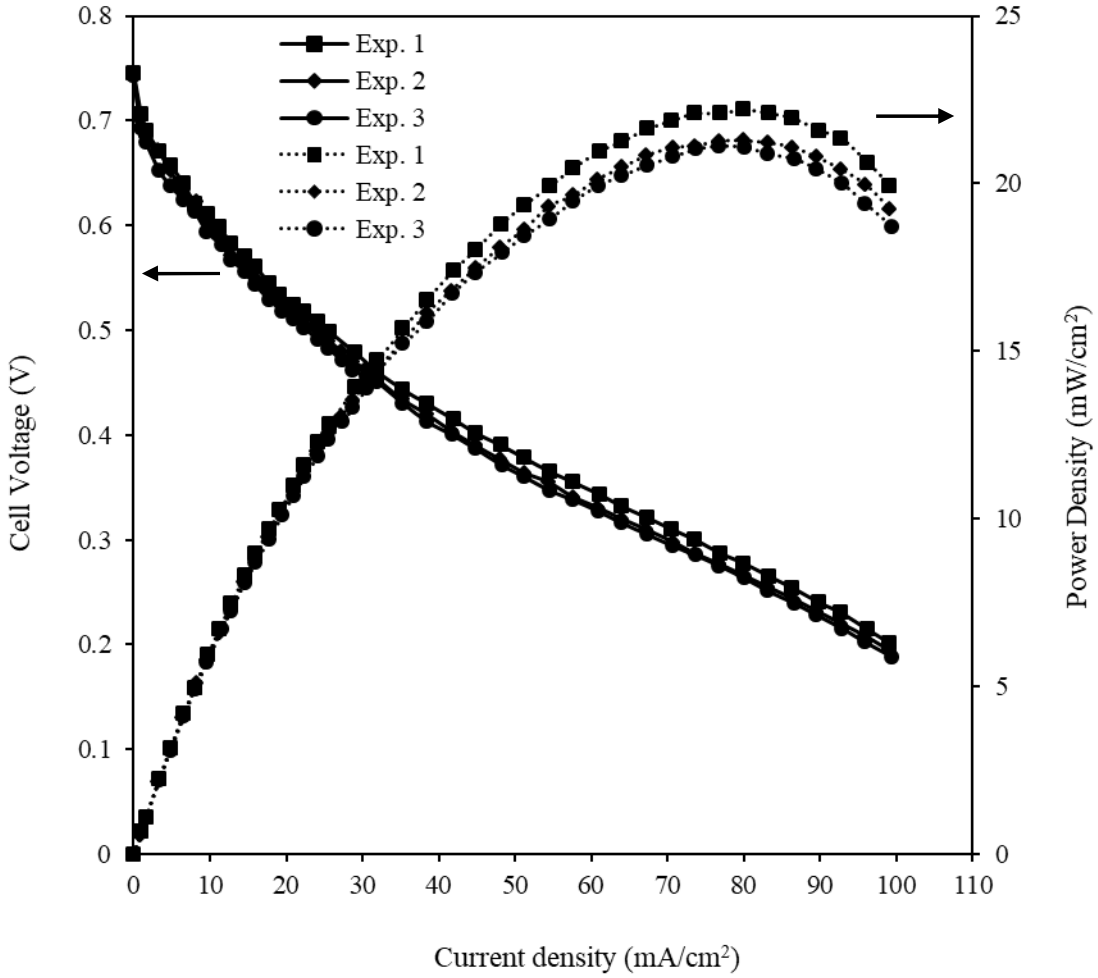

Figure 5.47 Polarization curves of three repeated confirmation tests.

Table 5.27 Developed quadratic model validation.

Ethanol conc. (M)	Electro-catalyst loading (mg/cm^2)	Operating cell temp. (°C)	Power density (mW/cm^2)					Error (%)
			Model predicted	Exp. 1	Exp. 2	Exp. 3	Avg.	
2.03	1.14	79.48	22.10	22.20	21.27	21.12	21.53	2.58

Conc.: Concentration, Temp.: Temperature, Exp.: Experiment and Avg.: Average value.